

## A method to improve the prediction of ship resistance in shallow water

Zeng, Qingsong

**DOI**

[10.4233/uuid:d4d8524a-fedc-4949-a953-f5848a1634bb](https://doi.org/10.4233/uuid:d4d8524a-fedc-4949-a953-f5848a1634bb)

**Publication date**

2019

**Document Version**

Final published version

**Citation (APA)**

Zeng, Q. (2019). *A method to improve the prediction of ship resistance in shallow water*. [Dissertation (TU Delft), Delft University of Technology]. <https://doi.org/10.4233/uuid:d4d8524a-fedc-4949-a953-f5848a1634bb>

**Important note**

To cite this publication, please use the final published version (if applicable). Please check the document version above.

**Copyright**

Other than for strictly personal use, it is not permitted to download, forward or distribute the text or part of it, without the consent of the author(s) and/or copyright holder(s), unless the work is under an open content license such as Creative Commons.

**Takedown policy**

Please contact us and provide details if you believe this document breaches copyrights. We will remove access to the work immediately and investigate your claim.

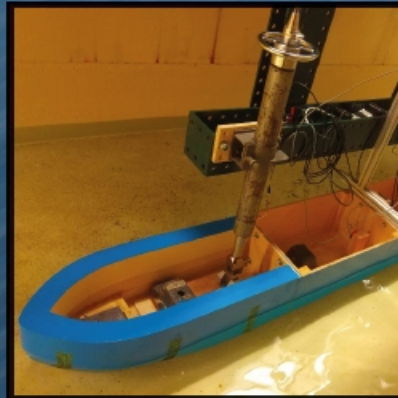
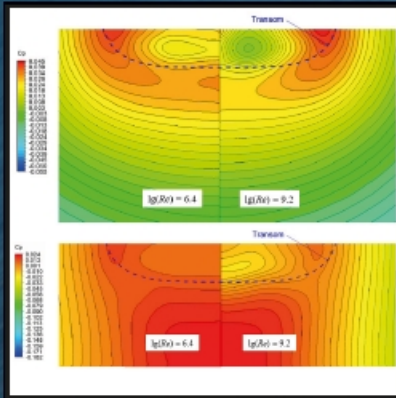
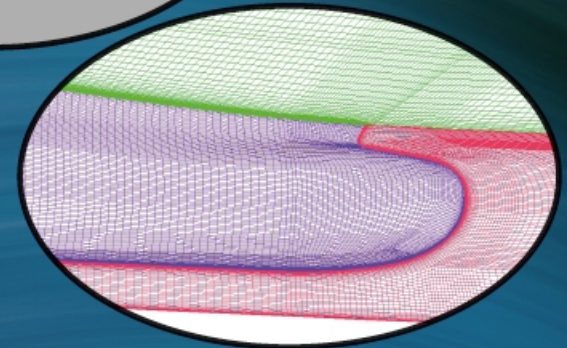
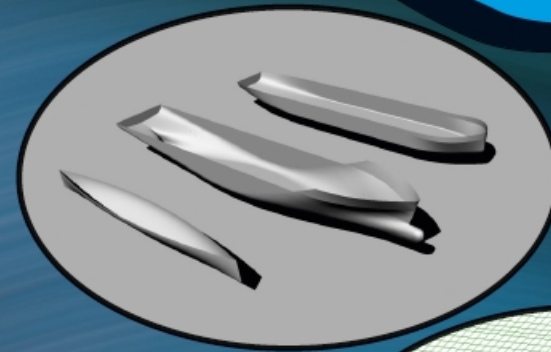
This dissertation describes an approach to improve the extrapolation of ship resistance for model-scale tests carried out in shallow water. The effects of limited water depths on the three components of ship resistance (frictional resistance, viscous pressure resistance, and wave-making resistance) have been studied individually. Empirical formulas have been developed for three ship types in various water depths.

# A Method to Improve the Prediction of Ship Resistance in Shallow Water

Qingsong Zeng

A Method to Improve the Prediction of Ship Resistance in Shallow Water

Qingsong Zeng



# **A Method to Improve the Prediction of Ship Resistance in Shallow Water**



# **A Method to Improve the Prediction of Ship Resistance in Shallow Water**

## **Dissertation**

for the purpose of obtaining the degree of doctor  
at Delft University of Technology,  
by the authority of  
the Rector Magnificus, prof. dr. ir. T.H.J.J. van der Hagen,  
chair of the Board for Doctorates,  
to be defended publicly on Friday 6 December 2019 at 12:30 o'clock

by

**Qingsong ZENG**

Master of Science  
in Design and Manufacture of Ships and Marine structures,  
Wuhan University of Technology, China.  
born in Guangshui, Hubei, China.

This dissertation has been approved by the  
promotor: Prof. ir. J.J. Hopman  
copromotor: Dr. ir. R.G. Hekkenberg  
copromotor: Dr. -Ing. C.H. Thill

Composition of the doctoral committee:

Rector Magnificus, Prof. ir. J.J. Hopman, Dr. ir. R.G. Hekkenberg, Dr. -Ing. C.H. Thill,	Chairperson Delft University of Technology, promotor Delft University of Technology, copromotor Delft University of Technology, copromotor
---	---

*Independent members:*

Prof. dr. ir. G. Delefortrie,	Ghent University; Flanders Hydraulics Research, Belgium
Prof. dr. -Ing. Z. Zou,	Shanghai Jiao Tong University, China
Prof. dr. ir. M. van Koningsveld,	Delft University of Technology
Prof. dr. ir. T.J.C. van Terwisga,	Delft University of Technology

This research is funded by the China Scholarship Council (No. 201506950009), the section of Ship Design, Production and Operation in the Department of Maritime and Transport Technology, at Delft University of Technology, the Netherlands.



*Keywords:* Ship resistance; Shallow water; Resistance extrapolation; Friction; Form factor; Wave-making; Computational Fluid Dynamics; Experimental Fluid Dynamics

*Printed by:* Gildeprint

Copyright © 2019 by Q. Zeng

All rights reserved. No part of the material protected by this copyright notice may be reproduced or utilized in any form or by any means, electronic or mechanical, including photocopying, recording or by any information storage and retrieval system, without written permission from the author.

ISBN 978-94-6384-090-3

An electronic version of this dissertation is available at  
<http://repository.tudelft.nl/>.

*To my wife  
Yuying  
for your continuous support.  
Qingsong*



# Contents

<b>Summary</b>	<b>xi</b>
<b>List of Symbols</b>	<b>xv</b>
<b>1 Introduction</b>	<b>1</b>
1.1 Research Objectives . . . . .	4
1.2 Research Method and Scope . . . . .	5
1.3 Dissertation Outline . . . . .	6
<b>2 A Physical Understanding of Shallow-water Ship Resistance</b>	<b>9</b>
2.1 Introduction . . . . .	9
2.2 Resistance Decomposition . . . . .	12
2.3 Frictional Resistance . . . . .	13
2.3.1 Experiments . . . . .	13
2.3.2 Numerical Method . . . . .	14
2.3.3 Recommendations . . . . .	16
2.4 Viscous Pressure Resistance . . . . .	17
2.4.1 Experiments . . . . .	18
2.4.2 Numerical Method . . . . .	18
2.4.3 Recommendations . . . . .	19
2.5 Wave-making Resistance . . . . .	20
2.5.1 Experiments . . . . .	21
2.5.2 Numerical Method . . . . .	22
2.5.3 Recommendations . . . . .	22
2.6 Coupled Scenarios . . . . .	23
2.6.1 Interactions among Resistance Components . . . . .	23
2.6.2 Trim and Sinkage . . . . .	23
2.7 Concluding Remarks . . . . .	24
<b>3 A Benchmark Test of Ship Resistance in Shallow Water</b>	<b>27</b>
3.1 Introduction . . . . .	27
3.2 Test Model and Scheme . . . . .	28
3.2.1 Test Model . . . . .	28
3.2.2 Test scheme . . . . .	29
3.3 Sources and Propagation of Uncertainties . . . . .	30
3.3.1 Hull Geometry . . . . .	31
3.3.2 Test Installation . . . . .	32
3.3.3 Instrument Calibration . . . . .	32
3.3.4 Repeating Tests . . . . .	35

3.4	Data Reduction . . . . .	36
3.5	Results and Uncertainty Evaluations . . . . .	37
3.6	Concluding Remarks. . . . .	44
<b>4</b>	<b>A Shallow Water Friction Line in 2D Cases</b>	<b>45</b>
4.1	Introduction . . . . .	46
4.2	Approach . . . . .	47
4.2.1	Simplification . . . . .	48
4.2.2	Computational Model . . . . .	49
4.2.3	Mesh Generation . . . . .	50
4.2.4	Boundary Conditions . . . . .	50
4.3	Verification and Validation . . . . .	53
4.3.1	Verification . . . . .	54
4.3.2	Validation . . . . .	56
4.4	Results and Analysis. . . . .	59
4.4.1	Physics of Shallow Water Effects on Friction . . . . .	60
4.4.2	The Validity of Zero-pressure Gradient Assumption . . . . .	61
4.4.3	Shallow Water Effects on Frictional Resistance . . . . .	65
4.4.4	The Fitting of a Numerical Friction Line . . . . .	66
4.4.5	Application and a Case Study . . . . .	67
4.5	Concluding Remarks. . . . .	69
<b>5</b>	<b>Shallow Water Effects on the Viscous Resistance of Ships</b>	<b>71</b>
5.1	Introduction . . . . .	72
5.2	Method . . . . .	73
5.2.1	The Strategy of Comparison . . . . .	73
5.2.2	The Models . . . . .	74
5.2.3	Mesh Generation and the Solver . . . . .	78
5.3	Verification and Validation . . . . .	78
5.3.1	Verification . . . . .	79
5.3.2	Validation . . . . .	81
5.4	Results and Analysis. . . . .	85
5.4.1	The Frictional Resistance . . . . .	85
5.4.2	The Viscous Pressure Resistance . . . . .	89
5.4.3	The Significance of Shallow Water Effects on Viscous Resistance . . . . .	98
5.5	Case Study of Viscous Resistance in Extremely Shallow Water . . . . .	99
5.5.1	Case Setup . . . . .	100
5.5.2	Results and Discussion . . . . .	101
5.5.3	Supplementary Notes . . . . .	107
5.6	Concluding Remarks. . . . .	108
<b>6</b>	<b>Shallow Water Effects on Ship-generated Waves</b>	<b>111</b>
6.1	Introduction . . . . .	112
6.2	Method . . . . .	112
6.2.1	Linear and Non-linear Wave Theories . . . . .	113
6.2.2	Code Verification and Validation. . . . .	116

6.3	Shallow Water Effects on Inviscid Ship Waves. . . . .	120
6.3.1	Wave Height . . . . .	121
6.3.2	Wavelength and Wave Superposition . . . . .	122
6.4	Effects of Viscosity on Ship Waves . . . . .	124
6.4.1	Effects of Viscosity on Wave Height . . . . .	124
6.4.2	Effects of Bottom Friction . . . . .	125
6.5	Scale Effects on Wave-making Resistance . . . . .	129
6.5.1	Case Design . . . . .	129
6.5.2	Results and Analysis. . . . .	130
6.6	Concluding Remarks. . . . .	133
<b>7</b>	<b>A Method to Improve Resistance prediction in Shallow Water</b>	<b>135</b>
7.1	Motivation . . . . .	135
7.2	The Proposed Method . . . . .	136
7.2.1	Wave-making Resistance Coefficient $C_w^*$ . . . . .	136
7.2.2	Frictional Resistance Coefficient $C_f^*$ . . . . .	137
7.2.3	The Form Factor $1+k^*$ . . . . .	138
7.3	Robustness Evaluation . . . . .	139
<b>8</b>	<b>Conclusions and Recommendations</b>	<b>145</b>
8.1	Conclusions . . . . .	145
8.1.1	Final Goal . . . . .	145
8.1.2	Frictional Resistance. . . . .	147
8.1.3	Viscous Pressure Resistance . . . . .	148
8.1.4	Wave-making Resistance . . . . .	149
8.2	Recommendations . . . . .	149
8.2.1	Experimental Aspect . . . . .	149
8.2.2	Computational Aspect . . . . .	150
8.2.3	Application Range . . . . .	150
8.2.4	Coupled with the propulsion system . . . . .	151
	<b>References</b>	<b>153</b>
	<b>Acknowledgements</b>	<b>163</b>
	<b>Curriculum Vitæ</b>	<b>165</b>
	<b>List of Publications</b>	<b>167</b>



# Summary

## *Motivation*

The traditional approach of extrapolating the experimentally measured resistance of a ship model to full scale is based on the Froude assumption or the form factor assumption, where the viscous part and wave-making part of the resistance are dealt with in deep water. In shallow water, however, the water-depth dependency of flat-plate/ship frictional resistance as well as form- and wave effects are expected. It is found in this dissertation that all of these three properties are deviating more or less clearly from the traditional understanding from certain water depths (expressed by the water-depth/ship-draft ( $h/T$ ) ratio).

A correct understanding of the resistance of ships in shallow water from the very basis is necessary to build a new approach to improve resistance prediction considering the water-depth dependency of the three features mentioned above. It can benefit for all further hydrodynamics-related ship researches, e.g., a reliable performance prediction, truly valid rules for ship design and even future work on understanding ship propulsion in (extremely) shallow water when navigating in inland waterways and coastal waters. This approach also allows further applications of the well-accepted extrapolation method with at the same time taking into account the inherent deviations in shallow water.

## *Goals and Approach*

- Final goal: To understand the mechanisms of shallow water effects on ship resistance and based on this to improve the extrapolation of ship resistance in shallow water.

A new extrapolation method is proposed for resistance extrapolation in shallow water. Based on the physical meanings of different parts of the resistance, shallow water effects on each component are studied separately. The Final goal is accordingly split into three sub-goals, which will be introduced later. Computational Fluid Dynamics (CFD) method is used to gain an insight into the flow field and also the results of resistance.

- Starting point: State-of-the-art knowledge and physical observation.

The existing research on ship resistance in shallow water is collected and summarized, reviewing both experimental and numerical studies. Knowledge gaps in those studies are identified, and the way this dissertation going to fill them is introduced (Chapter 2). A resistance

test of an inland ship model is performed in the towing tank at TU Delft, which provides physical observations and validating data for the chapters that follow (Chapter 3).

- Sub-goal 1: Understand the mechanism of how frictional resistance changes in shallow water.

A flat plate is first used to reveal shallow water effects on the characteristics of the boundary layer at the ship's bottom (Chapter 4) and then the study is extended to ship forms to investigate the 3D flow effects (first half of Chapter 5). After verifications and validations, systematic computations are performed in a commercial solver (ANSYS Fluent). In the computations, Reynolds number and water depth are considered as control variables. Based on the results, a database is built to fit a numerical correlation line for frictional resistance.

- Sub-goal 2: Understand the mechanism of how viscous pressure resistance changes in shallow water.

Double-body computations are performed to obtain the viscous pressure resistance separately (second half of Chapter 5). Systematic calculations are performed for three ships, which are different in terms of the flat bottom and the block coefficient. Based on the results, shallow-water and ship-form effects on the viscous pressure resistance (expressed by a modified form factor  $k^*$ ) are evaluated.

- Sub-goal 3: Understand the mechanism of how wave-making resistance changes in shallow water.

By adjusting the settings in the simulations, the influence of viscosity on ship-generated waves can be obtained. By performing resistance calculations with a free surface and combining with double-body computations at the same velocity and water depth, wave-making resistance can be derived approximately. Based on the results, the Reynolds number dependency of wave-making resistance can be studied in shallow water (Chapter 7).

- Develop a method to improve the prediction of ship resistance in shallow water.

Based on the understandings of shallow water effects on the three resistance components, a method to improve the resistance prediction in shallow water is built by modifying the extrapolation method of ship resistance from model scale to full scale.

### *Main Findings and Contribution*

- The changes in frictional resistance depend on whether the boundary layer can be developed freely. The assumption of zero pressure

gradient along a flat plate is found being not valid in extremely shallow water. A general method is suggested for the prediction of ship's frictional resistance in shallow water.

- A modified form factor defined based on the ship's frictional resistance can better convey physical meanings, especially in shallow water. The presence of transom can cause an increase in the form factor at the full-scale Reynolds number range.
- The Reynolds number dependency of wave-making resistance is found being obvious for relatively fuller ships in shallow water.
- A novel method to improve resistance extrapolation is proposed by correcting shallow water effects on each of the traditional resistance component separately. Empirical formulas have been developed for three ship types in various water depths. In the case studies, the proposed method can reduce the error of the resistance prediction to the range -5% ~ 2% whereas an error range -10% ~ 30% is normally generated if the traditional way is applied.



# List of Symbols

$1 + k$	Form factor
$a$	Wave amplitude (m)
$B$	Beam of a ship (m)
$B_C$	Blockage coefficient
$C_B$	Block coefficient
$C_f$	Coefficient of frictional resistance
$C_{fb}$	Coefficient of water bottom friction
$C_{fx}$	Coefficient of local frictional resistance
$C_p$	Coefficient of pressure
$C_r$	Coefficient of residual resistance
$C_t$	Coefficient of total resistance
$C_v$	Coefficient of viscous resistance
$C_{vp}$	Coefficient of the viscous pressure resistance
$c$	Wave speed (m/s)
CFD	Computational Fluid Dynamics
$D$	Distance between flat plate and parallel wall (m)
$d$	Distance between the sample point and the flat plate (m)
$E(m)$	Complete elliptic integral of the second kind
$E_D$	Energy dissipated on water bottom (J/m)
$E_k$	Kinetic energy per wavelength (J/m)
$E_p$	Potential energy per wavelength (J/m)
$E_T$	Total energy per wavelength (J/m)
EFD	Experimental Fluid dynamics
$Fr$	Froude number
$Fr_h$	Depth Froude number
$g$	Acceleration of gravity (m/s <sup>2</sup> )
$H$	Wave height (m)
$h$	Water depth (m)
$h_i$	A parameter which identifies the grid cell size
$I$	Turbulence intensity
$K(m)$	Complete elliptic integral of the first kind
$k$	Wavenumber (1/m)
$L$	Length of a plate or a ship (m)
$L_{oa}$	Overall length of a ship (m)
$L_{pp}$	Perpendicular length of a ship (m)
$m$	Elliptic parameter
$N$	Number of grid points
$n$	Number of waves along a ship hull

$p$	Order of accuracy
$R$	A symbol representing errors in grid study
$R_{vp}$	Viscous pressure resistance
$R_w$	Wave-making resistance
$Re$	Reynolds number
$Re_0$	Reynolds number of the incoming flow
$Re_B$	Reynolds number of the flow underneath ship's bottom
$Re_x$	Local Reynolds number
$Re_\theta$	Momentum boundary layer thickness Reynolds number
$S$	Wetted surface ( $m^2$ )
$S_B$	Wetted surface of the flat bottom of a ship or model ( $m^2$ )
$S_v$	Wetted surface of the vertical surface of a ship or model ( $m^2$ )
$SRE$	Standard deviation
$S_T$	Total wetted surface of a ship or model ( $m^2$ )
$T$	Draft of ship (m)
$t$	Time (s) or dimensionless time
$U_\infty$	Initial flow velocity (m/s)
$U_{ave}$	Reynolds averaged velocity (m/s)
$U(\phi_i)$	Uncertainty of a variable $\phi_i$
$u$	Horizontal velocity (m/s)
$u_x$	Velocity (m/s) and dimensionless velocity in horizontal direction
$u_y$	Velocity (m/s) and dimensionless velocity in vertical direction
$u^+$	A dimensionless velocity
$u^*$	Shear velocity (m/s)
$V$ or $V_0$	Velocity of the incoming flow (m/s)
$V_B$	Average input velocity of the flow underneath ship's bottom (m/s)
$V_{cr}$	Critical speed (m/s)
$V_h$	Velocity at water bottom (m/s)
$w$	Vertical velocity (m/s)
$y^+$	Y plus, a non-dimensional wall distance
$\alpha$	A parameter which identifies the grid cell size
$\beta$	A correction factor for wave-making resistance coefficient
$\gamma$	Equivalent factor for a virtual ship draft
$\epsilon$	Percentage of energy dissipation
$\eta$	Free surface elevation (m)
$\kappa$	Von Kármán constant
$\lambda$	Wavelength (m)
$\mu$	Molecular dynamic viscosity ( $Pa \cdot s$ )
$\mu_t$	Turbulent viscosity ( $Pa \cdot s$ )
$\nu$	Kinematic viscosity ( $m^2/s$ )
$\rho$	Water density ( $kg/m^3$ )
$\tau$	Shear stress ( $N/m^2$ )
$\tau_w$	Wall shear stress ( $N/m^2$ )
$\phi$	Velocity potential ( $m^2/s$ )
$\omega$	Wave frequency (1/s)

# 1

## Introduction

For nearly all types of ship, they inevitably spend part of their life in rivers, canals, harbors and/or coastal regions. In these areas, the behavior of a ship is strongly influenced by waterway conditions, such as water depth, water width, etc., as an example shown in Figure 1.1. Water depth is a crucial factor that affects the resistance of a ship, influences fuel consumption, and even determines the maximum navigating speed. In extremely shallow waters, the depth of water is only slightly larger than the draft of a ship and would make the ship's resistance significantly higher than in deep water.



Figure 1.1: A ship sails in a restricted waterway (Photo taken by the author, 2017)

Therefore for ships that are designed to operate in shallow water, it is essential to consider the effects of water depth on ship resistance from the aspects of both ship design and hull optimization:

First, a precise resistance prediction in shallow water can make a new-designed ship perform according to expectations. By providing references for power prediction, it can speed up the whole design process.

Secondly, a suitable prediction method can be applied for optimizing ship's dimension specifically for shallow water. Ship optimizers need to adjust a couple of parameters of a ship to reduce the added resistance caused by limited water depth, and Computational Fluid Dynamics (CFD) simulation is a popular tool to assist optimization (Van He and Ikeda, 2013). However, CFD method still takes more time than the empirical formulas (Kostas et al., 2015), which are more user-friendly like the method proposed by Holtrop and Mennen (1982) for deep water. Therefore, an efficient and effective prediction method in shallow - up to extremely shallow - water, which does not exist so far, would be helpful for ship optimizers.

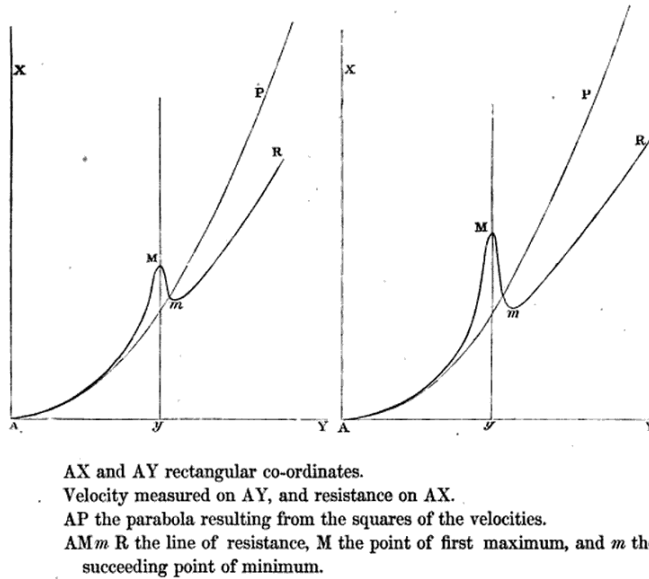


Figure 1.2: Instead of being a parabola, the curve of resistance against ship velocity in shallow water shows a different trend (Russell, 1837)

Historically, shallow water effects on ship resistance have been recorded quite early. In the summer of 1834, John Scott Russell observed that the resistance of a vessel in shallow water attained a local maximum at a certain velocity and immediately after this point, it dropped to a local minimum after which the increment of the resistance was recovered, as shown in Figure 1.2. He published this observation on the transactions of the Royal Society of Edinburgh (Russell, 1837). This finding is now well-known, and researchers have continued the study of ship resistance in shallow water until now.

A systematic and well-known study was published by Schlichting (1934). Based on a large number of model tests, several graphs were provided to show how a ship's resistance in shallow water deviates from that in deep water. Lackenby (1963) improved Schlichting's method by modifying the

method of speed correction and enlarging the range of application. However, Schlichting admitted that his method is lacking physical basis and not valid in extremely shallow water. Jiang (2001) proposed a mean effective speed based on the effective hydraulic blockage including the concept of the mean sinkage. In his case studies, this method made the total resistance to be a unit function of the effective speed and independent of the water depth. These methods are based on a correction of the resistance in deep water and reliant on the accuracy of the deep water prediction. However, deep water should be seen as an exception from shallow water and not vice versa. Thus, the physical basis of these methods is weak. The approach of Lackenby (1963) used to be recommended by the ITTC guidelines, but recently its reliability has been doubted for a wide range of modern ship designs and sizes (ITTC, 2017b).

In ship model tests, the traditional approach of extrapolating the experimentally measured resistance of a ship model to full scale is based on the Froude assumption, sometimes enhanced by the form factor assumption, where the frictional resistance depends on Reynolds number only, and the wave-making resistance solely depends on Froude number. In shallow water, however, the water-depth dependency of flat-plate/ship frictional resistance, viscous pressure resistance, and wave-making resistance will be proved. Regarding their different basic principles, all of these three properties would deviate more or less clearly from the traditional understanding in certain water depths.

Therefore, shallow water effects on ship resistance should be corrected componentwisely. Recently, corrections were conducted to correct the viscous part of ship resistance (Raven, 2012, 2016). However, the frictional resistance and the viscous pressure resistance are both among the viscous part, and Raven's method cannot recognize them separately. Further validations are also required for Raven's approach (ITTC, 2017b). Additionally, studies of the effects of water bottom friction on wave-making resistance at shallow-water conditions are scarce. To evaluate the applicability of the conventional extrapolation of resistance in shallow water, it would be valuable to evaluate the Reynolds number dependency of the wave-making resistance considering shallow water effects.

A correct understanding of the resistance of ships in shallow water from the very basis is necessary to build a more robust approach to improve resistance prediction considering the water-depth dependency of the three components mentioned above. It can benefit for all further hydrodynamics-related ship researches, e.g., a reliable performance prediction, truly valid rules for ship design, and even future work on understanding ship propulsion in (extremely) shallow water. This approach also allows the further application of the well-accepted extrapolation method while taking into account the inherent deviations caused by shallow water.

## 1.1. Research Objectives

In this dissertation, a solid understanding of the mechanisms of how a limited water depth affects the resistance of ships will be introduced to supplement Schlichting's research. Based on this, a robust approach to improve the prediction considering shallow water effects on each resistance component will become achievable, which forms the final goal of this dissertation:

**Final research goal:** *To understand the mechanisms of shallow water effects on ship resistance and based on this to improve the extrapolation of ship resistance in shallow water.*

Ships with different hull forms will have diverse resistance performance even when they sail in identical waterways. Therefore, it is challenging to build a generally-applicable method to predict the resistance of different ship forms in a range of water depth. However, it is possible to understand the physics of how the ship resistance responds to shallow water and provide general recommendations to improve the prediction based on studies of a certain number of ship forms.

The resistance of a ship hull is not "monochromatic". As aforementioned, the effects of shallow water on different components of the resistance are assumed to follow different rules and should be corrected separately. According to the currently-accepted approach that the three main components of ship resistance are frictional resistance, viscous pressure resistance, and wave-making resistance, the goal of this dissertation is also divided into three sub-goals. The envisaged approach for each sub-goal is also addressed briefly:

**Sub-goal 1:** *To understand the mechanism of how the frictional resistance changes in shallow water.*

For low-speed-sailing ships, the frictional resistance constitutes the majority of the total resistance. This component is therefore prioritized. Nevertheless, the ship's skin friction is difficult to be measured in a model test. The conventional way to achieve it is to apply empirical formulas, such as the ITTC 57 correlation line (ITTC, 1957), but this dissertation will show that this traditional prediction is insufficient in limited water depths, and it is recommended to modify the correlation line for shallow water.

To achieve this, a CFD approach is applied to obtain the friction by integrating the shear stress on the hull. As a further benefit from this approach, the physical details in the boundary layer, such as the velocity and pressure distribution, can be studied directly. Once sufficient data is acquired from the calculations, a method to predict a ship's frictional resistance in shallow water can be established.

**Sub-goal 2:** *To understand the mechanism of how the viscous pressure resistance changes in shallow water.*

The viscous pressure resistance of a ship, together with the frictional resistance, are two parts of the ship's viscous resistance. Conventionally, a non-dimensional form factor is used to show the significance of viscous pressure resistance. This factor can be regarded as the change in resistance due to a form that deviates from a flat plate. It can be determined by the quotient of viscous pressure resistance and friction. The form factor is practically treated as constant for a ship and its scaled models, but actually, its value is affected by a chosen friction line (ITTC, 2008). In this dissertation, through double-body CFD computations, a new definition of the form factor will be introduced, and the water depth dependency of the newly-defined form factor will be studied.

**Sub-goal 3:** *To understand the mechanism of how the wave-making resistance changes in shallow water.*

The research of shallow water effects on the component of wave-making resistance was started more than a century ago. One of the well-known studies is on the changes of wave pattern in shallow water, where the angle of the wave groups varies significantly when the ship's speed is near the critical velocity (Havelock, 1908). However, when the water is shallow enough, the water bottom friction will play a role in the alterations of ship's wave-making resistance. The conventional studies did not look into the effects of viscosity, especially the bottom friction, on ship-generated waves. This sub-goal is to find out whether and to which extent and up to which scaling factor of experiments, the effect of viscosity on the wave-making resistance exists.

## 1.2. Research Method and Scope

Basically, two methods can be used to estimate the resistance of a ship: ship model tests and numerical simulations. The method of ship model tests is a straightforward way to observe the physical phenomena around a hull. It can also provide validating data for numerical simulations, which is essential to check the reliability of a numerical method. However, the substantial cost and labor are the drawbacks of ship model tests. The numerical methods, on the other hand, such as Computational Fluid Dynamics (CFD), provide a more accessible and sometimes cheaper way to solve the problem (Anderson and Wendt, 1995). Through this method, the physical details of the interaction between a ship and the waterway can be observed numerically, and the results of each resistance component can be obtained in shallow water.

Therefore, a numerical method is applied as the primary tool to build the dataset. The reliability of the computing code will be validated by experiments, which are collected from published reports and papers. Due to the absence of publically available data of typical inland vessels, an inland ship model is constructed and tested in shallow water in the towing tank at TU Delft, which provides a further reference for validation.

A commercial CFD solver, ANSYS Fluent, is applied to execute all numerical computations in this dissertation. The numerical model was initially built in the Rhinoceros 3D, a commercial computer-aided design (CAD) software, and discretized in the ICEM-CFD, a meshing software of in ANSYS. To cope with a large number of computing tasks, two high-performance computers are utilized: the Reynolds, a cluster in the faculty of 3ME at TU Delft, and the Cartesius, which is the Dutch national supercomputer. Based on the results generated by the CFD method, the data of each resistance component is fitted by the least-squares method using the software Matlab.

This dissertation focuses on the physical understanding of ship resistance in pure shallow water, which has the following limitations in scope:

- The bottom of the waterway is even, and no current exists in the water;
- This research mainly focuses on the conditions of open shallow water without any lateral restrictions. Blockage effects in confined water have a significant influence on ship resistance, but they are outside the scope of this thesis;
- Subcritical speed range in open shallow water is the main interest regime. A limited number of cases in critical and supercritical speed regions are applied in both experiments and CFD computations for comparison;
- In the computations, the ship is fixed in the computational domain for simplification. Trim and sinkage are not included but they can make a difference in ship resistance. The study of sinkage can be included by regarding the position of a ship as the final stable condition sailing in shallow water, unless whose features of the wetted surface change obviously with sinkage;
- Bare hulls are used in this research. The propulsion system and ship appendices are not considered for simplification even though their effects on ship resistance are significant.

### 1.3. Dissertation Outline

This dissertation consists of eight chapters and is outlined in Figure 1.3.

Chapter 2 describes the general mechanism of ship resistance in shallow water. The changes of different physical parameters of the flow are discussed and compared with those in deep water. A brief history and the state-of-the-art research of ship resistance in restricted waterways are also presented.

Chapter 3 presents the details of a resistance test of an inland vessel in various water depths. The uncertainties of each measuring device are estimated, and the results of resistance are analyzed. This chapter provides

first-hand experimental data for the validations of the CFD calculations in the dissertation.

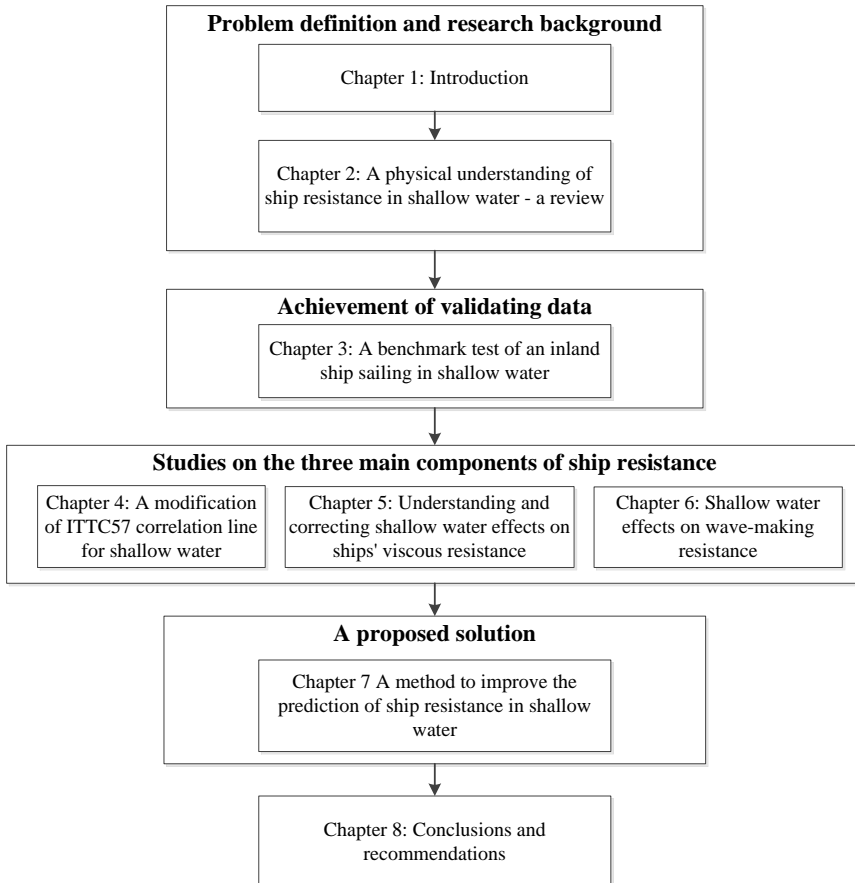


Figure 1.3: The outline of this dissertation

Chapter 4 simplifies the flat bottom of a typical inland vessel as a 2D flat plate and evaluates shallow water effects on the plate. The limited water depth is realized by installing another plate that is moving parallelly to the 2D flat plate. The changes in velocity and pressure distribution in the boundary layer are investigated.

Chapter 5 extends the research in Chapter 4 to 3D conditions by conducting double-body computations of three ship hulls in a range of water depths. The skin friction and the newly-defined form factor are obtained separately, and their responses to limited water depths are discussed

specifically. General expressions for the friction and the form factor are explored. A discussion of the viscous resistance in extremely shallow water is added at the end of this chapter.

Chapter 6 shows the energy dissipation on the water bottom and its effects on a ship's wave-making resistance. The Reynolds number dependency of wave-making resistance is discussed.

Chapter 7 builds an initial prediction method to improve ship resistance precision in shallow water based on the research of the previous chapters. Case studies are made to test the performance of this method and compared it with traditional approaches.

Chapter 8 concludes this dissertation. The recommendations for further improvements are given at the end of this chapter.

# 2

## A Physical Understanding of Shallow-water Ship Resistance

The prediction of ship resistance is essential for ship design and hull optimization, as it is discussed by, e.g., [Saha et al. \(2004\)](#) and [Rotteveel et al. \(2017\)](#). For vessels navigating on inland waterways and sea-going ships sailing in coastal areas, estuaries, and harbors, physical interactions between the hull and waterway make ship resistance different from that in deep water. To provide a practical and sufficiently reliable method for ship resistance prediction in shallow and confined water, a large amount of research has been conducted. A general review of these methods can be found in, e.g., [Pompée \(2015\)](#). However, a systematic discussion of the physics that determine how each resistance component reacts to a restricted condition is lacking, which is the main concern of this chapter.

### 2.1. Introduction

Generally, the usability of an empirical prediction method of resistance strongly depends on the ships and sailing conditions on which this method is based. When one of the conditions is changed, or an additional factor is added, the method should be revised accordingly. In shallow water, depth is an additional factor. A study focusing on the hydrodynamic aspects, i.e., the force, velocity, and pressure distribution, can provide a more in-depth insight into ship resistance in shallow water and assist in modifying a prediction method.

Before moving into the detailed discussion, the definition of shallow water is introduced. For restriction only in the water depth, if at least one of

the following two indicators has been reached, shallow water effects have to be considered (ITTC, 2017c) :

- Depth Froude number  $F\gamma_h = \sqrt{gh} > 0.5$ ;
- Water-depth to ship-draft ratio  $h/T < 4.0$ .

where  $V$  is ship's speed,  $g$  the gravitational acceleration,  $h$  the water depth, and  $T$  the ship's draft.

For ship resistance in shallow water, studying the velocity loss due to shallow water effects was the common method in the early stage of the research since it was difficult to obtain each resistance component directly (Schlichting, 1934). A brief history of the early-stage studies of ship resistance prediction in shallow water is shown in Table 2.1. Before the development of numerical simulation, the experimental method was basically the only way to do the research.

Most methods listed in Table 2.1 apply a velocity correction to correct shallow water effects, whose accuracy highly depends on the prediction of resistance in deep water. As mentioned in Chapter 1, these methods incorrectly regarded shallow water as an exception of deep water and not the other way around, which makes them physically weak or questionable. As admitted in the paper of Schlichting (1934):

*“I left no doubt that the described method should not be considered as absolutely precise and correct from the hydrodynamic standpoint.”*

Experimental techniques, as well as numerical methods, were not sufficiently developed in his time to provide enough physically correct answers. Physical details of the flow around a ship are not easily observed and measured, but this becomes more accessible nowadays, especially using numerical methods. Since different resistance components have different physical bases, studying the various components separately can help to gain a better insight into shallow water effects on ship resistance (Raven, 2012).

Following this track, this chapter is outlined accordingly like this: Section 2.2 explains why resistance is decomposed and clarifies that the scope of the review will limit to the three main components: frictional resistance, viscous pressure resistance, and wave-making resistance. Section 2.3, Section 2.4, and Section 2.5 will review the published research upon these three components in sequence, from both experimental and numerical aspects. Frankly, the demarcation of each resistance component is not entirely clear (Todd, 1966), i.e., they are coupled with each other and additionally affected by some other factors such as trim and sinkage. The influence of such coupled problems will be discussed in Section 2.6. Finally, conclusions and research content of the following chapters are given in Section 2.7.

Table 2.1: A brief history of the early-stage studies of ship resistance prediction in shallow water

Author	Research	$h/T$	Remarks
Schlichting (1934)	Wave resistance was considered to be constant if the length of ship-generated waves is equal in shallow and deep water. An experimental diagram of velocity loss for wave (actually: residual) resistance and frictional resistance was proposed.	> 1.33	
Landweber (1939)	Velocity correction for the effects of the cross section was suggested.		
Karpov (1946)	Two additional diagrams of speed corrections were provided for frictional resistance and residual resistance.	> 1.5	republished by Latorre et al. (1982)
Apukhtin (1947); Apukhtin and Voytkunskii (1953)	Ship speed between in shallow and in deep water was corrected by a single factor instead of two.	> 3.0	Latorre et al. (1982)
Schijf (1949); Schijf and Schönflöd (1953)	An analytical study of the relationship between depth Froude number and blockage was given.		
Lackenby (1963)	The range of the diagram proposed by Schlichting was extended to relatively deeper waters ( $Fr_h^2 < 0.3$ ). A correction to remedy the effects of wave retardation on frictional resistance was provided.	> 1.29	
Artjushkov (1968)	Tank wall effects on ship resistance were accounted for by a speed correction.		
Dand and Ferguson (1973)	An analytical study was performed for the backflow and ship's navigating speed in confined water.		
Bai (1978)	A correction was given to correct the blockage effect on ship velocity.		
Jiang (2001)	A mean effective velocity based on the mean sinkage was defined in shallow water. By using this new-defined speed, the total resistance can be seen as independent of water depth.	> 1.5	

## 2.2. Resistance Decomposition

This section is going to address two existing decompositions of the total resistance of a bare ship hull, and why corrections of shallow water effects should be made for each component individually.

It can be shown, e.g., by the principle of similitude (Rayleigh, 1892, 1915) or by the Buckingham  $\Pi$  theorem (Buckingham, 1914), that for all physical problems a limited number of dimensionless coefficients should be kept constant when conducting scaled model tests. For ship resistance tests, the relevant coefficients are the Froude number and the Reynolds number. As they cannot be kept constant simultaneously for a ship and its scaled models, Willam Froude as early as 1868 proposed that the total resistance of a ship can be divided into two parts: viscosity-related resistance and residual resistance (Froude, 1868). In the process of model-ship extrapolation, the frictional resistance was assumed to depend on the Reynolds number only and treated with the “equivalent plank” hypothesis; the residual resistance was assumed to depend on the Froude number only and follow Froude’s law of comparison.

In Froude’s assumption, the viscous pressure resistance was accounted for as a part of the residual resistance. In later research, it was shown that the viscous pressure resistance is more related to the Reynolds number, and the decomposition method could be improved by using a so-called form factor (Hughes, 1954). This factor was initially considered as constant and can be determined by the method of Prohaska (1966). However, it is now well-known that the form factor varies with the ship scale, even in deep water (García-Gómez, 2000). In this decomposition, on account of the physical basis, the total resistance is divided into three parts: the frictional resistance, the viscous pressure resistance, and the wave-making resistance.

These two treatments (Froude’s assumption and form factor assumption) of resistance decomposition are the common methods applied by almost all the towing tanks in the world. The latter approach is usually preferred (ITTC, 2017j) and will also be applied in this dissertation.

In shallow water, as it will be shown in this research, the shear stress, the pressure distribution along the ship hull, as well as the characteristics of ship-generated waves are influenced by the limited water depth. The three resistance components, which are related to these physical phenomena, need to be corrected individually, i.e., effects on shear stress should go into frictional resistance, effects on the pressure difference along the ship hull should be presented in the viscous pressure resistance, and the effects on wave properties should be included in wave-making resistance. In the following three sections, experimental and numerical studies for each resistance component are reviewed and discussed in sequence.

## 2.3. Frictional Resistance

As a relatively low speed is applied for most ships sailing in shallow water, the frictional resistance takes the majority of total resistance. Therefore, accurately predicting the frictional resistance is of the highest importance for those ships.

Physically, frictional resistance is an integral of all the local shear stresses on the hull surface projected into the longitudinal direction. Following Froude's "equivalent plank" assumption, many friction lines derived from flat plate (Grigson, 1999; Katsui et al., 2005; Schoenherr, 1932) can be used to predict the frictional resistance. By considering a part of form effects, a model-ship correlation line to predict the frictional resistance was proposed and recommended by ITTC proceedings (ITTC, 1957). However, as will be introduced in this dissertation, the presence of water bottom forces a thinner ship boundary layer resulting in higher frictional resistance. Furthermore, the water around the ship might change its local orientation and thus change the projected shear stress. Therefore, the friction lines and the correlation line designed for deep water needs to be corrected for shallow water. Such a correction requires accurate determination of the frictional resistance in shallow water.

There are basically two methods available to determine the frictional resistance: experiments and numerical simulations. In this section, it will be reviewed how these two methods were applied, and their feasibility considering shallow water effects will be discussed.

### 2.3.1. Experiments

The conventional way to measure the friction is using an "equivalent plank" with the same surface area and the same length as a (model) ship (Froude, 1871). The study of the friction on the flat plate is still used today to assist the investigation of the ship's frictional resistance (Eça and Hoekstra, 2008) based on a similar principle.

In shallow water, the method of using a flat plate can be applied to evaluate shallow water effects on the frictional resistance. By placing an additional plate parallel to the usual flat plate and making it move at the same speed as the incoming flow, a restricted space is formed to represent the under-keel clearance of ships. During the tests, it should be borne in mind that the limited space makes it more challenging to mount the measuring equipment, and the results can also be influenced by those devices.

In ship model tests and full-scale trials, it is difficult to measure the shear stress on a hull. The frictional resistance is implicitly measured as a part of the total resistance. In model tests, to improve the quality of measurements, the proportion of the turbulent boundary layer needs to be adjusted to a similar level as full-scale ship cases. For a full-scale sailing vessel, the Reynolds number is high ( $10^8 - 10^9$ ), and turbulent boundary layer starts immediately at the bow and stays attached to the hull. At the lower Reynolds numbers of ship models, the turbulent boundary layer starts rel-

actively later and unpredictably. Thus, to imitate the turbulent boundary layer at full scale, turbulence stimulators such as sand, tripwire, and pins (Hughes and Allan, 1951), are applied at the bow in model tests. In shallow water, the start point of the turbulent boundary layer is affected by the limited space and where to mount the stimulators should be reevaluated.

Currently, corrections for shallow water effects are usually applied to ship speed or on the form factor (ITTC, 2017b). Modifying the frictional resistance directly for shallow water is still rare. If enough experimental data of ships' frictional resistance is available, it can benefit such modification and also offer valuable validating data for new measuring devices as well as numerical simulations. Due to the difficulty of friction measurements, the numerical method will be applied as the main tool for the study of shallow water effects on shear stress.

### 2.3.2. Numerical Method

Compared to ship experiments, numerical methods like Computational Fluid Dynamics (CFD) are more recent and convenient to cope with the flow field around a ship. By solving the Navier-Stokes (N-S) equations or time-averaged N-S equations, physical details of the flow, such as velocity and pressure distribution, can be obtained directly by many CFD codes. It is easy to separate the friction from the total resistance by integrating the shear stress along the ship hull. However, the shortcomings of the CFD method are also found in the process of friction computations.

First, the choice of a turbulence model plays an important role. Since an analytical theory to predict the evolution of natural turbulence flows is absent, turbulence models are built to predict the statistical evolution of these flows (Pope, 2000). Based on this, the treatment of the flow parameters is different, and computations performed with different turbulence models will, therefore, lead to different results. For the simulations of water flowing over a flat plate, the results showed that the influence of a chosen turbulence model was even more significant than grid density, as shown in Figure 2.1 (Eça and Hoekstra, 2008).

In this figure, for computations with the same turbulence model, refining the mesh makes maximum 1.6% difference of the frictional resistance coefficient. However, a more considerable difference can be found between the results using different turbulence models (e.g., results with the SST model is generally 4% larger than those with BSL model). Therefore, the selection of a turbulence model should be validated by experiments and the corresponding differences in  $C_f$  should be given explicitly.

It should be noted that turbulence stimulation is more challenging to achieve in a numerical computation compared to a physical model test. It is possible to also build turbulence stimulators numerically, such as sandpaper with a certain roughness, and mount them on the ship hull digitally, but this method is not discussed in the publications and its performance is also not validated.

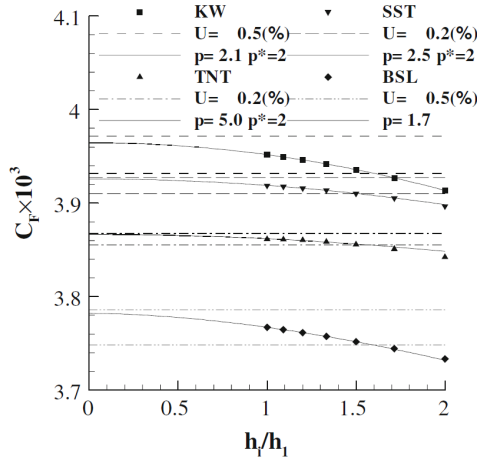


Figure 2.1: Convergence of the frictional resistance coefficient,  $C_F$ , with the grid refinement,  $h_i/h_1$ . (The finer the grid, the smaller the  $h_i/h_1$ . Turbulent flow over a two-dimensional finite plate,  $\lg(Re) = 6.25$ ) (Eça and Hoekstra, 2008)

Additionally, the turbulence intensity around a ship hull, which will be discussed in Chapter 5, will affect the computations of the frictional resistance. A value of more than 1% is recommended in a natural river or canal (Kozioł, 2013). Ideally, the value can be assigned at the inlet boundary, but since the flow at the inlet is set as unidirectional, the turbulence intensity decays fast before reaching the ship. According to Chapter 5, a small value (about 0.5%) is obtained if the inlet boundary is set too far (more than twice of the ship length) from the ship. Such a deviation can lead to about 3% difference in the friction. Thus, an appropriate position of the inlet boundary needs to be evaluated to make the numerical turbulence condition agree well a real test.

Secondly, the value of the calculated frictional resistance depends on the size of the cells in the first grid layer. The distance between the first computing point and the hull surface strongly influences the wall treatment selected in a numerical method. A non-dimensional factor,  $y^+$ , is commonly used to represent this distance which is defined as follows:

$$y^+ = \frac{u_\tau y}{\nu} \quad (2.1)$$

where  $y$  is the distance to the wall,  $u_\tau$  the shear velocity and  $\nu$  the kinematic viscosity. The value of  $y^+$  can usually be implemented to indicate the features of viscous sublayer ( $y^+ < 5$ ), buffer layer ( $5 < y^+ < 30$ ), log-law region ( $30 < y^+ < 200$ ) and outer layer ( $y^+ > 200$ ), in which the non-dimensional velocity  $u^+$  as a function of  $y^+$  can be virtualized (Nezu and Rodi, 1986; Pope, 2000; Wei and Willmarth, 1989) in Figure 2.2.  $u^+$  is defined by  $u/u_\tau$ , where  $u$  is the flow velocity parallel to the wall.

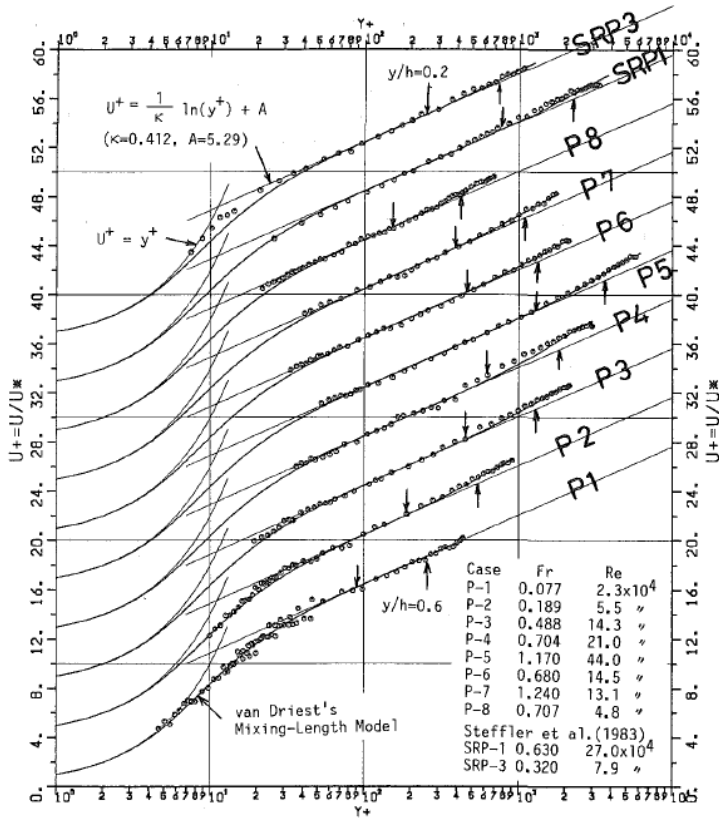


Figure 2.2: The non-dimensional velocity  $u^+$  as a function of  $y^+$  (Nezu and Rodi, 1986)

The value of  $y^+$  is recommended to be well under one to compute the boundary layer features directly (ITTC, 2017a). If the value is in the log-law region, wall functions can be applied, which provide an approximation of the viscous sublayer and buffer layer (ITTC, 2017a). In addition, to stabilize numerical computations of friction, the wall can be treated by blending the viscous sublayer formulation and the logarithmic layer formulation based on  $y^+$  (ANSYS, 2017b) and these two formulations are combined in an empirical way (such as Kader (1981)) to compute the buffer layer and outer layer. Therefore, studying the influence of  $y^+$  on the frictional resistance coefficient is needed to evaluate the  $y^+$  dependency of ship friction.

### 2.3.3. Recommendations

No analytical method is available for the prediction of frictional resistance in shallow water since the physical essence of turbulent flow is not fully understood yet. For unidirectional laminar flow over a semi-infinite flat plate, the friction can be calculated analytically (Blasius, 1908), but this

is an ideal condition and cannot apply for ships, where turbulence exists. Basically, the existing friction lines are derived from data fittings based on a large number of experimental data and/or numerical calculations. To improve the prediction of frictional resistance in shallow water, efforts should be made to obtain as much data as possible to enlarge the corresponding dataset through both physical tests and numerical computations.

Experimental techniques for measuring shear stress directly are limited to the flat plate where the friction is the only item of force. Measuring ship's friction separately from other resistance components is a difficult task. Therefore in this dissertation, CFD methods will be used as the primary tool to build the dataset mentioned above. Experience of computational settings gained from deep water may not be valid in shallow water. Items that should be evaluated in numerical computations include, but is not limited to, the performance of different turbulence models, the determination of  $y^+$ , the density of mesh, the level of turbulence intensity, and computational domain.

## 2.4. Viscous Pressure Resistance

Viscous pressure resistance ( $R_{vp}$ ) is the most complicated of the three resistance components. As indicated by the name, the impacts of viscosity and pressure are coupled for this component, which are reflected by ship scale and hull form, respectively.  $R_{vp}$  is an integral of the pressure difference caused by viscosity along the ship hull.

In shallow water, the hull together with the fairway bottom form a restricted space for water to pass through. According to the Bernoulli equation and the continuity equation, a decreased flow cross-section around a ship will cause an increase of flow speed and a decrease of pressure. The pressure distribution is therefore influenced, resulting in a different viscous pressure resistance (Raven, 2012). The suction force on ship bottom starts to be perceptible (about 0.44N) for a 7.8-meter ship model at between  $h/T = 4$  and  $h/T = 10$  compared to almost zero in deep water ( $h$  is water depth, and  $T$  is ship draft) (Sun et al., 2017).

Conventionally, the viscous pressure resistance is described by a form factor:

$$1 + k = \frac{C_v}{C_f} \quad (2.2)$$

where  $C_v$  is the coefficient of the viscous resistance, which is the sum of the frictional resistance coefficient ( $C_f$ ) and the viscous pressure resistance coefficient ( $C_{vp}$ ). For  $C_f$ , there was a debate on which friction line should be used to determine  $1+k$  (ITTC, 2008), but finally a true turbulent flat plate friction line instead of the ITTC57 correlation line was suggested (ITTC, 2017b), since  $1+k$  is more dependent on Reynolds number if the ITTC57 line is used.

To achieve the form factor,  $C_v$  or  $C_{vp}$  should be obtained separately, but in general, it is not an easy task. In this section, the experimental techniques and numerical methods to obtain  $C_{vp}$  will be discussed.

## 2

### 2.4.1. Experiments

A classical method of measuring the viscous resistance is the wake survey, in which the head loss in the wake compared to the incoming flow is measured and considered as the viscous resistance (Baba, 1969). In shallow water, due to the energy dissipation on the water bottom, the method of wake survey might overestimate the viscous resistance.

The velocity field around a ship hull can be shown with time-resolved Particle Image Velocimetry (PIV) technique (Mucha et al., 2018). Thus the pressure field can be predicted based on the Bernoulli equation, and the pressure distribution on ship hull can be obtained experimentally. However, the PIV method is not (yet) frequently applied for a resistance test in a towing tank.

The most commonly used method to obtain the form factor was proposed by Prohaska (1966), in which low-speed model tests (Froude number,  $Fr \leq 0.2$ ) should be applied to eliminate wave effects and benefit a linear fitting. Provided the ITTC (1957) correlation line is used, the form factor scale dependency was found and can be corrected (García-Gómez, 2000) by

$$k_s - k_m = 1.91 \cdot (\lambda - 1) \cdot 10^{-3} \quad (2.3)$$

where the subscripts  $s$  and  $m$  denotes the full-scale and model-scale ship, respectively.  $\lambda$  is the scale of the model, and the value of it equals to one indicates the full-scale ship.

In shallow water, the form factor is further affected by the depth of waterway. By lowering the water level of a towing tank, shallow water conditions can be realized. If enough number of model tests are performed in shallow water, it is possible to provide an empirical formula to correction shallow water effects on form factor, such as equation proposed by (Millward, 1989):

$$\Delta k = 0.644(h/T)^{-1.72} \quad (2.4)$$

However, a correction considering both ship scale and water depth does not exist. Resistance tests with different sizes of model, and probably the full-scale ship, in shallow water are therefore required.

### 2.4.2. Numerical Method

Numerical simulations provide a straightforward way to observe the pressure distribution on the ship hull, as shown in Figure 2.3. By comparing the pressure changes at the bow and stern in various water depths, shallow water effects on viscous pressure resistance can be explained physically.

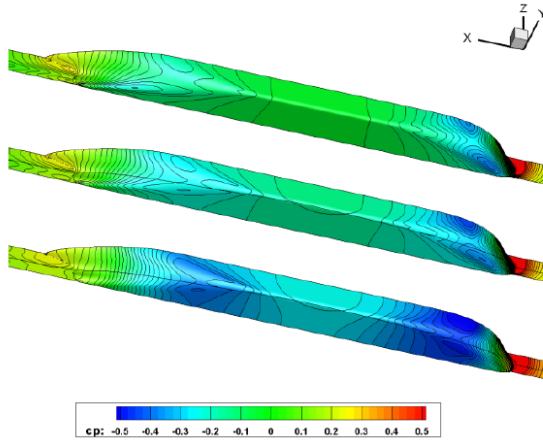


Figure 2.3: KVLCC2m, model scale. Effects of water depth on hull pressure distribution in viscous flow. Top: deep water; middle:  $h/T = 1.96$ ; bottom:  $h/T = 1.24$ . (Raven, 2012)

To separate  $R_{vp}$  from the pressure resistance, double-body computations (the free surface is suppressed) can be applied (Raven et al., 2008). In a double-body computation, the integral of the pressure on hull surface in the ship's sailing direction equals the viscous pressure resistance ( $R_{vp}$ ). However, for computations with free water surface, existing CFD codes are not able to distinguish  $R_{vp}$  from the pressure resistance. Likewise, shallow water effects solely on  $R_{vp}$  are physically not separable by existing numerical methods. By subtracting the frictional resistance, the viscous pressure resistance can be approximately achieved when assuming that the effect of a wavy free surface on the viscous pressure resistance could be neglected.

Significant efforts have been made to improve the prediction form factor, which directly relates to  $R_{vp}$ , in shallow water numerically (Raven, 2012, 2016; Toxopeus, 2011). Similar to the experiments, it is possible to build a correction for shallow water effects on form factor, such as equation (2.5) (Raven, 2016):

$$(1 + k)/(1 + k)_{deep} = 1 + 0.57(h/T)^{-1.79} \quad (2.5)$$

Equation (2.5) is claimed to be valid for  $h/T > 2.0$  since scattering data was found at  $h/T < 2.0$ .

### 2.4.3. Recommendations

In shallow water, as shown in Section 2.3, ship's friction is affected by limited water depth. If a turbulent plate friction line, as suggested by (ITTC, 2017j), is used in the definition of form factor, shallow water effects on the frictional resistance will be brought into the form factor, which makes its physical basis poor. To remedy this, the computed friction of the ship,

in which shallow water effects on frictional resistance is included, will be suggested (Chapter 5) to define the form factor ( $k^*$ ) in shallow water. By this definition, the factor  $k^*$  clearly represent the viscous pressure resistance.

Conventionally, the concept of the form factor is not recommended for ships with a transom (ITTC, 2017j). However, the immersed transom is typical for a large number of inland ships. Transom effects are already contained in the form factor derived from double-body computations. There are, at least to the author's knowledge, no reliable methods to separate it precisely from form factor. Furthermore, the influence of the transom on resistance is physically a part of viscous pressure resistance. Thus for practical reasons, it will be considered as form effects and discussed within the form factor.

## 2.5. Wave-making Resistance

Wave-making resistance is generally a small part of the total resistance for most inland ships. However, for high-speed ships and also for model-ship resistance extrapolation, this section will show that wave-making resistance begins to play a role, and a study of viscous effects on ship-generated waves becomes necessary to improve the prediction of wave-making resistance.

Physically, wave-making resistance is a result of the energy transfer from ship to ship-generated wave system. Since shallow water effects on wave pattern (e.g., the Kelvin angle) are easily observed, investigations on wave-making resistance in shallow water have started very early (Havelock, 1908). With the potential wave theory, wave-making resistance can be predicted analytically (Havelock, 1928; Michell, 1898). In most of these studies, the influence of viscosity was considered as negligible.

However, when the water is sufficiently shallow, water particles can no longer move freely, and the oscillating movements adjacent to the bottom will be affected by the bottom friction. For example, according to linear wave theory (Airy, 1841), the velocity of water particles at the bottom ( $V_h$ ) is given as follows,

$$V_h = \frac{a\omega}{\sinh(kh)} \cos(kx - \omega t) \quad (2.6)$$

where  $a$  is the wave amplitude,  $k$  the wavenumber,  $\omega$  the wave frequency,  $h$  the water depth,  $x$  the horizontal position and  $t$  the time.

In shallow water, as shown in the top picture in Figure 2.4, water particles should move freely following equation (2.6) but actually, the flow velocity on the bottom is zero due to viscosity (bottom picture in Figure 2.4). An oscillatory boundary layer is formed above the bottom, and consequently, a part of wave energy is dissipated in the boundary layer (Schlichting, 1979). Wave characteristics, such as wave height, will be influenced accordingly (Putnam and Johnson, 1949).

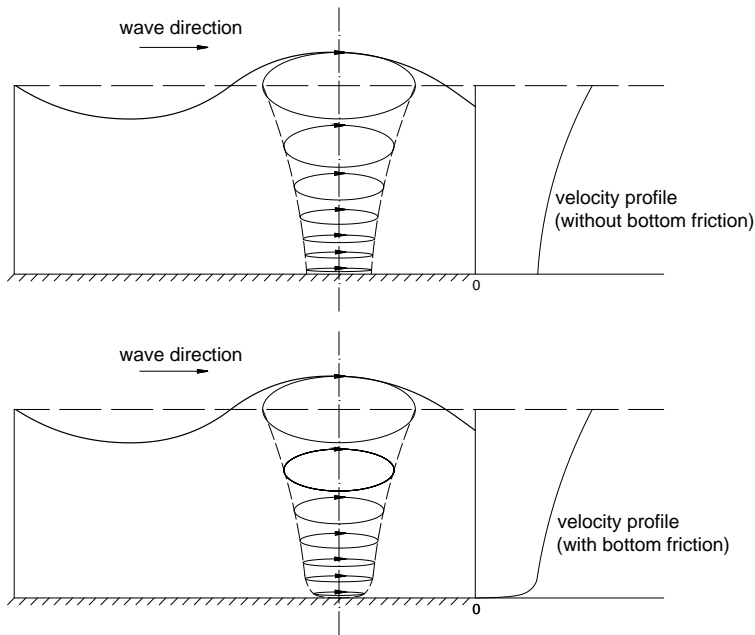


Figure 2.4: A sketch for movements and the maximum velocity profile in shallow water (top: without bottom friction; bottom: with bottom friction)

In the model-ship extrapolation of ship resistance, wave-making resistance is assumed to be independent of Reynolds number (ITTC, 2017j). However, since viscosity starts to play a role in shallow water, Reynolds number dependency of wave-making resistance should be reevaluated.

In this section, the acquisition of wave-making resistance by model test and numerical method in shallow water will be reviewed and discussed.

### 2.5.1. Experiments

Physically, the energy contained in ship-generated waves is initially generated from a part of the pressure on hull surface, and an integral of such pressure is equal to ship's wave-making resistance. Therefore, based on the conservation of energy, wave-making resistance can be derived by analyzing the energy of the wave system, which is known as wave pattern analysis. The two commonly-used methods are longitudinal wave cut and transverse wave cut (Sharma, 1963).

As a potential approach is applied, the influence of viscosity is neglected in the wave pattern analysis. For deep water though, the wave cut methods can provide acceptable predictions (Raven and Prins, 1998; Will and Kömpe, 2015). In shallow water, however, characteristics of ship-generated waves are affected by viscosity (Putnam and Johson, 1949), and the accuracy of wave-cut analysis needs to be evaluated (Thill, 1991).

In experiments, the effects of viscosity on the wave system are not easy to measure. Furthermore, to reveal the effects of bottom friction on waves, a case when the bottom friction is zero might be required for comparison purposes. This case is almost impossible in model tests but can be easily realized in numerical computations, which will be discussed in the next section.

### 2.5.2. Numerical Method

With a well-developed potential wave theory (Michell, 1898), it is possible to obtain the wave-making resistance ( $R_w$ ) analytically in inviscid flow. However, an analytical prediction of  $R_w$  considering the effects of viscosity does not exist. The method of Computational Fluid Dynamics (CFD) is now used by many researchers to study ship-generated waves in viscous flow.

Since the existing CFD codes cannot distinguish  $R_w$  from the total pressure resistance, a common practice is to regard  $R_w$  as the difference of the total resistance calculated with and without free surface (Raven et al., 2008). This treatment is an approximation and is acceptable provided the difference of the frictional resistance in both cases is minor compared to  $R_w$ .

By controlling the boundary conditions on water bottom, the effects of bottom friction on waves can be evaluated explicitly (Pascolo et al., 2018; Tsang et al., 2018).

### 2.5.3. Recommendations

Numerical computation is applied as the primary method in this dissertation to study the Reynolds number dependency of wave-making resistance in shallow water. By using different scales of ship model, scale effects on  $R_w$  in shallow water can be studied. If the effects of viscosity are found to be significant for certain shallow water conditions, the Reynolds number dependency of wave-making resistance should be considered.

Since such computations are related to friction, the numerical setup, such as the density of mesh and the value of  $y^+$  introduced in Section 2.3.2, also needs to be discussed in the study of wave-making resistance. Meanwhile, the grid dependency of the wave profile should also be studied to determine how many grid points per wavelength are needed to guarantee a practically sufficient resolution of waves. Detailed studies on the items mentioned above will be given in Chapter 6.

Compared with experimental data in deep water, measurements of wave characteristics in shallow water are mostly not publically available. Full-scale measurements are even more scarce. The validation of computed ship-generated waves can largely benefit from more available experiments, and this is recommended for the research on the next stage.

## 2.6. Coupled Scenarios

### 2.6.1. Interactions among Resistance Components

As discussed in Section 2.2, the total resistance of a bare hull can be divided into three components: frictional resistance, viscous pressure resistance, and wave-making resistance, which are determined based on their physical bases. Strictly speaking, these three components are coupled with each other and cannot be separated clearly (Todd, 1966).

The friction on the hull surface can influence the pressure gradient around the surface, especially in shallow water, by which the pressure distribution on the hull is altered leading to a different viscous pressure resistance and wave-making resistance. In addition, ship-generated waves change the area of the wetted surface and also make the local friction on the area that closes to the free surface change periodically. Thus, an average of the friction over the whole surface is not necessarily equal to that in a double-body test. Meanwhile, the viscous pressure resistance and the wave-making resistance are defined only based on how the energy is transferred, but in principle, both of them originally come from the pressure on the hull and essentially interchangeable.

Nevertheless, such coupled phenomena make no difference to the frictional resistance, which is determined by the integral of the shear stress in the longitudinal direction, and it includes all the coupled influence on the shear stress from other resistance components. The coupled phenomena only matter for pressure-based resistance components, i.e., the viscous pressure resistance and wave-making resistance. In this dissertation, the viscous pressure resistance will be obtained individually through the simulations with the free surface suppressed, and the calculated form factor will be assumed to be identical to the calculations with a free surface.

Indeed, one should keep an eye open on new definitions and explore a solution for the coupled problem for pressure-based resistance components, but it is not in the scope of this research.

### 2.6.2. Trim and Sinkage

In shallow water, due to the changes of the under-keel pressure field, the trim and sinkage are amplified compared to deep water (Gourlay, 2008) and also coupled with ship resistance. The under-keel clearance becomes smaller than a designed value which leads to stronger shallow water effects. The wetted surface is also altered due to sinkage, resulting in a different frictional resistance. The changes in pressure distribution caused by trim and sinkage will further affect the viscous pressure resistance and wave-making resistance. When the velocity of the vessel is approaching the critical speed range (in open shallow water, the critical speed is given by  $V_{cr} = \sqrt{gh}$  (Havelock, 1908)), ship's movements during the resistance test in shallow water becomes unstable, As will be pointed out in Chapter 3, it will make the coupled problem more remarkable.

Nevertheless, most inland ships sail at subcritical speed range and the trim of corresponding ships is not significant. The study of sinkage can be included in computations by regarding the position of a ship as the final stable condition sailing in shallow water. Treating the ship as fixed is surely an approximation, but valuable information for improving the prediction of ship resistance in shallow water is expected.

## 2.7. Concluding Remarks

In this chapter, a brief history of the prediction of ship resistance in shallow water using speed-correction method is introduced. A discussion is made for two methods of decompositions of the total resistance. The method with three components, i.e., frictional resistance, viscous pressure resistance, and wave-making resistance, is preferred due to its stronger physical basis. Afterward, the experimental and numerical methods applied to investigate all these three components in shallow water have been reviewed. Several conclusions can be drawn as follows:

- For frictional resistance, the existing experiments are limited to the flat plate in unrestricted flow. Direct measurements of friction on a ship hull are difficult, and numerical simulations can provide an easier way to obtain the value of friction by an integral of the shear stress on the hull surface. However, the numerical results are sensitive to the settings of computations, and reliable verifications and validations are therefore required;
- For viscous pressure resistance, the method of wake survey can be used to derive this resistance experimentally but does not work well in shallow water. Alternatively, a linear fitting based on low-speed tests can provide practically reliable results of form factor as well as the corrections for shallow water effects. Double-body computations are common to determine form factor numerically. Shallow water effects on form factor can also be corrected based on numerical results;
- For wave-making resistance, wave pattern analysis can be applied, but its accuracy will be influenced by viscosity in shallow water. In numerical calculations, the difference between the total resistance computed with free surface and that without free surface can be accounted as an approximation of wave-making resistance. Water bottom friction plays a role leading to a Reynolds number dependency for wave-making resistance in shallow water. The conventional model-ship extrapolation should, therefore, be reconsidered for shallow water.

Based on the existing studies, some recommendations can be given for the following chapters:

- In the aspect of experiments, additional model tests in shallow water are needed to provide validating data for numerical simulations. For

model tests, both fixed and free model (e.g., free to pitch and heave) should be used since a large amount of computations are performed for both cases;

- In the aspect of numerical computations, computed results of resistance highly depend on the mesh as well as the settings in the code. In shallow water, items that should be evaluated include, but is not limited to, the performance of different turbulence models, the determination of  $y^+$ , the density of mesh, and computational domain. Meanwhile, numerical results should be validated to assure an acceptable level of accuracy.

To sum up, the prediction of ship resistance in shallow water has been developed in the past with several practically accurate corrections. However, the physical basis of those methods is incorrect, and individual corrections for shallow water effects on each resistance component can make the prediction more robust. Publically available experiments of ship resistance in shallow water are, however, not adequate for validations.

In the following chapters, a model test of an inland ship sailing in shallow water will be introduced (Chapter 3), and physical understandings of how different resistance components are altered in shallow water will be discussed based on numerical computations (Chapters 4 to 6).



# 3

## A Benchmark Test of Ship Resistance in Shallow Water

In the previous chapter, the experimental and numerical methods applied to obtain ship resistance in shallow water have been reviewed. It has been shown that publicly available data of ship model tests is insufficient, and this acts as the motivation of this chapter. Observing ship's behavior in shallow water can provide physical impressions as well as measurements applied to validate numerical results. In this chapter, a 1/30 scaled model of an 86-meter inland ship was selected, and the resistance tests were performed in various water depths. Due to the width limitation of the applied towing tank, blockage effects will occur in some cases. Therefore in this chapter, the critical speed in confined water will be applied in the analysis. In later chapters, where the blockage effects are eliminated in computations, the critical velocity in open shallow water will be used. The experimental results will be applied in Chapter 5 to validate the CFD results of form factor, and also can be used by other researchers working on a similar topic.

### 3.1. Introduction

For sea-going ships in deep water, plenty of experimental data can be found, especially for “standard” ship types like the Duisburg Test Case (DTC) (Moc-tar et al., 2012). Schlichting (1934) performed a number of ship resistance tests in shallow water, but the ships applied are cruisers, which cannot be seen as representatives for inland ships that usually has a fuller shape.

---

This chapter is based on the paper: Zeng, Q., Thill, C., & Hekkenberg, R., 2018. A benchmark test of ship resistance in extremely shallow water. Progress in Maritime Technology and Engineering: Proceedings of the 4th International Conference on Maritime Technology and Engineering (MARTECH), Lisbon, Portugal. (Zeng et al., 2018).

Jiang (2001) did some tests with a typical inland ship, and his method is only applicable for moderately shallow water (water depth-to-draft ratio  $h/T \geq 1.5$ ). A more recent test with  $h/T$  at 1.2 was performed by Mucha et al. (2017), but no results are available for other water depths. Therefore, the existing experimental data is insufficient for the validations of CFD computations, and more experimental data is required.

In this chapter, resistance tests of an 86 m inland ship model (bare hull) in shallow and calm water are performed in the smaller towing tank at TU Delft. Four different shallow water cases are implemented, and one deep-water case is added for comparison. The depth Froude number ( $F_{T_h}$ ) varies from 0.1 to 0.75, which covers the typical speed range used by most inland vessels. Additionally, the uncertainties of the measuring instruments, as well as the results of resistance, trim, and sinkage, are evaluated according to the guidelines of ITTC (2017g).

## 3.2. Test Model and Scheme

### 3.2.1. Test Model

A hybrid wood-foam ship model (Figure 3.1) is used in this test. This is a 1/30 scaled model of an inland ship with the main parameters shown in Table 3.1.



Figure 3.1: The 1/30 scaled model of an inland ship in towing tank

Sand strips are used to stimulate a turbulent flow at three positions:  $x = 2.787$  m (close to the starting point of the bow),  $x = 2.487$  m (transition point to the parallel midbody), and  $x = 2.187$  m (on the parallel midbody). The strips are 40 mm wide and have an experimentally validated resistance coefficient of 0.01.

The towing tank is 85 m long, 2.75 m wide and with the maximum carriage speed of 3 m/s. The water depth of the tank can be adjusted within the range from 0 m to 1.25 m to realize all shallow water cases planned in the test.

Table 3.1: Main parameters of both the model and full-scale ship

	symbol	unit	model	full-scale
Scale	$\lambda$	-	1/30	1
Length	$L$	m	2.867	86.0
Beam	$B$	m	0.380	11.4
Draft	$T$	m	0.117	3.5
Mass	$M$	kg	109.190	2948118
Wetted surface	$S$	m <sup>2</sup>	1.575	1417.8
Block coefficient	$C_B$	-	0.864	0.864

### 3.2.2. Test scheme

In this test, four cases of shallow water with  $h/T$  of 2.0, 1.8, 1.5, and 1.2 are selected. One case of deep water ( $h/T = 10.71$ , the deepest condition for this towing tank) is applied for comparison.

In general, the design speed of an inland ship is in the range of 10 - 18 km/h. In this chapter, this range is expanded to 6 - 22 km/h not only to include more navigation conditions but also to cover a large enough part of the speed range. The values of depth Froude number ( $Fr_h = V/\sqrt{gh}$ , where  $V$  is ship's speed) for each case are shown in Table 3.2.

Table 3.2: The depth Froude number for each case

$V$ (m/s)	$V$ (km/h)	Depth Froude number ( $Fr_h$ )				
		$h/T$	$h/T$	$h/T$	$h/T$	$h/T$
1/30 model	full-scale	10.71	2.01	1.8	1.5	1.2
0.3	5.92	0.086	0.198	0.209	0.229	0.256
0.4	7.89	0.114	0.263	0.279	0.305	0.341
0.5	9.86	0.143	0.329	0.348	0.382	0.427
0.6	11.83	0.171	0.395	0.418	0.458	0.512
0.7	13.80	0.200	0.461	0.488	0.534	0.597*
0.8	15.77	0.228	0.527	0.557	0.611*	-**
0.9	17.75	0.257	0.593	0.627*	0.687*	-
1.0	19.72	0.286	0.659*	0.697*	0.763*	-
1.1	21.69	0.314	0.724*	0.766*	-	-

\* Cases that might be in the critical or supercritical speed range of this test.

\*\* To avoid grounding, cases marked "-" were not performed.

Due to the width limitation of the applied towing tank, blockage effects may occur. For research purposes, part of the cases listed in Table 3.2 will enter the critical or the supercritical speed region to study the changes in resistance. The critical speed ( $V_{cr}$ ) can be predicted using the equation (Briggs et al., 2010) as follows:

Table 3.3: Critical speed (m/s) for each water depth

$h/T$	10.71	2.01	1.80	1.50	1.20
$V_{cr}$ (m/s)	3.018	1.040	0.959	0.835	0.699

$$V_{cr} = \sqrt{gh} \cdot \left[ 2 \sin \left( \frac{\text{Arcsin}(1 - B_C)}{3} \right) \right]^{3/2} \quad (3.1)$$

where  $h$  is water depth and  $B_C$  the blockage coefficient, which is the ratio between the area of ship's midsection and the area of the wetted waterway section. The calculated critical speed for each water depth in this test is shown in Table 3.3. The cases that are estimated to be within the critical or the supercritical regions are marked in Table 3.2.

### 3.3. Sources and Propagation of Uncertainties

For ship resistance tests, uncertainties will be generated throughout the test process and propagate into the final results of resistance, trim, and sinkage. Based on the guidelines suggested by ITTC (2017g), the sources of uncertainty can be grouped into five categories: geometry, installation, calibration, repeat measurement, and data reduction. Most items in each group are listed in Figure 3.2. Each group is discussed in the following subsections.

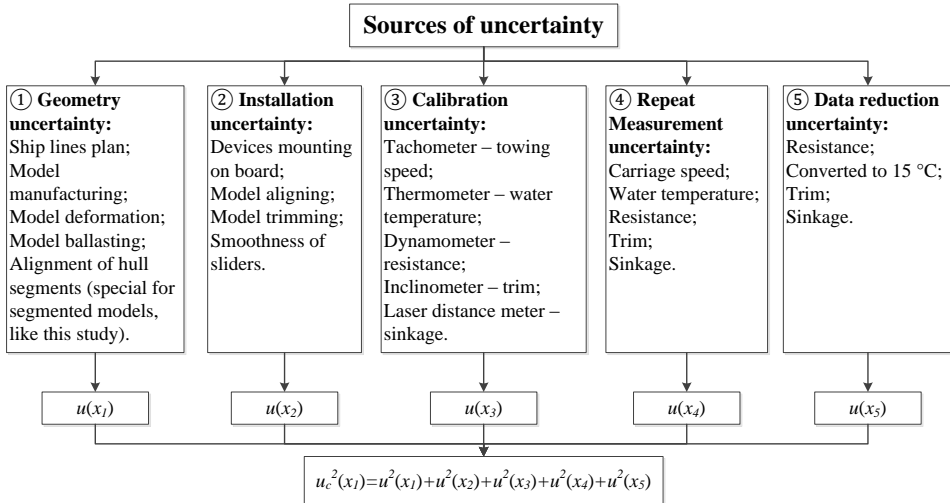


Figure 3.2: Sources of uncertainty in ship resistance test



Figure 3.3: Geometry check at three sections that shift 220 mm (stern), 1430 mm (parallel body), 2640 mm (bow) from the end of stern (the inner curve on each section model offset 2 mm deliberately from the prototype, and this gap is checked on more than 20 positions per section between the section model and hull surface).

### 3.3.1. Hull Geometry

A scaled model is built based on the provided lines plan. Uncertainty might result from possible deviations between the physical model and the prototype. The deviations can cause a different displacement and/or different wetted surface, which will propagate into the final results (e.g., the resistance). In this test, the parallel midship segment of the model used was constructed by trained engineering staff, and NC (Numerical Control) milling was applied at the bow and the stern. After checking three sections, i.e., each for the bow, parallel body, and stern, the errors are less than 0.5 mm which is considered as acceptable, as shown in Figure 3.3.

Also, the total weight, including all hull segments, the measuring equipment, and all the ballast bricks, of the model at the designed waterline has less than 0.1% error when compared with the expected displacement.

Therefore, the error caused by hull geometry is deemed as negligible.

### 3.3.2. Test Installation

This group of sources of uncertainty relates to the drift angle, the alignment of the direction of the dynamometer with the ship model's centerline, and other aspects of the test mounting.

During ship resistance tests, the model should be ballasted to its designed waterline. A deviation can cause an uncertainty into the displacement ( $u(\Delta)$ ). Consequently, an uncertainty is generated into the wetted surface and then propagates into the value of resistance. The wetted surface is assumed to be a two-thirds power of the volume ( $S \propto \Delta^{2/3}$ ). Therefore, the relative uncertainty of the wetted surface ( $u'(S)$ ) can be represented as

$$u'(S) = \frac{u(S)}{S} = \left( \frac{u(\Delta)}{\Delta} + 1 \right)^{2/3} - 1. \quad (3.2)$$

As the wetted surface area has linear effects on ship resistance, the influence of the deviation of the displacement on the resistance can be easily derived.

For the tests in shallow water, if the model is not ballasted to the designed waterline, the water depth will change accordingly. The resistance, trim, and sinkage in shallow water, which depend on the water depth, will be affected by the mismatched draught. In this test, the ship model and the measuring instruments are carefully mounted, and the quality of the installation is guaranteed (e.g., the drift angle is within 0.1 degrees, the initial trim is less than 0.1 degrees). Therefore, the uncertainty caused by the test installation into the final results is deemed negligible.

### 3.3.3. Instrument Calibration

In this section, the calibrations of the instruments for measuring forces, trim, sinkage, and temperature are illustrated sequentially.

#### Dynamometer for Resistance

Two dynamometers are chosen for the measurements of drag force. One is for the towing point in the front of the model, which absorbs the majority of force; the other is at the back and connected with a slider (free to move back and forth). Meanwhile, the predicted maximum drag of the ship in shallow water is 30 N. Considering the fact that a three to four times larger force may occur when the carriage launches, two dynamometers with a range of 100 N and 50 N are used for the front and the back, respectively.

According to the [ITTC \(2017i\)](#), end-to-end calibrations were performed for the dynamometers, in both the positive and the negative direction. By regularly adding the masses to the maximum and then reducing them to zero, changes of forces against the voltage are shown in Figure 3.4.

The calibration factor  $k_R$  for resistance is defined as

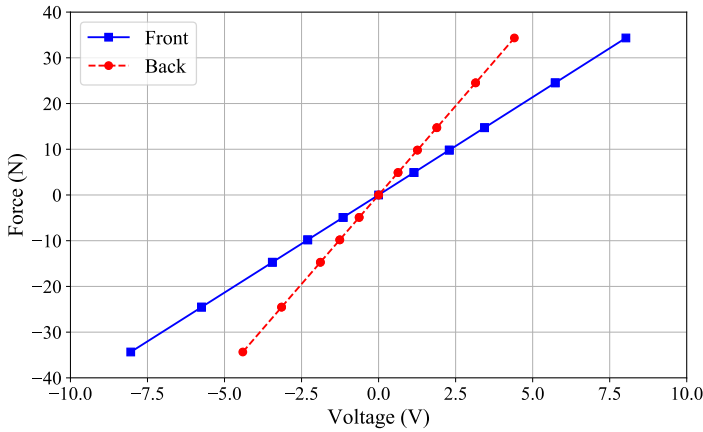


Figure 3.4: The forces against the voltages for the front and the back dynamometers

$$Force(N) = Voltage(V) \times k_R. \quad (3.3)$$

The value of  $k_R$  and its standard uncertainty ( $u(k_R)$ ), as well as the relative uncertainty ( $u'(k_R)$ ), are shown in Table 3.4.

Table 3.4: The calibration factors  $k_R$  of the dynamometers and the uncertainties

Dynamometer position	$k_R$	$u(k_R)$	$u'(k_R)$
Front	7.787	0.013	0.17%
Back	4.273	0.007	0.16%

The uncertainties of the dynamometers will directly propagate into the measurements of the resistance.

### Inclinometer for Trim

An inclinometer is applied to measure the trim angle, which is mounted at the center of gravity. Errors and uncertainties caused by a deviation from the center of gravity during the test are negligible. The calibration factor  $k_{Tr}$  is defined based on the average angle ( $\theta_A$ , in degree) and the measured angle ( $\theta_M$ , in degree):

$$\theta_A = \theta_M \times k_{Tr}. \quad (3.4)$$

$k_{Tr}$  and its standard uncertainty ( $u(k_{Tr})$ ) and relative uncertainty ( $u'(k_{Tr})$ ) are shown in Table 3.5.

The uncertainty of the inclinometer will directly propagate into the measurements of the trim angle.

Table 3.5: The calibration factor  $k_{Tr}$  of the inclinometer and the uncertainties

Device	$k_{Tr}$	$u(k_{Tr})$	$u'(k_{Tr})$
Inclinometer	1.00	0.043	4.26%

### Laser Distance Meter for Sinkage

The sinkage is measured by a laser distance meter, which is fixed at the same longitudinal position as the center of gravity of the model. The resolution of this device is sufficiently high (0.1 mm).

The calibration factor  $k_{Si}$  for the sinkage measurements is defined as follows:

$$Distance(mm) = Voltage(V) \times k_{Si}. \quad (3.5)$$

$k_{Si}$  and its standard uncertainty ( $u(k_{Si})$ ) and relative uncertainty ( $u'(k_{Si})$ ) are shown in Table 3.6.

Table 3.6: The calibration factors  $k_{Si}$  of the laser distance meter and the uncertainties

Device	$k_{Si}$	$u(k_{Si})$	$u'(k_{Si})$
Laser distance meter	6.601	0.056	0.85%

The uncertainty of the laser distance meter will directly propagate into the measurements of sinkage.

### Thermometer for Water Temperature

The temperature in the water was regularly recorded with a thermometer, which has a resolution of 0.1°C. Five positions selected for recording distributed evenly along with the towing tank. As the test was performed in a short time (18-28 July 2017), the results show that variations of temperature are small (range: 19.4 °C - 19.6°C).

The calibration factor  $k_{Te}$  for temperature measuring is defined based on the average temperature ( $T_A$ ) and the measured temperature ( $T_M$ , in °C):

$$T_A = T_M \times k_{Te}. \quad (3.6)$$

$k_{Te}$  and its standard uncertainty ( $u(k_{Te})$ ) and relative uncertainty ( $u'(k_{Te})$ ) are shown in Table 3.7.

Table 3.7: The calibration factor  $k_{Te}$  of the thermometer and the uncertainties

Device	$k_{Te}$	$u(k_{Te})$	$u'(k_{Te})$
Thermometer	1.00	0.0042	0.42%

The uncertainty of the thermometer will directly propagate into the measurements of temperature, which affects the density and viscosity of the water. As discussed in ITTC (2017f), when the temperature is changed by 0.1 °C (at 20°C), the change of density and viscosity can be estimated as ±0.0021% and ±1%, respectively. Therefore, the relative uncertainties of density ( $u'(\rho)$ ) and viscosity ( $u'(\mu)$ ) in this test, considering the uncertainty of thermometer, can be estimated as ( $T_A$  is 19.5 °C in this test)

$$u'(\rho) = \frac{u(\rho)}{\rho} = \pm \frac{19.5 \times 0.42\%}{0.1} \times 0.0021\% = 0.0017\%; \quad (3.7)$$

$$u'(\mu) = \frac{u(\mu)}{\mu} = \pm \frac{19.5 \times 0.42\%}{0.1} \times 1\% = 0.819\%. \quad (3.8)$$

### Tachometer for Carriage Velocity

A tachometer is installed on the carriage, which is used to indicate the towing velocity. The calibration factor  $k_V$  for the tachometer is defined based on the average velocity ( $V_A$ , in m/s) and the measured velocity ( $V_M$ , in m/s):

$$V_A = V_M \times k_V. \quad (3.9)$$

$k_V$  and its standard uncertainty ( $u(k_V)$ ) and relative uncertainty ( $u'(k_V)$ ) are shown in Table 3.8.

Table 3.8: The calibration factor  $k_V$  of the tachometer and its uncertainties

Device	$k_V$	$u(k_V)$	$u'(k_V)$
Tachometer	1.00	0.0004	0.04%

The uncertainty of the tachometer will propagate into the calculation of the total resistance coefficient.

### 3.3.4. Repeating Tests

If an average of the results is used, the standard uncertainty and the relative standard uncertainty can be represented as follows:

#### For Single Measurement

1000 samples were recorded within a unit time (1 second). A moving average ( $\hat{x}_i$ ) with an interval of 1000 is taken for the results of resistance, trim, and sinkage. The number of time units during the effective time range (when the recording result is stable) is expressed with the symbol  $n$ . The measured value ( $x_i$ ) and its uncertainty can be derived as

$$x_i = \frac{1}{n} \sum_{i=1}^n \hat{x}_i, \quad u(x_i) = \sqrt{\frac{1}{n} \sum_{i=1}^n (\hat{x}_i - x_i)^2}, \quad u'(x_i) = \frac{u(x_i)}{x_i}. \quad (3.10)$$

It should be mentioned that after the tests, a method named “Transient Scanning Technique” (TST) was recommended by ITTC procedures (ITTC, 2017d) for a single measurement. The TST method has a good performance to determine whether a signal approaches a stationary state and therefore, the mean value can be achieved more accurately.

For Repeating Tests (repeat  $N$  times)

$$\bar{x}_i = \frac{1}{N} \sum_{i=1}^N x_i, \quad u(\bar{x}_i) = \sqrt{\frac{1}{N} \sum_{i=1}^N (x_i - \bar{x}_i)^2}, \quad u'(\bar{x}_i) = \frac{u(\bar{x}_i)}{\bar{x}_i}. \quad (3.11)$$

### 3.4. Data Reduction

Conventionally, the results of the total resistance need to be converted into the condition that the temperature is 15 °C. The following relation is usually applied (ITTC, 2017e):

$$\frac{R_t(15^\circ\text{C})}{R_t(t_i)} = \frac{\rho(15^\circ\text{C})}{\rho(t_i)} \left[ 1 + \frac{C_f(15^\circ\text{C}) - C_f(t_i)}{C_t(t_i)} \right], \quad (3.12)$$

where  $t_i$  is the temperature during the test,  $C_f$  can be estimated by the ITTC57 correlation line for deep water. However, as will be discussed in the next chapter, the ITTC 57 line is not applicable in shallow water, and the exact expression for friction prediction in shallow water is not available. Therefore, all the results of the total resistance in this test will be expressed under the exact temperature.

In this test, the data reduction for the coefficient of ship resistance can be represented as

$$C_t = \frac{R_t}{0.5 \cdot \rho V^2 S}. \quad (3.13)$$

The measurements of resistance ( $R_t$ ), water density ( $\rho$ ), ship velocity ( $V$ ), and wetted surface ( $S$ ) are independent. Therefore, the uncertainty of  $C_t$  can be written as follows (ITTC, 2017h):

$$u^2(C_t) = \left( \frac{\partial C_t}{\partial R_t} \right)^2 u^2(R_t) + \left( \frac{\partial C_t}{\partial \rho} \right)^2 u^2(\rho) + \left( \frac{\partial C_t}{\partial V} \right)^2 u^2(V) + \left( \frac{\partial C_t}{\partial S} \right)^2 u^2(S). \quad (3.14)$$

Based on the analyses in the above subsections, the standard uncertainty of  $C_t$  can be written as

$$u(C_t) = \sqrt{\left( \frac{2}{\rho V^2 S} \right)^2 \cdot u(k_R) + \left( \frac{2R_t}{\rho^2 V^2 S} \right)^2 \cdot u(\rho) + \left( \frac{4R_t}{\rho V^3 S} \right)^2 \cdot u(k_V) + \left( \frac{2R_t}{\rho V^2 S^2} \right)^2 \cdot u(S)}. \quad (3.15)$$

As discussed in Section 3.3.2,  $u(S) \approx 0$ . Therefore,  $u(C_t)$  can be rewritten as

$$u(C_t) = \sqrt{\left(\frac{2}{\rho V^2 S}\right)^2 \cdot u(k_R) + \left(\frac{2R_t}{\rho^2 V^2 S}\right)^2 \cdot u(\rho) + \left(\frac{4R_t}{\rho V^3 S}\right)^2 \cdot u(k_V)}. \quad (3.16)$$

The above equation is the uncertainty of a single test on the measuring instrument, and the uncertainty of repeating tests can follow the method introduced in section 3.3.4.

For trim and sinkage, the uncertainties of trim ( $u(trim)$ ) and sinkage ( $u(sinkage)$ ) can be derived from the calibration of the inclinometer and laser distance meter:

$$u(trim) = u(k_{Tr}); u(sinkage) = u(k_S). \quad (3.17)$$

### 3.5. Results and Uncertainty Evaluations

During the test, the average temperature in the water in the towing tank is 19.5°C (range: 19.4 °C - 19.6°C). Therefore, the corresponding density is 998.3091 kg/m<sup>3</sup>, and the dynamic viscosity is 0.001014 Pa·s. The signs of the resistance, trim, and sinkage and are defined as follows:

- resistance is positive pointing to the stern;
- trim is positive with bow up;
- sinkage is positive downwards.

The results of the total resistance and its coefficient are shown in Figure 3.5. A detailed view of the drag force from 0 N to 8 N and the corresponding error bars are shown in Figure 3.6. Some extra towing speeds in addition to Table 3.2 were added where necessary (e.g., the range  $Fr_h = 0.6 - 0.8$ ).

Compared with the deep water case ( $h/T = 10.71$ ), the drag force on ship hull increases in shallow water. As will be illustrated through Chapters 4 to 6, all the three main resistance components increase significantly due to shallow water effects at  $1.2 \leq h/T \leq 4.0$ . When the depth Froude number ( $Fr_h$ ) is around 0.7, significant increases in the drag force are observed. Furthermore, for the same velocity, a smaller  $h/T$  will lead to an earlier change of the drag.

It should be pointed out that a “turning point” ( $V = 1.0$  m/s at  $h/T = 1.80$ ) is observed in the right part of Figure 3.5, i.e., when the speed goes up to a certain value, the value of  $C_t$  begin to drop. This is a typical phenomenon in the supercritical speed region.

The resulting total resistance coefficient ( $C_t$ ) and uncertainties are shown in Table 3.9 and the cases that were tested by multiple times are marked.

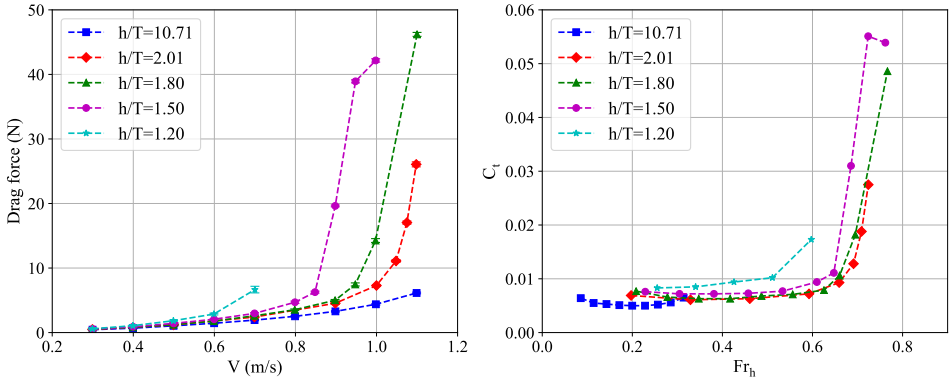


Figure 3.5: Results of total resistance (drag force) against the velocities with error bar (left) and the total resistance coefficient ( $C_t$ ) against the depth Froude number ( $Fr_h$ ) (right)

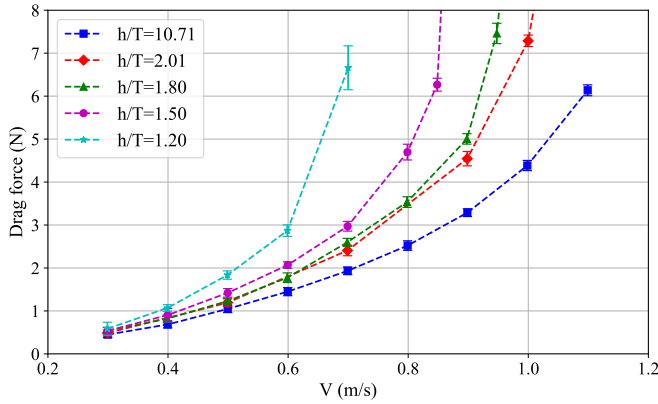


Figure 3.6: Detailed view of the left graph in Figure 3.5 with the drag force from 0 N to 8 N

Results of the trim against both velocity and  $Fr_h$  are shown in Figure 3.7. The reverse trend of trim indicates that the corresponding cases are among the critical or the supercritical speed ranges. The dynamic pressure at the bow becomes strong enough to raise the bow up. A detailed view of the trim range from 0 degrees to -0.5 degrees is shown in Figure 3.8. The relative uncertainty (in percentage) for the sinkage are shown in Table 3.10.

Results of the sinkage against both velocity and  $Fr_h$  are shown in Figure 3.9. The decrease of sinkage at  $Fr_h \approx 0.7$  for  $h/T = 2.0$ , 1.8, and 1.5 indicates supercritical speed regions. A detailed view of the sinkage range from 0 mm to 20 mm is shown in Figure 3.10. The relative uncertainty (in percentage) for the sinkage are shown in Table 3.11.

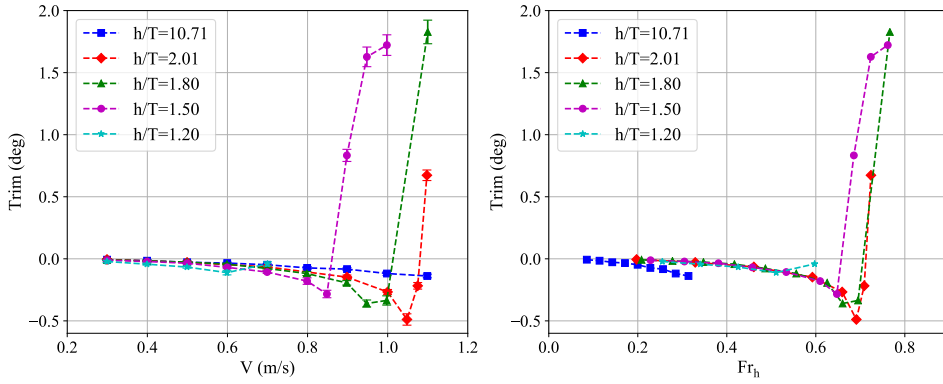


Figure 3.7: Results of trim against the velocities with error bar (left) and the trim against the depth Froude number ( $Fr_h$ ) (right)

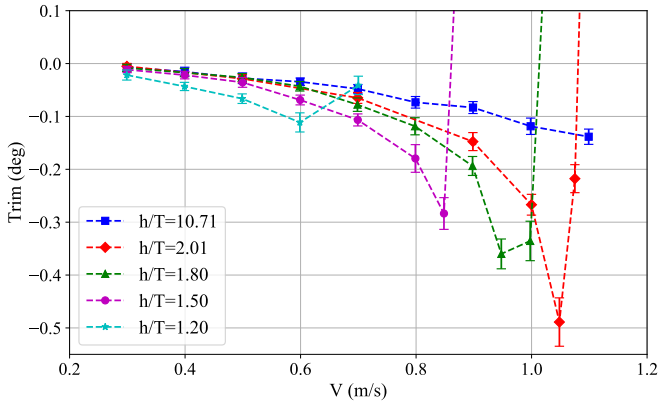


Figure 3.8: Detailed view of the left graph in Figure 3.7 with the trim from 0 deg to -0.5 deg

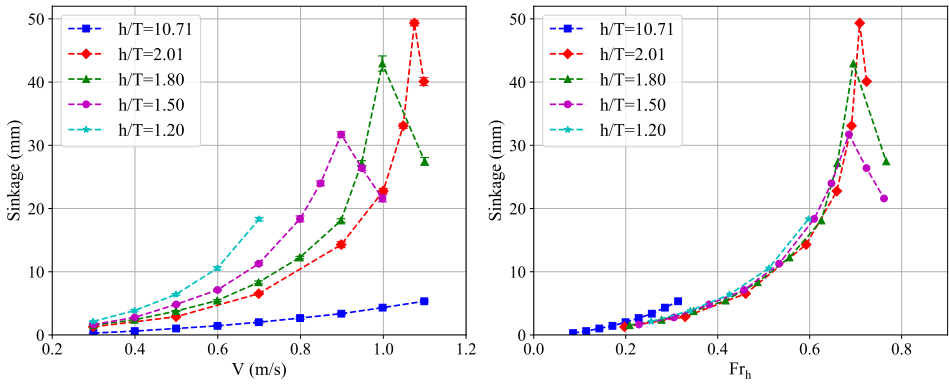


Figure 3.9: Results of sinkage against the velocities with error bar (left) and the sinkage against the depth Froude number ( $Fr_h$ ) (right)

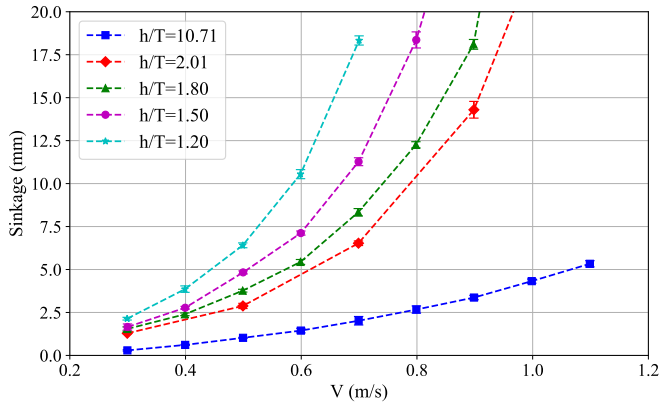


Figure 3.10: Detailed view of the left graph in Figure 3.9 with the sinkage from 0 mm to 20 mm

Table 3.9: The Results of total resistance coefficient ( $C_t$ ) and uncertainties (the sign is  $\pm$ )

V (m/s)	h/T											
	10.71		2.01		1.80		1.50		1.20			
	$C_t \times 10^3$	Uncertainty										
0.30	6.37*	15.42%	6.92	14.22%	7.68	14.88%	7.62	13.84%	8.34	25.58%		
0.40	5.47*	11.74%	-	-	6.56	10.35%	7.21	17.09%	8.53	7.35%		
0.50	5.35*	8.29%	6.09	7.48%	6.28	5.72%	7.25	6.98%	9.39	5.31%		
0.60	5.13	6.59%	-	-	6.30	6.34%	7.33	3.67%	10.18	4.72%		
0.70	5.03**	4.63%	6.27	5.09%	6.77	3.57%	7.74	3.81%	17.30	7.67%		
0.80	5.03	4.42%	-	-	7.06	3.51%	9.37	3.90%	-	-		
0.85	-	-	-	-	-	-	11.08	2.39%	-	-		
0.90	5.18*	2.76%	7.16	3.68%	7.90	2.43%	30.96	0.71%	-	-		
0.95	-	-	-	-	10.57	3.17%	55.11	0.60%	-	-		
1.00	5.60*	2.71%	9.28	1.84%	18.23	2.10%	53.88	0.62%	-	-		
1.05	-	-	12.85	1.95%	-	-	-	-	-	-		
1.075	-	-	18.77	1.43%	-	-	-	-	-	-		
1.10	6.47*	2.06%	27.51	1.47%	48.59	0.66%	-	-	-	-		

\* repeated twice;

\*\* repeated three times.

Table 3.10: The results of the trim ( $^{\circ}$ ) and uncertainties (the sign is  $\pm$ )

$V$ (m/s)	$h/T$											
	10.71		2.01		1.80		1.50		1.20			
	Trim ( $^{\circ}$ )	Uncertainty										
0.30	-0.01	93.78%	-0.01	104.64%	-0.01	83.35%	-0.01	49.69%	-0.02	43.89%		
0.40	-0.02	54.86%	-	-	-0.02	45.83%	-0.02	32.89%	-0.04	17.89%		
0.50	-0.03	36.47%	-0.03	26.53%	-0.03	27.97%	-0.04	26.00%	-0.07	13.62%		
0.60	-0.03	20.40%	-	-	-0.04	20.83%	-0.07	13.43%	-0.11	16.27%		
0.70	-0.05	17.19%	-0.07	15.85%	-0.08	16.35%	-0.11	10.70%	-0.04	42.13%		
0.80	-0.07	14.94%	-	-	-0.12	13.63%	-0.18	14.57%	-	-		
0.85	-	-	-	-	-	-	-0.28	10.58%	-	-		
0.90	-0.08	13.57%	-0.15	11.54%	-0.19	9.26%	0.83	5.86%	-	-		
0.95	-	-	-	-	-0.36	7.83%	1.63	4.86%	-	-		
1.00	-0.12	13.04%	-0.27	7.36%	-0.34	11.12%	1.72	4.82%	-	-		
1.05	-	-	-0.49	9.36%	-	-	-	-	-	-		
1.075	-	-	-0.22	12.16%	-	-	-	-	-	-		
1.10	-0.14	10.44%	0.67	6.31%	1.83	5.20%	-	-	-	-		

Table 3.11: The results of the sinkage (mm) and uncertainties (the sign is  $\pm$ )

V (m/s)	$h/T$											
	10.71		2.01		1.80		1.50		1.20			
	Sinkage (mm)	Uncertainty										
0.30	0.29	13.53%	1.29	2.09%	1.54	7.83%	1.66	10.62%	2.14	3.70%		
0.40	0.61	4.03%	-	-	2.39	3.27%	2.78	2.81%	3.86	4.87%		
0.50	1.03	2.62%	2.88	5.28%	3.77	2.17%	4.83	1.82%	6.41	2.19%		
0.60	1.45	9.26%	-	-	5.44	2.60%	7.12	1.67%	10.55	2.50%		
0.70	2.02	12.22%	6.53	2.06%	8.33	2.57%	11.27	2.04%	18.33	1.46%		
0.80	2.67	7.82%	-	-	12.26	1.48%	18.36	2.55%	-	-		
0.85	-	-	-	-	-	-	23.98	1.61%	-	-		
0.90	3.37	3.76%	14.30	3.40%	18.10	1.57%	31.71	1.38%	-	-		
0.95	-	-	-	-	27.18	1.44%	26.39	1.39%	-	-		
1.00	4.32	2.82%	22.76	1.83%	42.94	2.80%	21.59	2.43%	-	-		
1.05	-	-	33.09	1.21%	-	-	-	-	-	-		
1.075	-	-	49.33	0.90%	-	-	-	-	-	-		
1.10	5.33	3.40%	40.10	1.53%	27.46	2.24%	-	-	-	-		

### 3.6. Concluding Remarks

In this chapter, four shallow water cases ( $h/T = 1.2, 1.5, 1.8, \text{ and } 2.0$ ) were used to conduct benchmark tests of an inland ship model. One deep-water case ( $h/T=10.71$ ) was added for comparison. The depth Froude number ( $Fr_h$ ) varies from 0.1 to 0.75, which covers the subcritical speed range and a part of critical and supercritical speed range in confined water. It was confirmed that ship's resistance, trim, and sinkage deviate significantly compared to deep water.

The uncertainties of the measuring instruments, as well as the resistance, trim, and sinkage, were evaluated. Results of the resistance, trim, and sinkage in different shallow water conditions were expressed with graphs, which build a database for this benchmark test. This test showed the path for the ongoing research on improving the prediction method of ship resistance in the shallow water. It also provides the benchmark for the validation of CFD calculations in this research.

# 4

## A Shallow Water Friction Line in 2D Cases

In Chapter 2, it was recommended that shallow water effects on each resistance component should be studied separately based on its physical basis. Following this approach, this chapter starts with the frictional resistance, which is generally the major part of resistance for most inland vessels. The ITTC57 correlation line, which is suggested by ITTC guidelines (ITTC, 2017j) for the prediction of ship's friction, was derived based on the assumption that the water is infinitely deep and wide. However, for vessels sailing in waterways with limited water depth, the frictional resistance is influenced, leading to a decreasing accuracy of the prediction with the ITTC57 correlation line. In this chapter, it will be shown that the ITTC57 line is more than 20% smaller in certain water depths, and a modification for this line is proposed specifically for the flat area of the bottom of the ship. This area can be simplified to a two-dimensional (2D) flat plate with a parallel wall close to it to study how limited space affect the flat plate friction coefficient. Computational Fluid Dynamics (CFD) calculations are applied as the main tool to build the dataset. As the relative boundary layer thickness differs from model to full scale, such deviations may cause severe scale effects when extrapolating ship resistance from model scale and, therefore, affect the accuracy of ship's performance prediction. The proposed modification can be used to improve the prediction of the frictional resistance of those ships with a large area of flat bottom and sail in shallow water.

---

This chapter is based on the paper: Zeng, Q., Thill, C., Hekkenberg, R., & Rotteveel, E. (2019). A modification of the ITTC57 correlation line for shallow water. *Journal of Marine Science and Technology*, 24(2), 642-657. (Zeng et al., 2019d).

## 4.1. Introduction

An improved understanding of the characteristics of friction/correlation lines in various conditions can contribute a better model-ship extrapolation, which is in turn beneficial for ship design and optimization. Such prediction is based on the understanding of the boundary layer theory and friction lines derived from a flat plate. In the past century, researchers have provided several friction lines, e.g. Schoenherr (1932), Grigson (1999) and Katsui et al. (2005), based on the results of experiments and/or numerical simulations. However, the incoming flow applied in those research is unrestricted, and the pressure gradient along the flat plate can be assumed as zero.

In fact, shallow water condition is commonly found in inland waterways and coastal area. Various researchers (Jiang, 2001; Lackenby, 1963; Roemer, 1940) provided ways to predict the resistance in shallow water but without specifically and physically discussing the changes of the frictional resistance. This chapter will focus on the effects on the flat plate friction in intermediate pure shallow water with  $h/T \geq 1.2$ . The inflow conditions in the space between ship's and fairway's bottom are subject to changes especially in extremely shallow water ( $h/T < 1.2$ ), where the thickness of the boundary layer is approaching under-keel clearance (*UKC*), and these effects will be introduced in Chapter 5.

For waterways with unlimited width, shallow water mainly affects the bottom area of the ship. Since the ITTC57 correlation line was not designed for shallow water, it should be corrected for shallow water effects.

Generally, most inland ships sailing in shallow water have a long parallel midbody and a large area of the flat bottom. The characteristics of the flow close to the bottom are comparable to the flow passing over a 2D flat plate, as shown in Figure 4.1 (this is further illustrated in Section 4.2.1). The velocity of far-field incoming water is  $V$  (ship-based coordinate system), and the water underneath the ship is accelerated by  $\Delta V$  (due to the displacement of the ship and the limitation of the waterway). This acceleration even happens in deep water but is more obvious in shallow water. Therefore, in the simplification, the speed of incoming water for the flat plate should be  $V + \Delta V$ . For illustrating convenience, the symbol  $V$  is still used to represent the velocity for flat plate and revert to  $V + \Delta V$  when calculating ship's friction; similarly, the symbol  $L$  is used for the length of the plate.

A 2D flat plate has been seen as a reasonable simplification for investigating the physics of friction (Grigson, 1999; Katsui et al., 2005). In the research of Eça and Hoekstra (2008), systematic calculations of frictional resistance using CFD have been performed on a flat plate with a number of turbulence models. In their research, the parallel boundary was deliberately set far enough away from the flat plate to avoid shallow water effects. They compared the results when the distances between the flat plate and the parallel boundary were  $0.25L$  and  $0.5L$ , where  $L$  is the length of the plate, and concluded that the differences were too small to be consid-

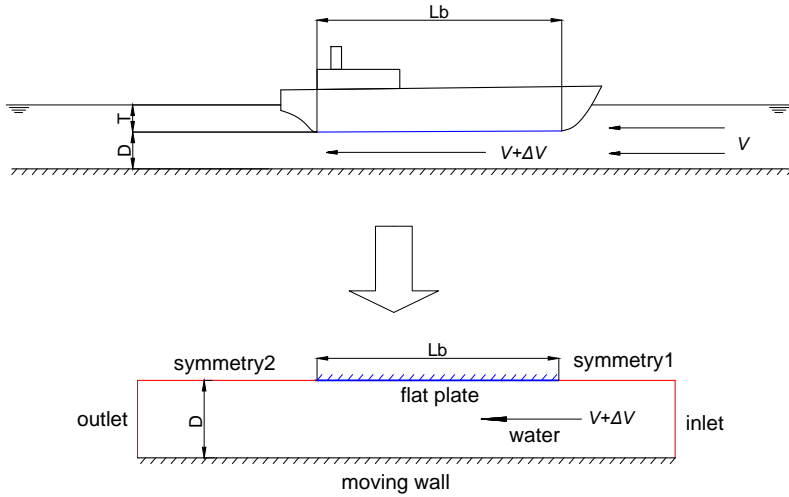


Figure 4.1: Simplification of ship bottom in shallow water (ship-based coordinate system;  $L_b$  is the length of the flat bottom,  $D$  the under keel clearance,  $T$  the draft,  $V$  and  $V + \Delta V$  are the initial and accelerated velocities)

ered. However, a distance less than  $0.25L$  is common in practice, e.g., for some ports and inland waterways, the under-keel clearance might be even smaller than  $0.02L$  (Elout and Vantorre, 2011).

In this chapter, extremely narrow under-keel clearances (up to  $0.01L$ ) are considered. Shallow water effects on the physical details of boundary layer thickness and pressure gradients are investigated using CFD techniques. It is found that both the pressure gradients along with the plate and the friction were affected by the flow confinement. At last, a regression analysis is made based on the CFD results to propose a numerical friction line for the flat plate in shallow water. By applying the ITTC57 correlation line for all wetted surface and applying the proposed line to correct the shallow water effects on a ship's flat bottom, the prediction of ship's frictional resistance in shallow water is improved.

## 4.2. Approach

The feasibility of the 2D flat plate simplification is first discussed. The shallow water conditions were obtained by adjusting the distance between the flat plate and a parallel wall. In this study, calculations were performed in a CFD solver: ANSYS<sup>(TM)</sup> Fluent (version 16.2). The Reynolds number in the simulations was varied from  $10^5$  to  $10^9$  in order to cover the relevant Reynolds numbers for model- and full-scale conditions.

### 4.2.1. Simplification

In practice, reasonable simplification can help to understand the nature of a phenomenon with fewer resources than the original model. In this study, the flow passing above a 2D flat plate was applied to represent the flow close to the flat bottom of inland vessels.

Physically, due to the presence of the bow and the stern, part of the water around a ship will go laterally (3D flow). The control volume 1 shown in Figure 4.2, therefore, cannot be simplified into a 2D case. However, if the control volume is moved from 1 to 2, as shown in Figure 4.2, the 2D simplification is valid.

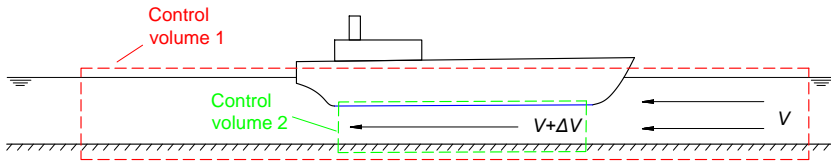


Figure 4.2: The chosen of the control volume

To further illustrate the assumption, an example is shown for an inland vessel. As depicted in Figure 4.3, part of the water flows away from the longitudinal center plane at the bow. These effects shall be considered by appropriate corrections imposed to the inflow boundary conditions for the 2D investigated flat bottom plate. Through this, when the water goes into the space underneath the bottom of the ship, its direction is no longer changed, as shown in the dashed box in Figure 4.3. In this region, the characteristics of the flow are well-nigh comparable to that over a 2D flat plate.

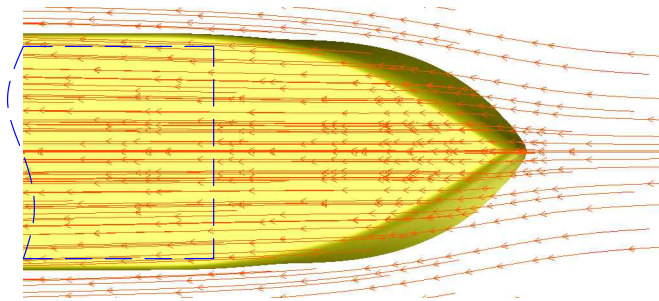


Figure 4.3: An example of water path lines underneath an inland vessel ( $h/T = 1.5$ ,  $V = 0.8$  m/s,  $L = 2.86$  m,  $T = 0.117$  m, the dashed box indicates the area where the 2D simplification is valid)

Therefore, for the control volume 2, it is rational to apply the simplification mentioned at the beginning of this section.

### 4.2.2. Computational Model

The computational domain is shown in Figure 4.4. To pursue a conventional view, the domain is rotated by  $180^\circ$  compared with that in Figure 4.1.

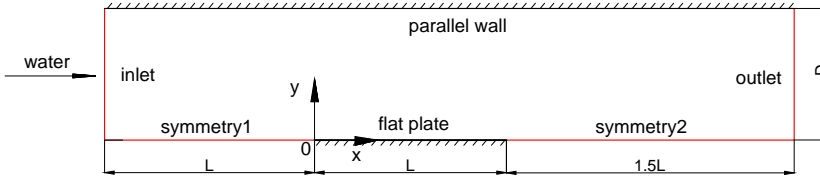


Figure 4.4: Computational domain

The flat plate used in this study is two meters long ( $L$ ), and the domain stretches  $L$  in front of the plate and  $1.5L$  behind it. A geometric progression with a factor of 0.5 is implemented for the distances ( $D$ ) between the parallel wall and the plate, as shown in Table 4.1.

Table 4.1: The seven computational cases ( $D_n$  means the distance between the parallel wall and the flat plate at the case  $n$ )

Case	$D/L$	$D_{n+1}/D_n$
1	1.00	0.32
2	0.32	0.5
3	0.16	0.5
4	0.08	0.5
5	0.04	0.5
6	0.02	0.5
7	0.01	-

Case 1 simulates the deep water condition for comparison. Case 7 is reaching the region of extremely shallow water. For example,  $D/L = 0.01$  means a ship with 100 meters long flat bottom (approximately a class Va vessel in European inland waterways) sails in a shallow waterway with the *UKC* of only one meter (water-depth/ship draft,  $h/T = 1.25$  for  $T = 4$  m).

The flow is the fresh water with a density of  $999.04 \text{ kg/m}^3$  and a kinematic viscosity of  $1.13902 \times 10^{-6} \text{ m}^2/\text{s}$ . Four turbulence models were chosen: three fully-turbulent models (Spalart-Allmaras (SA), BSL  $k-\omega$  and SST  $k-\omega$ ) and one transition model ( $k-kl-\omega$ ).

This study uses ten Reynolds numbers ( $Re$ ) in the range from  $10^5$  to  $10^9$ , as shown in Table 4.2. Different  $Re$  is realized by changing the incident fluid velocity (alternatively, changing the viscosity or the reference length). It should be aware that for  $V = 902.6 \text{ m/s}$ , according to [Fine and Millero \(1973\)](#), the dynamic pressure is around 4000 bar, and the volume of the

water will be about 18% smaller which violates the assumption of incompressibility. However, the incompressibility assumption remains for this case in order to solve the right Navier-Stokes equations at high Reynolds number range.

Table 4.2: Investigated Reynolds numbers

No.	$V(\text{m/s})$	$Re$	$\lg(Re)$
1	0.2267	$3.9811 \times 10^5$	5.6
2	0.5695	$1.0000 \times 10^6$	6.0
3	1.4305	$2.5119 \times 10^6$	6.4
4	3.5934	$6.3096 \times 10^6$	6.8
5	9.0261	$1.5849 \times 10^7$	7.2
6	22.6726	$3.9811 \times 10^7$	7.6
7	56.9510	$1.0000 \times 10^8$	8.0
8	143.0544	$2.5119 \times 10^8$	8.4
9	359.3365	$6.3096 \times 10^8$	8.8
10	902.6125	$1.5849 \times 10^9$	9.2

### 4.2.3. Mesh Generation

The number of grid cells in the x-direction is identical for most cases (mesh was refined for the shallowest cases and part of the high  $Re$  cases), and the distribution of grid cells close to the flat plate is similar for all cases. The number of grid cells in the y-direction decreases with the decrease of the distance ( $D$ ). Additionally, the mesh close to the flat plate and that close to the parallel wall was refined from case 2 to case 7, since shear stress was observed on these boundaries.

Denser grids were generated near the flat plate as well as in the area close to plate's leading and trailing edge, as shown in Figure 4.5 (The number of grid cells in the picture has been reduced for illustration). The "BiGeometric" bunching law (ANSYS, 2015) was applied to the nodes distribution, indicating that the space expansion between the nodes in each direction is linear.

### 4.2.4. Boundary Conditions

#### Inlet boundary

An incompressible, undisturbed flow enters the domain from the inlet with a velocity of  $U_\infty$ . The inlet boundary applies Dirichlet conditions for both velocity and turbulence quantities:

$$u_x = U_\infty, \quad u_y = 0, \quad I \equiv \frac{u'}{U_{ave}} = C_1, \quad \frac{\mu_t}{\mu} = C_2. \quad (4.1)$$

In equation (4.1),  $u_x$  and  $u_y$  are the velocities of upstream flow in  $x$  and

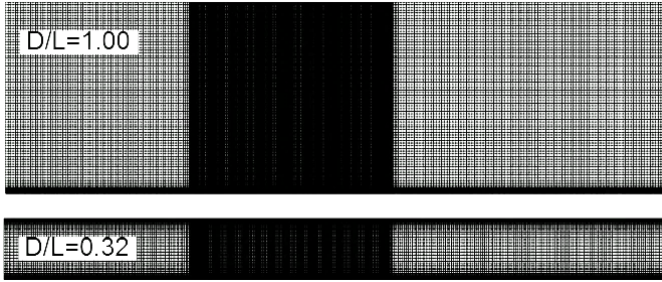


Figure 4.5: Mesh generation

y direction, respectively.  $I$  is the turbulence intensity,  $u'$  the root-mean-square of the turbulent velocity fluctuations,  $U_{ave}$  the Reynolds averaged velocity,  $\mu_t$  the turbulent viscosity, and  $\mu$  the molecular dynamic viscosity.  $C_1$  and  $C_2$  are both constants, which will be chosen in this section.

The static pressure at the inlet boundary is set to zero. The total pressure is not a constant value but will rise to whatever value is necessary to provide the prescribed velocity distribution (ANSYS, 2017b).

In the research of Walters and Cokljat (2008), where the three-equation transition model (k-kl- $\omega$ ) was proposed, different sets of inlet boundary conditions are applied. Similar sets are chosen in this study, as shown in Table 4.3.

Table 4.3: The alternative inlet boundary conditions

Set	$I$ (%)	$\mu_t/\mu$
1	0.9	9
2	0.9	12
3	0.9	100
4	3	9
5	3	12
6	3	100
7	6	9
8	6	12
9	6	100

The computed results of the friction on the flat plate are recorded and shown in percent compared to a randomly chosen set (Set 5:  $I = 3\%$ ,  $\mu_t/\mu = 12$ ), which is listed in Table 4.4. For calculations with the SA model, the friction are compared with the result with  $\mu_t/\mu = 12$ . Two Reynolds numbers are selected in the comparison: one is relatively low ( $Re = 2.51 \times 10^6$ ) for which the transition from laminar flow to turbulent flow is distinct; another one is high ( $Re = 1.58 \times 10^9$ ) for which the turbulent flow is dominant.

Based on Table 4.4, it can be derived that

Table 4.4: Influence of inlet boundary conditions on the results of friction (compare to Set 5, shown in percent, %)

Turbulence model	$I$ %	$\mu_t/\mu$ ( $Re = 2.51 \times 10^6$ )			$\mu_t/\mu$ ( $Re = 1.58 \times 10^9$ )		
		9	12	100	9	12	100
SA	-	-0.37	0.00	4.60	0.00	0.00	0.02
	0.9	-0.05	0.00	0.37	0.00	0.01	0.08
BSL k- $\omega$	3	-0.07	0.00	1.10	-0.01	0.00	0.05
	6	-0.07	-0.02	1.19	-0.01	-0.01	0.03
SST k- $\omega$	0.9	-0.04	-0.01	0.19	0.01	0.02	0.09
	3	-0.04	0.00	0.72	0.00	0.00	0.06
k-kl- $\omega$	6	-0.05	-0.01	0.79	-0.01	0.00	0.04
	0.9	0.05	-0.29	-13.14	-	-	-
k-kl- $\omega$	3	0.24	0.00	87.91	-	-	-
	6	0.07	0.16	92.95	-	-	-

- For the high Reynolds number, the friction is insensitive to different  $I$  and  $\mu_t/\mu$ ; even the maximum difference is less than 0.1%;
- For the relatively low Reynolds number ( $Re = 2.51 \times 10^6$ ), the calculations with the BSL k- $\omega$  and the SST k- $\omega$  model both show insensitivity to inlet boundary conditions (the maximum difference is 1.2%). For the calculations with the SA model, the deviation is larger but still less than 5%. However, for the k-kl- $\omega$  model, the results show big discrepancies especially when  $\mu_t/\mu = 100$  because the value of  $\mu_t/\mu$  affects the position of the “transition point” from laminar flow to turbulent flow, and the k-kl- $\omega$  model is sensitive to such transition;
- For the calculations with fully turbulence models, higher turbulent viscosity ratio ( $\mu_t/\mu$ ) leads to larger value of friction.

Thus, for the BSL k- $\omega$  and SST k- $\omega$  models, the turbulence intensity and turbulent viscosity ratio at the inlet boundary have minor impacts on results. For the SA model, the influence of boundary conditions is noticeable, and for the k-kl- $\omega$  model, the results significantly depend on the boundary conditions. Therefore, the BSL k- $\omega$  and SST k- $\omega$  models are preferred. Further discussions about the selection of a turbulence model are made in verification and validation (see Section 4.3).

#### Other boundary conditions

The “pressure outlet” was set at the outlet boundary. All derivatives of the flow quantities at x direction were set to zero. The position of outlet boundary should be far enough from the flat plate to avoid influencing the gradient of fluid variables in the domain. A study with the outlet boundary

0.5L, 1.0L and 1.5L ( $L = 2\text{m}$ ) away from the trailing edge of the plate is performed to test the influence of the position of the outlet boundary. Results of the pressure gradient behind the plate for each case are shown in Figure 4.6.

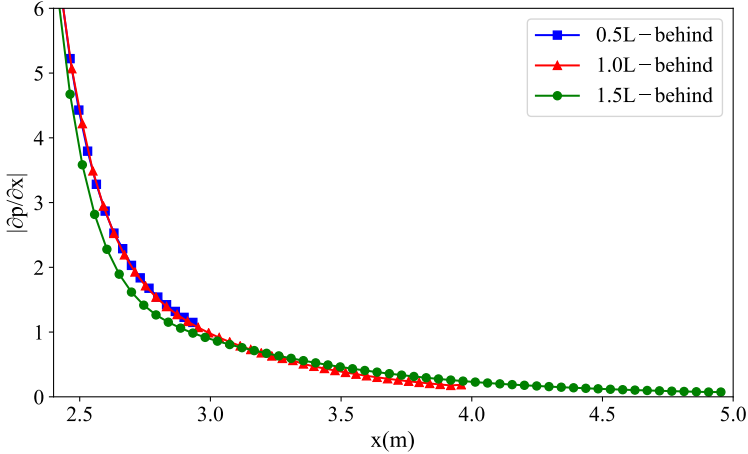


Figure 4.6: Pressure gradient at x direction from the trailing edge to the outlet boundary

For the outlet boundary of 0.5L, 1.0L, and 1.5L behind the flat plate, the pressure gradients to the x-direction near the outlet boundary are 1.149, 0.186, and 0.0074. A value close to zero means the outlet boundary is far enough away and will not affect the flow features. Therefore, the outlet boundary with 1.5L behind the plate is enough for this study.

In addition, for the “backflow” (if any) at the outlet boundary, Dirichlet conditions are set to the turbulence intensity and turbulence-viscosity ratio with the same values as at the inlet boundary.

The parallel wall is set as a non-slip “moving wall” with the same speed as the free stream. All derivatives of the flow quantities in the y-direction are set to zero, and the speed relative to the parallel wall in the x-direction is set to zero.

The flat plate is set as a still, non-slip wall. Dirichlet conditions were set to the velocities, i.e. velocities at x and y directions are zero. Symmetry conditions are set in front and behind the flat plate. The velocity and the derivatives of all flow quantities at the y-direction are set to zero.

### 4.3. Verification and Validation

Numerical simulations shall be verified and validated before application. This is done in sections 4.3.1 and 4.3.2, respectively.

### 4.3.1. Verification

The verification gives the numerical error and uncertainty of a simulation. Typically, a numerical error is the discrepancy between a numerical result and the exact solution. According to Roache (1998), the numerical error contains three components: round-off error, iterative error, and discretization error.

Round-off error results from the finite precision of the computers, but the double precision format can usually keep this error negligible (Eça and Hoekstra, 2009). The iterative error is a consequence of the non-linearity of the mathematical equations. Using the double-precision scheme and a sufficient number of iterations can normally reduce this error to the level of the round-off error. In this study, the convergence criteria of all residuals are set to  $10^{-7}$ . This does not mean the iterative error is  $10^{-7}$ , and actually, this usually keeps the iterative error at the level of  $10^{-9}$ . The discretization error is generated when transforming the partial differential equations into algebraic equations and mostly dominates the numerical error. Therefore, in this chapter, only the discretization error is considered.

A grid refinement study is commonly used to estimate the discretization error (Roache, 1998). At least four grids are recommended (Eça and Hoekstra, 2014) to justify whether the results are in the “asymptotic region”. In this verification, four geometrically similar grids (G1 to G4) with a refinement ratio of 1.6 are generated for the Case1 ( $D/L = 1.0$ , the deep case). Both the number of nodes (Table 4.5) and the distance between the nodes (e.g., the  $y^+$ , see Table 4.6) has a ratio as close as possible to 1.6. No wall functions are used, and even the coarsest grid has a  $y^+$  less than 1.

Table 4.5: Number of nodes in x and y directions for two Reynolds numbers in Case 1 ( $D/L = 1.0$ )

$\lg(Re)$		G1	G2	G3	G4
All	$N_x$	755	471	295	183
6.4	$N_y$	269	169	105	65
9.2	$N_z$	377	237	149	93

In this grid refinement study, a turbulence intensity of 3% and a turbulent viscosity ratio of 12 are used. Two Reynolds numbers ( $Re = 2.51 \times 10^6$  and  $Re = 1.58 \times 10^9$ ) are selected for the verification with three turbulence models, as shown in Figure 4.7.

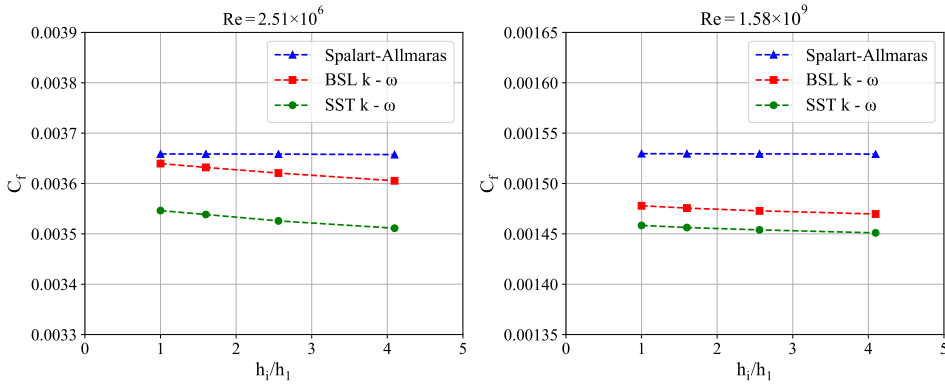
The scale of different grids can be represented by a symbol  $h_i$ , which is defined as follows:

$$\frac{h_i}{h_1} = 1.6^i = \frac{N_{x1}}{N_{xi}} = \frac{N_{y1}}{N_{yi}}, \quad (4.2)$$

where  $h_i$  is a symbol representing the scale of Grid  $i$ ;  $N_{xi}$  and  $N_{yi}$  are the numbers of Grid  $i$  at x and y directions, respectively. The value of  $h_1$  is set

Table 4.6: Values of  $y^+$  of the first layer of the grid above the plate

No.	$\lg(Re)$	G1	G2	G3	G4
1	5.6	0.200	0.320	0.512	0.820
2	6.0	0.200	0.319	0.511	0.817
3	6.4	0.200	0.320	0.512	0.820
4	6.8	0.202	0.323	0.517	0.828
5	7.2	0.205	0.328	0.525	0.840
6	7.6	0.207	0.331	0.530	0.848
7	8.0	0.212	0.339	0.542	0.867
8	8.4	0.212	0.340	0.544	0.870
9	8.8	0.214	0.342	0.547	0.876
10	9.2	0.211	0.337	0.540	0.863

Figure 4.7: Frictional resistance coefficient  $C_f$  with the refinement of grids

to 1 by default. The value of  $h_i$  is useful for presenting the results of grid refinement study (i.e., the x-axis of Figure 4.7).

Although this study applied the 3-equation  $k-k\ell-\omega$  model for  $Re = 2.51 \times 10^6$ , the results showed oscillatory convergence (Table 4.7).

A symbol  $R$ , which can be used to evaluate the oscillation, is defined as

$$R = \frac{C_{fi} - C_{fi+1}}{C_{fi+1} - C_{fi+2}}, \quad (4.3)$$

where  $C_{fi}$  is the frictional resistance coefficient of Grid  $i$  ( $i \leq 2$ ). For  $R < 0$  and  $C_f$  has an oscillatory convergence (Eça and Hoekstra, 2014). Therefore, computations with the  $k-k\ell-\omega$  show oscillatory convergence. Since only the monotonous convergence is considered, the calculations with the  $k-k\ell-\omega$  model was excluded in the systematic calculations.

Following the procedure of numerical uncertainty analysis proposed by

Table 4.7: Grid refinement study with k-kl- $\omega$  model for  $Re = 2.51 \times 10^6$ 

Grid	$C_f \times 10^3$	$R$
G1	15.166	-0.830
G2	15.602	-0.676
G3	15.077	-
G4	15.854	-

Eça and Hoekstra (Eça and Hoekstra, 2014), the uncertainty of  $C_f$  for the finest grid (G1) and the corresponding observed order of accuracy  $p$  is shown in Table 4.8.

Table 4.8: The observed order of accuracy and uncertainty of  $C_f$  for the finest grid (G1)

Turbulence model	$Re = 2.51 \times 10^6$		$Re = 1.58 \times 10^9$	
	$p$	Uncertainty	$p$	Uncertainty
SA	2.49	0.042%	1.00	0.047%
BSL k- $\omega$	0.57	0.919%	0.71	0.376%
SST k- $\omega$	0.61	0.867%	0.74	0.326%

Based on Figure 4.7 and Table 4.8, it can be observed

- In the grid refinement study, the value of  $C_f$  depends on Reynolds number and the selected turbulence models.  $C_f$  increases with the refinement of the mesh. Calculations with SA model generate the highest  $C_f$  and SST k- $\omega$  leads to the lowest  $C_f$  for both Reynolds numbers;
- The chosen turbulence models affect  $C_f$  more than the grid density. Those changes of  $C_f$  become smaller with the mesh refinement;
- Calculations at  $Re = 1.58 \times 10^9$  show smaller uncertainty than those at  $Re = 2.51 \times 10^6$ , but both of the uncertainties are smaller than 1%.

Consequently, the finest grid (Grid 1), which has been verified in this section, is chosen for the further systematic simulations.

### 4.3.2. Validation

After estimating the numerical uncertainty, the deviations of simulations from experimental data (modeling error) are estimated.

In this section, the results of the total friction coefficient ( $C_f$ ) on the flat plate are validated using the friction lines proposed by Schlichting (1941) and Katsui et al. (2005). Different inlet boundary conditions listed in Table 4.3 are compared and the most suitable one will be selected by Table 4.9. Finally, the local skin friction and the mean flow velocity profile, are validated with the experimental data of Nagib et al. (2007).

Formulas of Prandtl-Schlichting and Katsui friction lines are as follows:

1) The Prandtl-Schlichting line (Schlichting, 1941):

$$C_f = \frac{0.455}{(\lg Re)^{2.58}}. \quad (4.4)$$

2) The friction line proposed by Katsui et al. (2005):

$$C_f = \frac{0.0066577}{(\lg Re - 4.3762)^a}, \quad (4.5)$$

for  $1 \times 10^6 \leq Re \leq 7 \times 10^9$ , where  $a = 0.042612 \lg Re + 0.56725$ .

For both  $Re = 2.51 \times 10^6$  and  $Re = 1.58 \times 10^9$ , the differences of  $C_f$  in unrestricted condition ( $D/L=1.0$ ) are compared with these two friction lines, which are shown in Table 4.9.

From Table 4.9, it can be derived that

- The simulations with the SA model overestimate  $C_f$  by 1% - 4% for  $\mu_t/\mu = 100$  at  $Re = 2.51 \times 10^6$  and for all cases at  $Re = 1.58 \times 10^9$ ;
- Simulations with the BSL  $k-\omega$  and the SST  $k-\omega$  models agree with the two friction lines; and the results with BSL  $k-\omega$  model agree better (less than 0.5%), especially when  $I = 6\%$  and  $\mu_t/\mu = 100$ ;
- The results with the  $k-k\ell-\omega$  model show smaller values because this model catches larger laminar regions than fully turbulence models.

For full-scale ships, the turbulent boundary layer starts immediately after the flow reaches the bow and stays along the ship hull. Therefore, the boundary layer computed with the  $k-k\ell-\omega$  model, where a large area of laminar flow is observed, is less comparable with the practice.

According to Table 4.9, the BSL  $k-\omega$  model with  $I = 6\%$  and  $\mu_t/\mu = 100$  has a good agreement with the fully turbulent friction lines at both low and high Reynolds numbers. This set of turbulence model and boundary conditions, therefore, are chosen for further systematic simulations.

Additionally, Nagib et al. (2007) evaluated many previously proposed empirical local friction formulas based on more recent experimental datasets (Nagib et al., 2006; Österlund, 1999). Through proper modifications, they concluded that those formulas could accurately describe the local friction. The mean velocity profiles in the turbulent boundary layers were also shown in a graph against a large range of momentum thickness Reynolds number ( $Re_\theta$ ), which provides additional validating data for this research.

Table 4.9: Differences of  $C_f$  compared with methods of Prandtl-Schlichting and Katsui et al. at both  $Re = 2.51 \times 10^6$  and  $Re = 1.58 \times 10^9$  (shown in percent, %)

Turbulence model	I (%)	Compared with Prandtl-Schlichting method						Compared with Katsui method					
		$Re = 2.51 \times 10^6$			$Re = 1.58 \times 10^9$			$Re = 2.51 \times 10^6$			$Re = 1.58 \times 10^9$		
		9	12	100	9	12	100	9	12	100	9	12	100
SA	-	-3.70	-3.34	1.11	3.07	3.07	3.10	-1.02	-0.65	3.92	3.95	3.95	3.97
	0.9	-3.89	-3.85	-3.48	-0.41	-0.40	-0.33	-1.21	-1.17	-0.80	0.43	0.44	0.52
	3	-3.89	-3.84	-2.78	-0.42	-0.41	-0.36	-1.22	-1.17	-0.08	0.43	0.43	0.48
BSL k- $\omega$	6	-3.91	-3.86	-2.70	-0.42	-0.42	-0.38	-1.24	-1.19	0.00	0.43	0.43	0.47
	0.9	-6.34	-6.32	-6.13	-1.72	-1.71	-1.64	-3.74	-3.71	-3.52	-0.88	-0.88	-0.80
	3	-6.34	-6.31	-5.63	-1.73	-1.73	-1.67	-3.74	-3.70	-3.01	-0.89	-0.89	-0.83
SST k- $\omega$	6	-6.35	-6.32	-5.57	-1.74	-1.73	-1.69	-3.75	-3.72	-2.94	-0.90	-0.89	-0.85
	0.9	-59.91	-60.05	-65.20	-	-	-	-58.80	-58.94	-64.23	-	-	-
	3	-59.84	-59.93	-24.71	-	-	-	-58.72	-58.82	-22.61	-	-	-
k-kl- $\omega$	6	-59.90	-59.87	-22.69	-	-	-	-58.79	-58.75	-20.54	-	-	-

Based on the fitting of Nagib, the local Reynolds number ( $Re_x$ ) can be converted to  $Re_\theta$  using

$$Re_\theta = 0.01277(Re_x)^{0.8659} \quad (4.6)$$

The CFD calculations of local friction coefficients ( $C_{fx}$ ) are validated in Figure 4.8. A curve fitted by Schlichting (1979) ( $C_{fx} = [2 \lg(Re_x) - 0.65]^{-2.3}$ ) is also shown for comparison

When compared with the results of Nagib, the CFD calculations have up to 6% errors. If the classical local friction line, i.e., Prandtl-Schlichting, is used, the CFD results generally underestimate  $C_{fx}$  by about 4%. The data of Nagib is based on more recent experiments, which are assumed to be more reliable. It should be pointed out that, after converting  $Re_\theta$  to  $Re_x$ , the error of  $C_{fx}$  becomes less than 1%, which is practically acceptable.

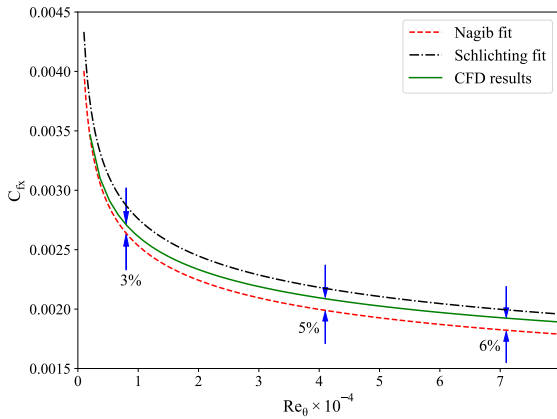


Figure 4.8: The local friction coefficient is shown against  $Re_\theta$  (the friction line of Prandtl-Schlichting is shown for comparison)

The mean velocity profiles are also validated using the data of Nagib, which are shown in Figure 4.9. The CFD results agree well with the experiments, especially for  $y^+ < 8$  and  $50 < y^+ < 500$ . In other regions, CFD results slightly underestimate the velocity profile, which means a thinner boundary layer and thus a higher velocity gradient. This leads to a small overestimate of  $C_{fx}$ , which is shown in Figure 4.8.

Based on the validation, CFD techniques applied in this study have acceptable errors and are reliable for further calculations.

## 4.4. Results and Analysis

The systematic simulations involve ten Reynolds numbers and seven shallow water conditions, as shown in Table 4.10. The number of grid cells in the x-direction ( $N_x$ ) is unchanged from  $Re = 3.9811 \times 10^5$  to  $Re = 2.5119 \times 10^8$ ,

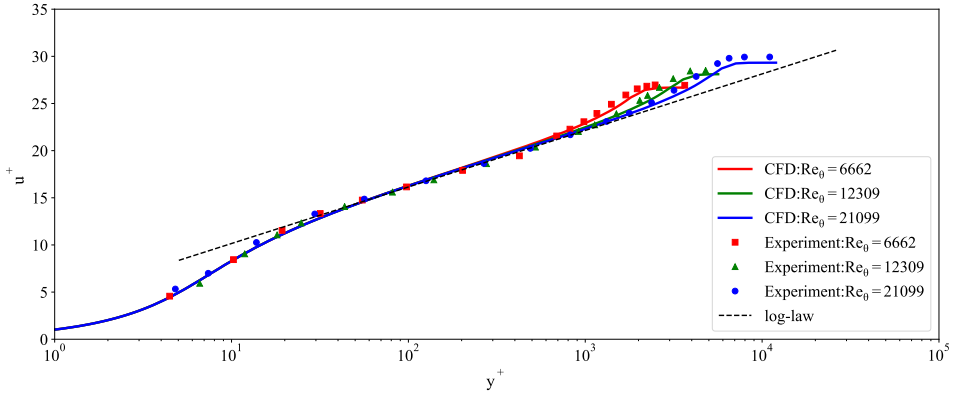


Figure 4.9: Mean velocity profiles and log-law diagnostic function against  $y^+$  ( $u^+$  is the dimensionless velocity defined by  $u^+ = u/\sqrt{\tau_w/\rho}$ , where  $u$  is the flow velocity parallel to the plate and  $\tau_w$  is the wall shear stress; in the logarithmic law,  $\kappa = 0.394$ )

and to stabilize the calculation,  $N_x$  is increased to 827 (finer mesh) at higher Reynolds numbers. The number of grid cells in the  $y$ -direction ( $N_y$ ) varies based on the distance between the flat plate and the parallel wall.

Table 4.10: Number of nodes in  $x$  and  $y$  directions at different conditions

No.	$Re$	$\lg(Re)$	$N_x$	$N_y$						
				$D/L$						
				1.00	0.32	0.16	0.08	0.04	0.02	0.01
1	$3.9811 \times 10^5$	5.6	755	237	165	113	85	65	45	29
2	$1.0000 \times 10^6$	6.0	755	253	177	125	97	77	57	41
3	$2.5119 \times 10^6$	6.4	755	269	189	137	109	89	69	53
4	$6.3096 \times 10^6$	6.8	755	285	201	149	121	101	81	65
5	$1.5849 \times 10^7$	7.2	755	301	213	161	133	117	93	77
6	$3.9811 \times 10^7$	7.6	755	313	225	173	145	129	105	89
7	$1.0000 \times 10^8$	8.0	755	329	237	185	157	141	117	101
8	$2.5119 \times 10^8$	8.4	755	345	249	197	169	153	129	113
9	$6.3096 \times 10^8$	8.8	827	361	265	209	181	165	141	125
10	$1.5849 \times 10^9$	9.2	827	377	277	221	193	177	153	137

#### 4.4.1. Physics of Shallow Water Effects on Friction

Physically, the flow will be accelerated due to the displacement of the boundary layer, leading to a thinner boundary layer, especially in extremely shallow water conditions. To illustrate the changes in boundary layers, a square area close to the flat plate is chosen, as shown in Figure 4.10.

The boundary layer thicknesses at the trailing edge of the plate at two Reynolds numbers are shown in Figure 4.11. The space in the  $y$ -direction



Figure 4.10: The area in the dashed box is chosen for illustrating the shallow water effect on boundary layer thickness

is amplified 5 times to illustrate the physical details in the boundary layer clearly.

From Figure 4.11, some remarks can be derived:

- The maximum flow speed increases for both  $Re = 2.51 \times 10^6$  and  $Re = 1.58 \times 10^9$ . The boundary layer thickness decreases with the decrease of  $D/L$ ;
- When  $D/L = 0.01$ , where the distance between the flat plate and the parallel wall has the same order of magnitude as the boundary layer thickness, the boundary layer thickness decreases more significantly than that for  $D/L \geq 0.02$ .

As a consequence, the velocity gradient normal to the flat plate increases, leading to a rise of the local friction ( $C_{fx}$ ). Figure 4.12 shows the results of  $C_{fx}$  at  $Re = 2.51 \times 10^6$  and  $Re = 1.58 \times 10^9$  in different shallow water conditions.

Several remarks can be drawn from Figure 4.12:

- For both Reynolds numbers, limited water depth has an increasing influence on  $C_{fx}$  from the leading edge to the trailing edge;
- $C_{fx}$  increases rapidly with the decrease of  $D/L$ ;
- The influence of shallow water on local friction is more significant at the low Reynolds number. For example, at the trailing edge, when  $D/L = 0.01$ , the increase of  $C_{fx}$  can be more than 50% at  $Re = 2.51 \times 10^6$  but is only 20% at  $Re = 1.58 \times 10^9$ . This discrepancy shows significant scale effects when extrapolating resistance in shallow water from model scale to full scale.

Consequently, the total frictional resistance, which is the sum of the local frictions, also increases in shallow water conditions and depends on  $D/L$  as well.

#### 4.4.2. The Validity of Zero-pressure Gradient Assumption

An assumption in the previous research (Eça and Hoekstra, 2008; Grigson, 1999; ITTC, 1957; Katsui et al., 2005; Schoenherr, 1932; Todd, 1951) about the flow passing over a flat plate is that the pressure gradient along the plate is zero. Based on this assumption, it is convenient to derive both analytical

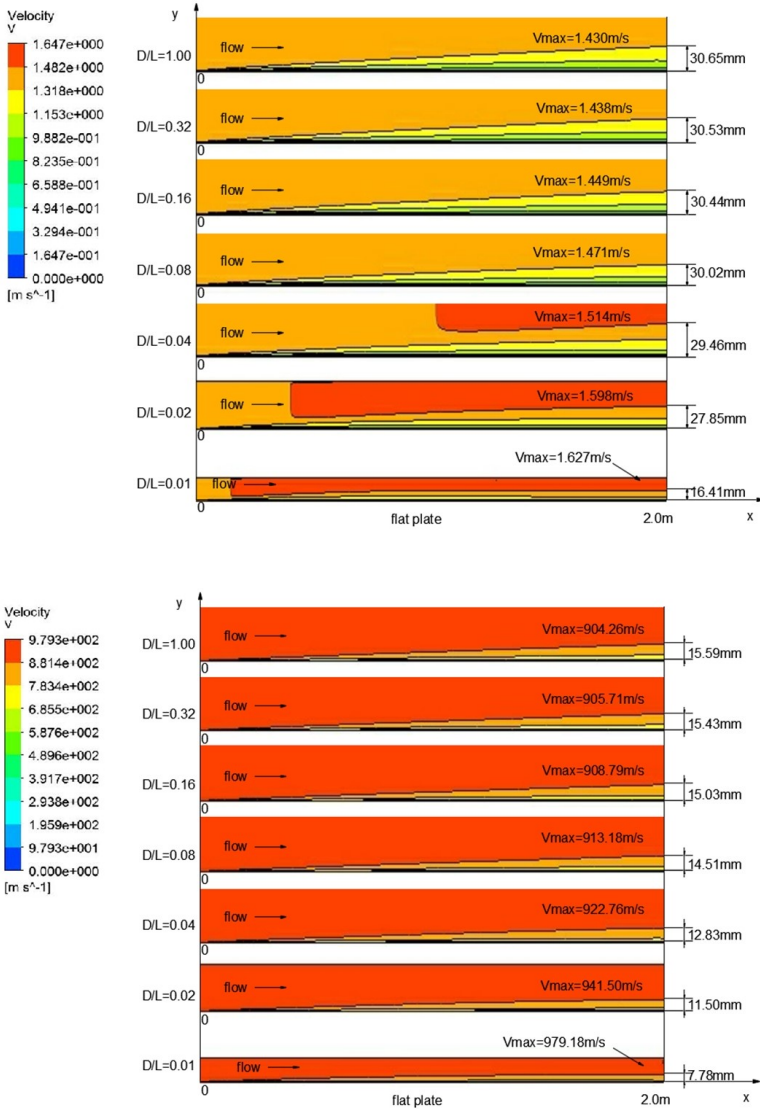


Figure 4.11: The velocity contour close to the flat plate at different  $D/L$  (top:  $Re = 2.51 \times 10^6$ , bottom:  $Re = 1.58 \times 10^9$ ; the boundary layer thickness ( $0.99V_{max}$ ) at  $x = 2\text{ m}$  is shown at the right of the figures)

and practical solutions for friction lines which have a good agreement with experimental data in unrestricted water.

For incompressible, two-dimensional laminar flow, the control equations within the boundary layer are

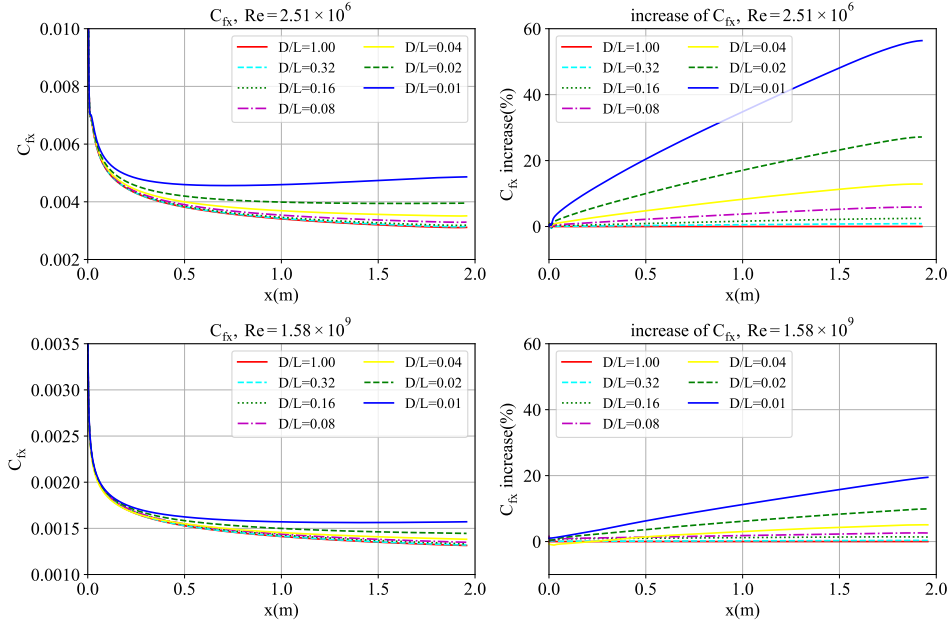


Figure 4.12: Local friction resistance coefficient ( $C_{fx}$ ) and  $C_{fx}$  increase compared to  $D/L = 1.00$  (in percent) at in shallow water conditions

$$u \frac{\partial u}{\partial x} + v \frac{\partial u}{\partial y} = -\frac{1}{\rho} \frac{\partial p}{\partial x} + \frac{\partial^2 u}{\partial y^2}, \quad (4.7)$$

$$0 = -\frac{\partial p}{\partial y}, \quad (4.8)$$

$$\frac{\partial u}{\partial x} + \frac{\partial v}{\partial y} = 0. \quad (4.9)$$

Blasius (1908) (translated by NACA (1950)) set the term to zero in equation (4.7) and derived the Blasius solution.

For a two-dimensional, fully-developed turbulent flow, based on the Zero-pressure Gradient (ZPG) assumption and a large amount of experiments results, Schlichting (1941) fitted a formula for  $C_f$  in fully turbulent flow:

$$C_f = \frac{0.455}{(\lg Re_x)^{2.58}} \quad (4.10)$$

However, the validity of the ZPG in shallow water should be tested. In this study, two Reynolds numbers are used:  $Re = 2.51 \times 10^6$  and  $Re = 1.58 \times 10^9$ . Sample points are selected on three straight lines which close

to the boundary layer, with the same length of the flat plate and offset the plate by  $d = 5$  mm, 10 mm, and 15 mm, as shown in Figure 4.13. Values of pressure gradient and velocity gradient were recorded at these points.

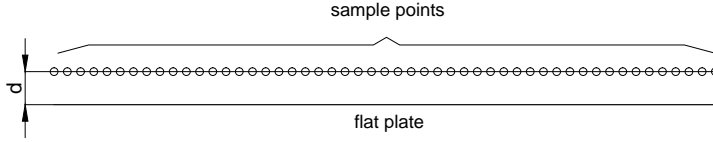


Figure 4.13: Sample points near the flat plate

4

To evaluate the ZPG assumption, the essence of the problem is to compare the order of magnitude of  $u\partial u/\partial x$  and  $-\rho^{-1} \cdot \partial p/\partial x$ . The ZPG assumption is not valid if these two terms have the same order. Figure 4.14 presents the values of  $u\partial u/\partial x$  and  $-\rho^{-1} \cdot \partial p/\partial x$  in different conditions.

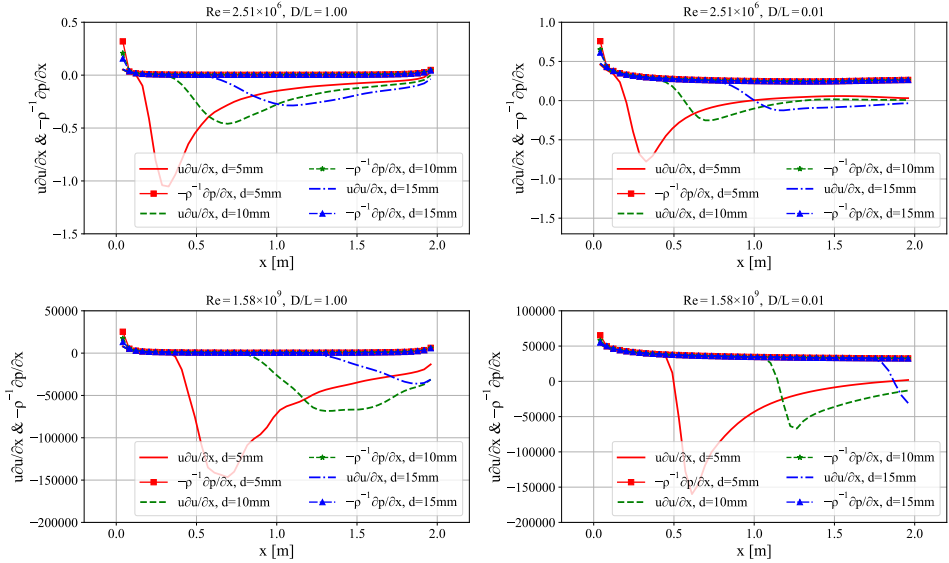


Figure 4.14: Magnitude comparisons of  $u\partial u/\partial x$  and  $-\rho^{-1} \cdot \partial p/\partial x$  at four conditions (Case information is shown at the top of each sub-graph. The y axis denotes the magnitudes of  $u\partial u/\partial x$  and  $-\rho^{-1} \cdot \partial p/\partial x$ . The x axis shows the position from the leading edge to trailing edge of the flat plate)

When  $D/L$  is 1.00, values of  $-\rho^{-1} \cdot \partial p/\partial x$  are close to zero, which are negligible compared to  $u\partial u/\partial x$  for both Reynolds numbers. However, when  $D/L$  drops to 0.01, the magnitude of  $-\rho^{-1} \cdot \partial p/\partial x$  increases significantly and reaches the same order as  $u\partial u/\partial x$ .

Therefore, when  $D/L$  is small enough, the item  $-\rho^{-1} \cdot \partial p/\partial x$  is no longer

negligible, both at low and high Reynolds numbers. In other words, the ZPG assumption is invalid at  $D/L = 0.01$ . Thus, those methods based on the zero-pressure gradient assumption should be reconsidered in shallow water cases.

#### 4.4.3. Shallow Water Effects on Frictional Resistance

Results of the total frictional resistance coefficients of the flat plate and their increase compared with deep water condition (in percent) are presented in Figure 4.15.

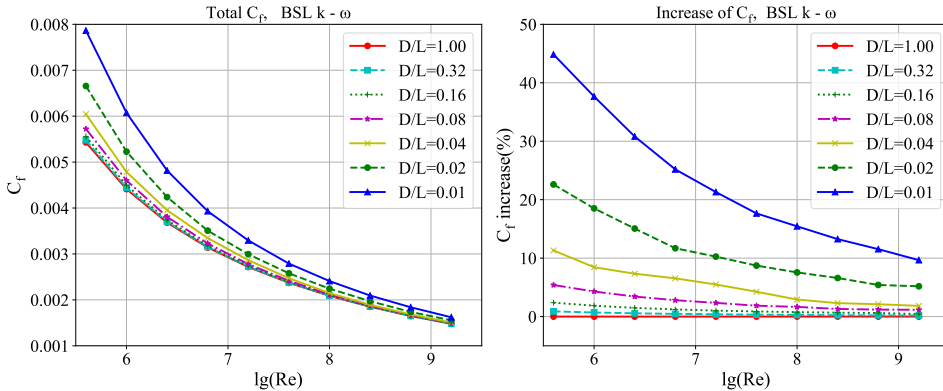


Figure 4.15: Total frictional resistance coefficient ( $C_f$ ) with Reynolds number (left); Increase of  $C_f$  compared with  $D/L = 1.00$  (right)

Based on Figure 4.15, it can be derived that

- For relatively low Reynolds numbers ( $\lg(Re) < 7.5$ ),  $D/L$  significantly influences  $C_f$ . For instance, when  $\lg(Re) = 5.6$ , the increase of  $C_f$  can reach almost 50% compared to the deep water condition;
- The influences from shallow water are diminishing with the increase of Reynolds number. For instance, when  $\lg(Re) = 9.2$ , the increase of  $C_f$  is only 10% compared to the deep water condition.

As a result, the influence of shallow water conditions on  $C_f$  again depends on the Reynolds number. Shallow water effects are larger at lower  $Re$  since the boundary layer is thicker and is easier to be affected by limited space.

In practice, the scale effects at shallow water conditions may cause large errors in engineering. For instance, for an inland ship with 100 meters long and sails at 18 km/h (relative to the flow under the ship bottom), its Reynolds number is about  $4.4 \times 10^8$ , and it sails in shallow water with  $D/L = 0.01$ . When using a 1/25 scaled model, which has a Reynolds number about  $3.5 \times 10^6$ , to extrapolate the total resistance,  $C_f$  of the bottom part

at full scale will increase by about 11% compared to deep water, but it will increase by about 28% at model scale according to this study. This discrepancy will lead to an unreliable resistance extrapolation if the ITTC57 correlation line is applied. Consequently, the ITTC57 line should be modified by considering shallow water effects to contribute a more reliable prediction of ship's frictional resistance in shallow water.

#### 4.4.4. The Fitting of a Numerical Friction Line

This section proposes a numerical friction line for correcting the shallow water effects on ship's bottom based on the described CFD calculations.

A regression analysis using the method of least squares was applied. During the procedure, choosing a suitable function model is essential to the quality of the fitting. Inspired by the ITTC (1957) formula, the function model as follows was applied:

$$C_f = \frac{a}{(\lg Re - b)^c}, \quad (4.11)$$

$a$ ,  $b$  and  $c$  are constants defined in the fitting. In this study, this regression follows two steps: first, fit a numerical friction line in deep water condition using the results of  $D/L = 1.00$ ; Second, include the parameter  $D/L$  based on the numerical results of all cases of  $D/L$ .

The result for the first fitting with the R-squared value (a statistical measure of how close the data are to the fitted regression line) of 0.9996 is shown as follows:

$$C_{f\_deep} = \frac{0.08169}{(\lg Re - 1.717)^2}. \quad (4.12)$$

$C_f$  in shallow water conditions depends on Reynolds number and  $D/L$ . Additionally, equation (4.12) is an intermediate step that is used to provide information for the fitting of all  $D/L$ . The value of  $R^2$  can be changed when a new fitting is performed.

Afterward, a numerical friction line in all shallow conditions is proposed using regression analysis:

$$C_{f\_proposed} = \frac{0.08169}{(\lg Re - 1.717)^2} \cdot \left(1 + \frac{0.003998}{\lg Re - 4.393} \cdot \left(\frac{D}{L}\right)^{-1.083}\right), \quad (4.13)$$

$Re$ : Reynolds number;  $D$ : the distance between flat plate and parallel wall;  $L$ : the length of the flat plate.

Equation (4.13) is based on all cases of  $D/L$ . It has a slight deviation (less than 0.33%) from equation (4.12) at  $D/L = 1.0$ , and the new  $R^2$  is 0.9998. Errors between the CFD results and equation (4.13) are shown in Table 4.11.

Table 4.11: Errors between simulations and the proposed friction line

$Re$	$D/L$						
	1.00	0.32	0.16	0.08	0.04	0.02	0.01
$3.9811 \times 10^5$	0.11%	0.03%	-0.18%	-0.50%	-0.66%	0.04%	2.33%
$1.0000 \times 10^6$	1.19%	1.10%	0.89%	0.51%	0.64%	-0.16%	0.07%
$2.5119 \times 10^6$	1.35%	1.28%	1.11%	0.81%	0.37%	0.03%	-0.10%
$6.3096 \times 10^6$	0.85%	0.79%	0.67%	0.45%	-0.37%	0.50%	0.01%
$1.5849 \times 10^7$	0.20%	0.16%	0.08%	-0.08%	-0.73%	-0.30%	-0.30%
$3.9811 \times 10^7$	-0.35%	-0.38%	-0.45%	-0.42%	-0.65%	-0.57%	0.05%
$1.0000 \times 10^8$	-0.74%	-0.75%	-0.80%	-0.80%	-0.17%	-0.74%	-0.16%
$2.5119 \times 10^8$	-1.00%	-1.00%	-1.04%	-0.87%	-0.17%	-0.82%	0.10%
$6.3096 \times 10^8$	-1.16%	-1.15%	-1.19%	-1.04%	-0.42%	-0.43%	0.31%
$1.5849 \times 10^9$	-1.24%	-1.23%	-1.16%	-1.20%	-0.46%	-0.78%	0.96%

The errors are mostly less than 1%, except when  $D/L = 0.01$  (still less than 3%). This error table can be referred to when using this new friction line.

#### 4.4.5. Application and a Case Study

The previous section proposed a modification of the ITTC57 correlation line. However, since a ship also has non-horizontal wetted surfaces, this method cannot be applied directly. In this paper, it is suggested to apply the ITTC57 correlation line for all wetted surface and modify the frictional resistance on the flat bottom area with the proposed friction line. The following steps are proposed to following this method in the prediction of the frictional resistance of an actual ship:

- Use the ship's physical or digital model to obtain the area of the total wetted surface ( $S_T$ ) and the area of the flat bottom ( $S_B$ );
- Calculate the Reynolds number ( $Re_0$ ) of the incoming flow with the free stream velocity ( $V_0$ );
- Calculate the Reynolds number ( $Re_B$ ) of the water underneath the ship's bottom with the incoming velocity ( $V_B$ ) derived from continuity equation or potential flow calculations by averaging the velocity at the leading edge of the flat bottom;
- Apply the ITTC57 correlation line to calculate the conventional frictional resistance coefficient  $C_{f0}$ ;
- Use the proposed friction line to calculate the coefficient ( $C_{f-proposed}$ ) in shallow water, and use the Katsui's line to calculate the friction coefficient ( $C_{f-Katsui}$ ) of flat plate in unrestricted conditions;
- The corrected total frictional resistance coefficient ( $C_f$ ) of ship in shallow water can be predicted as

$$C_f = C_{f0} + (C_{f-proposed} - C_{f-Katsui}) \cdot \left(\frac{S_B}{S_T}\right) \cdot \left(\frac{V_B}{V_0}\right)^2 \quad (4.14)$$

It should be pointed out that the Katsui's line used in equation (4.14) can be replaced by any other suitable deep water friction line.

As a case study, the above steps are applied for a 1/30 scaled model ship, whose prototype is an 86-meter long inland ship. The free surface is not considered in CFD calculations to eliminate wave effects on friction. Details of the ship parameters can be found in Chapter 3.

To achieve the average velocity ( $V_B$ ) at the leading edge of the wide flat bottom (as indicated in Figure 4.3), a systematic CFD calculation has been done for various incoming velocities and water depths. The results of  $V_B$  are shown in Figure 4.16, and an empirical formula is regressed for this specific case. For  $h/T > 4.0$ ,  $V_B \approx V$ . For  $h/T \leq 4.0$ ,

$$V_B \equiv V + \Delta V = 0.4277 \cdot V \cdot \exp\left\{\left(\frac{h}{T}\right)^{-0.07634}\right\}. \quad (4.15)$$

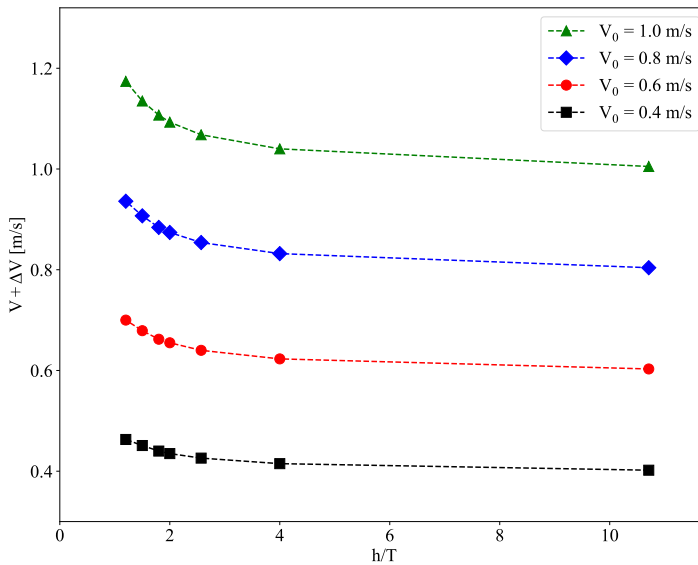


Figure 4.16: The average velocity at the leading edge of the flat bottom against water depth

Following the steps shown at the beginning of this section, the frictional resistance of this ship model is predicted at 0.8 m/s and 1.0 m/s in various water depths, as shown in Table 4.12.

For all the three different water depths, results of  $C_f$  using the proposed method agree better with the values derived from CFD compared to the

Table 4.12: An example of applying the proposed friction line

$V_0$ (m/s)	$V_B$ (m/s)	$h/T$	$D/L$	$C_f$ from CFD ( $\times 10^{-3}$ )	ITTC57		Proposed method	
					$C_f$ ( $\times 10^{-3}$ )	Error	$C_f$ ( $\times 10^{-3}$ )	Error
0.8	0.800	10.71	0.3952	3.886	4.049	4.19%	4.049	4.19%
	0.882	2.01	0.0411	4.187	4.049	-3.29%	4.133	-1.28%
	0.916	1.20	0.0081	4.555	4.049	-11.11%	4.540	-0.33%
1	1.000	10.71	0.3952	3.760	3.872	3.00%	3.872	3.00%
	1.102	2.01	0.0411	4.058	3.872	-4.58%	3.961	-2.40%
	1.145	1.20	0.0081	4.421	3.872	-12.41%	4.390	-0.69%

ITTC57 line. With the differences less than 3% in shallow water, the improved correlation line is practically considered applicable to successfully predict the friction including shallow water effects on ship's flat bottom.

## 4.5. Concluding Remarks

In this chapter, a numerical friction line has proposed for correcting shallow water effects on ship's bottom using CFD calculations.

A moving plate approaching a flat plate is applied to build the shallow water conditions. Three fully turbulence models (Spalart-Allmaras, BSL  $k-\omega$ , and SST  $k-\omega$ ) and one transition model ( $k-kl-\omega$ ) are applied to verify and validate the numerical calculations. Practically, the BSL  $k-\omega$  is the most suitable model, and the turbulence intensity of 6% with the turbulent viscosity ratio of 100 is the best inlet boundary condition in this study.

Based on the calculations in shallow water conditions, it can be concluded that

- For low Reynolds numbers,  $D/L$  significantly influences the friction on the flat plate. When  $\lg(Re) = 5.6$ , the increase of  $C_f$  can reach almost 50% compared to the deep water condition;
- The influence of shallow water on friction has scale effects, which diminishes with the increase of Reynolds number. For a relatively high Reynolds number (e.g.  $\lg(Re) = 9.2$ ), the increase of  $C_f$  is only 10% compared to the deep water condition;
- The zero-pressure gradient assumption should be reconsidered in shallow water.

Reynolds number is no longer the only factor influencing the friction at shallow water conditions. It was shown in the case study at the end of this chapter that the conventional method with the ITTC57 correlation line would underestimate the total frictional resistance of a ship by more than 12%. A numerical friction line considering the shallow water effects and the scale effects is proposed. After applying this proposed line to modify the frictional resistance on ship's bottom and applying the ITTC57 correlation

line for the remaining wetted surface, the difference of the prediction of ship's frictional resistance is reduced to less than 3% in shallow water.

For resistance extrapolation in shallow water from ship models to full-scale ships, the proposed friction line can also correct the scale effect on the frictional resistance of on ship's bottom and thus, increase the reliability of the model-ship extrapolation of resistance.

Simplifying the flow under ship's bottom into a 2D case can be a good approximation of the prediction of ship's frictional resistance in shallow water. This method is practically acceptable but if one wants to gain more in-depth insight into the ship flow in shallow water, straightforward computations of 3D hull forms are required. This will be the main concern of the next chapter.

# 5

## Shallow Water Effects on the Viscous Resistance of Ships

In the previous chapter, shallow water effects on the frictional resistance on a 2D flat plate were discussed, and a modification for the ITTC57 correlation line was proposed. This modification can be applied to improve the prediction of the frictional resistance on ship's flat bottom in shallow water but cannot be applied directly for a 3D curved surface. Likewise, the other known friction lines have the similar drawbacks when dealing with a 3D surface. In this chapter, shallow water effects on the frictional resistance of 3D ship hulls will be investigated. As the wave-making resistance is a minor part for cargo ships sailing in shallow water (typically at low speed), the free surface is suppressed in the computations. Additionally, results of the viscous pressure resistance, which can be represented by a so-called form factor, are obtained after the simulations. How the form factor changes in shallow water will also be discussed in this chapter.

A Wigley hull and the KCS (KRISO Container Ship), for which benchmark data are available, are used. An 86 m long inland ship is added to analyze a typical inland vessel and also discuss the influence of the transom. Based on the results, a formula to predict a ship's friction in shallow water is proposed with some constants determined based on ship's characteristics. A form factor defined based on ship's computed frictional resistance is suggested, and an empirical expression is provided for each ship mentioned.

---

This chapter is based on the papers:

Zeng, Q., Hekkenberg, R., Thill, C.(2019). On the viscous resistance of ships sailing in shallow water. *Ocean Engineering*, 190, 106434. (Zeng et al., 2019a)

Zeng, Q., Hekkenberg, R., Thill, C.(2019). A study of ship's frictional resistance in extremely shallow water, 38th International Conference on Ocean, Offshore & Arctic Engineering (OMAE 2019), Glasgow, UK. (Zeng et al., 2019b)

## 5.1. Introduction

The conventional way to deal with ship resistance during ship model tests is based on Froude's approach, where the resistance is divided into two independent parts, the viscous resistance component and the wave resistance component. The viscous part,  $(1+k)C_f$ , is assumed to be proportional to the frictional resistance coefficient  $C_f$ , where  $1+k$  is the so-called form factor (Hughes, 1954). In the model-ship extrapolation of resistance, the factor  $1+k$  is assumed to be independent of the Reynolds number ( $Re$ ), but in reality, it varies with both the ship's size (García-Gómez, 2000) and the applied friction line (Van der Ploeg et al., 2008).

In the previous chapter, the velocity field and pressure field of the flow close to a restricted flat plate are studied. The accuracy of the prediction of  $C_f$  proposed in Chapter 4 will be affected by the absence of 3D flow effects. In this chapter, the role of the water depth and the hull form to the changes of  $C_f$  in shallow water will be analyzed and discussed.

For  $1+k$ , in addition to the ship's size and the applied friction line, it was found that it also depends on water depth. Based on model tests, Millward (1989) suggested an empirical correction for  $1+k$  in different water depths. The CFD simulations performed by Toxopeus (2011) supported Millward's formula and indicated that the factor  $1+k$  of the KVLCC2 could increase by about 30% in shallow water. Raven (2012) showed that the treatment of the form factor is crucial for the accuracy of the extrapolation of ship resistance from model to full scale, and proposed an empirical correction four years later Raven (2016). However, a systematic study of  $1+k$  considering the effects of both the Reynolds number and the water depth is missing, which is regarded as the second concern in this chapter apart from the frictional resistance.

Additionally, an immersed transom is a crucial factor that affects the form factor (Hollenbach, 2009). Large transoms, as well as tunnel endings, are commonly found on inland ships, and their effects on ship resistance are difficult to separate from the total resistance. In this chapter, an 86 m inland ship with a transom is added, and the influence of the transom is incorporated in  $1+k$ .

Furthermore, double-body calculations are performed using Computational Fluid Dynamics (CFD). By suppressing the free surface, the method allows the study of form effects even at higher speeds as long as the form effects due to the deformed free surface can be excluded. Seven shallow water conditions are generated by adjusting the position of the water bottom. A deep-water case is added for comparison. Twelve Reynolds numbers which vary from  $10^5$  to  $10^9$  are used, which cover the range from model scale to full scale. After comparing the viscous resistance of the ships with the results on a 2D flat plate, the effects of the curved surface of a ship are discussed. The results of the viscous resistance of a Wigley hull, the KCS, and the 86m inland ship provide insight into form effects on both  $C_f$  and  $1+k$  in shallow water.

## 5.2. Method

In this section, a strategy of exploring the effects of water depth on the ship's viscous resistance is introduced, followed with the details of the geometric models and mesh generation.

### 5.2.1. The Strategy of Comparison

Although the empirical friction lines exist, a numerical friction line derived from the simulations on a 2D flat plate is applied for further analysis, by which all comparisons will be made among numerical results.

In the previous chapter, the majority of shallow water effects on the frictional resistance are observed on a ship's flat bottom. Also, the area of the flat bottom highly depends on the fullness of the ship, which can be represented by the block coefficient ( $C_B$ ). Therefore, three ships, the Wigley hull, the KCS, and an 86m inland ship, are selected. The corresponding  $C_B$  values are 0.45, 0.65, and 0.86. The difference between different ship forms helps to reveal the influence of the ship forms or, specifically, the area of the flat bottom on the viscous resistance in shallow water. The strategy of this study is outlined in Figure 5.1.

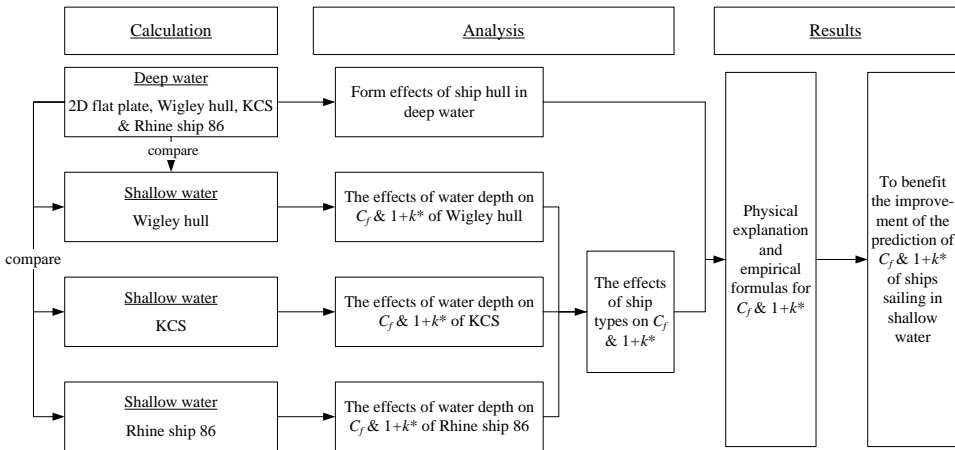


Figure 5.1: The strategy of comparison in this chapter ( $C_f$ : the coefficient of the frictional resistance;  $1 + k$ : the form factor)

The Reynolds number ( $Re$ ) is one of the dimensionless variables controlled in this study. Generally, the  $Re$  for a ship model is at the level of  $10^6$  and a value of  $10^9$  for a full-scale ship. Since the results of resistance at model scale are more sensitive to  $Re$  (Chapter 4), more sampling points are given for the relatively low  $Re$  range, as shown in Table 5.1.

Table 5.1: The chosen Reynolds number ( $Re$ ) in this chapter

No.	$\lg(Re)$	$Re$
1	5.8	$6.310 \times 10^5$
2	6.0	$1.000 \times 10^6$
3	6.2	$1.585 \times 10^6$
4	6.4	$2.512 \times 10^6$
5	6.6	$3.981 \times 10^6$
6	6.8	$6.310 \times 10^6$
7	7.2	$1.585 \times 10^7$
8	7.6	$3.981 \times 10^7$
9	8.0	$1.000 \times 10^8$
10	8.4	$2.512 \times 10^8$
11	8.8	$6.310 \times 10^8$
12	9.2	$1.585 \times 10^9$

### 5.2.2. The Models

In this section, the models of a 2D flat plate, the Wigley hull, the KCS, and the 86m inland ship are introduced.

#### The 2D flat plate

The computational domain of the 2D flat plate and the boundary conditions are shown in Figure 5.2.

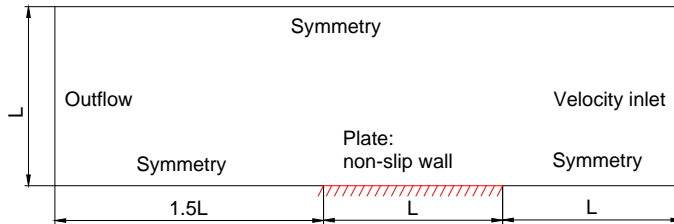


Figure 5.2: The computational domain of for the 2D flat plate and the boundary conditions

The computational domain extends one plate length ( $L$ ) in front of the plate,  $1.5L$  in the rear and  $L$  at the side. As indicated in the approach of the previous chapter, such size of domain is large enough for  $C_f$  calculations.

#### The Wigley hull, the KCS and the Rhine Ship 86

The hull surface of a Wigley hull can be described mathematically as

$$y = \frac{B}{L} \left( 1 - \left( \frac{2x}{L} \right)^2 \right) \left( 1 - \left( \frac{z}{T} \right)^2 \right), \quad (5.1)$$

where  $B$  is the beam,  $L$  the length, and  $x, y, z$  are the coordinates of three directions.  $x$  is positive forward,  $y$  is positive port and  $z$  is positive upward. This coordinate system is also valid for the KCS except for the position of the origin. For the Wigley hull, the origin is the cross point of the midsection, the symmetric plane, and the designed waterline plane. For the KCS, the origin is the cross point of the aft perpendicular and the zero waterline plane.

The sketches of sections of the Wigley hull (Ship A), the KCS (Ship B), and the Rhine Ship 86 (Ship C) are shown in Figure 5.3. Since the total length of the inland ship is 86m and it sails in the Rhine, it was named as “Rhine Ship 86”.

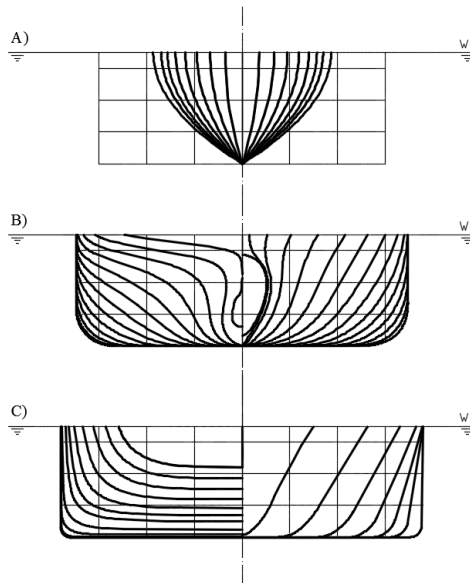


Figure 5.3: The sections of A) the Wigley hull, B) the KCS, and C) the Rhine Ship 86

The main dimensions of the ships are listed in Table 5.2. In the table,  $L_{pp}$  is the length between the perpendiculars,  $B$  the beam,  $C_B$  the block coefficient, and  $S$  the area of the wetted surface.

Table 5.2: The main dimensions of the Wigley ship, the KCS, and the Rhine Ship 86

	Unit	Wigley ship	KCS	Rhine Ship 86
$L_{pp}$	m	2.500	230.000	85.522
$B$	m	0.250	32.200	11.400
$T$	m	0.156	10.800	3.500
$C_B$	-	0.445	0.651	0.860
$S$	m <sup>2</sup>	0.930	9530.000	1418.761

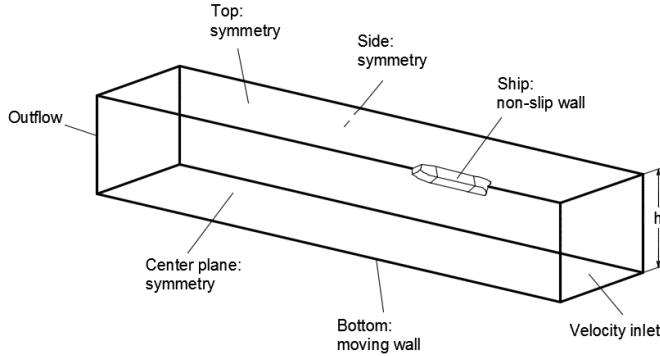


Figure 5.4: The computational model and boundary conditions for the ships ( $h$ : water depth)

## 5

The computational domain is shown in Figure 5.4. Half of the ship is applied due to symmetry. The domain extends  $3L_{pp}$  behind the ship. The side boundary should be set far enough to avoid blockage effects. To search for an appropriate position, calculations were performed for the KCS with the side boundary deviate by  $0.5L_{pp}$ ,  $1.0L_{pp}$ ,  $1.5L_{pp}$ ,  $2.0L_{pp}$ , and  $3.0L_{pp}$  from the ship, and the results are compared in Table 5.3. In addition, one ship length in front of the ship was found far enough to prevent a severe upwind effect of the object to the inlet boundary. Whether a position further than  $1.0L_{pp}$  will affect the result is also studied by setting the inlet boundary at  $1.5L_{pp}$ ,  $2.0L_{pp}$ , and  $3.0L_{pp}$  in front of the object. At the inlet boundary for Cases 1 through 8, the initial turbulent intensity is 6% and the turbulent viscosity ratio ( $\mu_t/\mu$ ) is 100, which follows the validations of Chapter 4. For Case 9, the initial turbulent intensity is 2.6% and the turbulent length scale is  $3L_{pp}$ , by which the level of the turbulent intensity in front of the ship is similar to the benchmark (Case 5). The results of  $C_f$  for all cases are compared in Table 5.3.

Several remarks can be derived based on Table 5.3. For the position of the side boundary (Cases 1 through 5):

- When the side boundary is  $0.5L_{pp}$  away from the ship,  $B_C$  is 11.7% and  $C_f$  is 6.3% higher compared to Case 5, which is considered as significant;
- When the side boundary is  $1.0L_{pp}$  away from the ship, its influence on  $C_f$  is negligible (less than 1%);
- Changing the location of the side boundary in the range of  $0.5L_{pp} - 3.0L_{pp}$  has no influence on the turbulent intensity in front of the vessel;
- If a stricter requirement of accuracy is needed (e.g., less than 0.1%),  $B_C$  should be less than 3.9% (see Case 3);

Table 5.3: Results of the  $C_f$  of the KCS with different locations of the side and front boundary  
(General information:  $h/T = 1.2$ ,  $\lg(Re) = 6.4$ ,  $y^+ = 2$ )

Case	Side ( $\times L_{pp}$ )	Front ( $\times L_{pp}$ )	$B_C^*$ (%)	$I^{**}$ (%)	$C_f$ ( $\times 10^{-3}$ )	Error Vs. Case 5
1	0.5	1.0	11.67	0.84	4.502	6.35%
2	1.0	1.0	5.83	0.84	4.265	0.76%
3	1.5	1.0	3.89	0.84	4.236	0.08%
4	2.0	1.0	2.92	0.84	4.233	-0.01%
5	3.0	1.0	1.94	0.84	4.233	0.00%
6	3.0	1.5	1.94	0.60	4.171	-1.46%
7	3.0	2.0	1.94	0.49	4.140	-2.19%
8	3.0	3.0	1.94	0.38	4.117	-2.75%
9***	3.0	3.0	1.94	0.85	4.232	-0.03%

\*  $B_C$ : Blockage coefficient, the ratio between the area of the ship midsection and the area of the waterway section;

\*\*  $I$ : The turbulent intensity recorded at  $0.5 L_{pp}$  in front of the ship with  $y = 0$  at the suppressed water surface;

\*\*\* Case 9: An additional case based on Case 8 by increasing  $I$  deliberately to a similar level to Case 5.

- If  $B_C$  is less 3.9%, further reducing  $B_C$  makes little difference to  $C_f$ .

In this chapter, the value of  $B_C$  is guaranteed to be equal to or less than 3.9%. For the KCS at  $1.2 \leq h/T \leq 2.0$ , the side boundary is set at  $1.5L_{pp}$  away from the ship's centerline. For the Rhine Ship 86, the value of  $1.5L_{pp}$  applies for  $1.2 \leq h/T \leq 1.5$ . For other cases, the side boundary is set at  $1.0L_{pp}$ .

For the position of the front boundary (Cases 2 to 9):

- When  $B_C$  is less than 5.8%, the result of  $C_f$  is more sensitive to the position of front boundary than that of the side boundary;
- The further the front boundary away from the ship, the lower the  $C_f$ . This can be explained by the level of turbulence intensity close to the hull, of which the values are 0.84%, 0.60%, 0.49%, and 0.38% for  $1.0L_{pp}$ ,  $1.5L_{pp}$ ,  $2.0L_{pp}$ , and  $3.0L_{pp}$ . A lower turbulence intensity leads to a lower  $C_f$ ;
- In Case 9,  $I$  of the upcoming flow is increased to 0.85% and the rest settings are the same as Case 8. It can be found that  $C_f$  of Case 9 has a minor difference from Case 5, which means the turbulent intensity, instead of the position of the front boundary, dominates the changes of  $C_f$ . Therefore, Case 5 is preferred due to fewer grid cells and thus less computing time.

In the simulations of this chapter, the initial flow is unidirectional and thus, the turbulence intensity decays fast before reaching the ship. For a natural river or canal, the level of turbulence intensity close to the water

surface is usually more than 1% (Kozioł, 2013). To make sure the turbulence intensity is as close as the natural condition, the front boundary at  $1.0L_{pp}$  is preferred and used for all simulations in this chapter. Since a distance less than  $1.0L_{pp}$  is less likely to cope with the backflow, such condition is not considered.

By adjusting the value of  $h$ , seven varied water depths are selected and shown in Table 5.4. In the table,  $h$  is the water depth, and  $T$  the draft of the ship.

Table 5.4: The seven water depths selected in this chapter

No.	$h/T$
1	15.06
2	4.00
3	3.00
4	2.00
5	1.80
6	1.50
7	1.20

### 5.2.3. Mesh Generation and the Solver

Hexahedral mesh is applied to all computations in this chapter. Close to a non-slip wall, the grid is refined to capture the velocity gradient and pressure gradient, and an example is shown in Figure 5.5. For shallow water cases, the number of grid points in the vertical direction is adjusted based on the water depths. For high Reynolds number cases, the mesh is refined in the x direction correspondingly to keep the aspect ratio of the grid cells at an acceptable level.

In this chapter, all numerical calculations were performed in an FVM (Finite Volume Method) code ANSYS Fluent (version 18.1). The SST  $k-\omega$  model is chosen as the turbulence model. The scheme of the pressure-velocity coupling is “Coupled” and the discretization of the gradient is “Least Squares Cell-Based”. For the discretization of pressure, PREssure staggering Option “PRESTO!” is used, and “Second Order Upwind” is applied for the discretization of momentum, turbulent kinetic energy, and specific dissipation rate.

### 5.3. Verification and Validation

In this section, a grid independence study is performed to verify the mesh and the CFD solver. Afterward, the calculations of the frictional resistance of ships are validated with the existing empirical formulas.

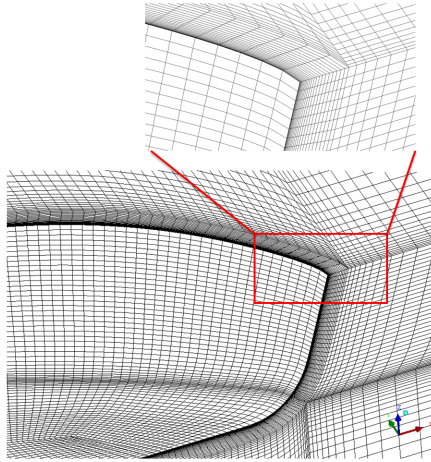


Figure 5.5: The mesh around the bow of the Rhine Ship 86

### 5.3.1. Verification

Calculations should be verified to keep the numerical errors at an acceptable level. When double precision format and suitable convergence criteria are used, the dominant error is the discretization error (Eça and Hoekstra, 2009), which is the main concern in this subsection.

According to Roache (1998) a grid refinement study is an effective way to find the most suitable mesh for calculations. In this verification, four geometrically similar grids (G1 to G4) are built for the 2D flat plate as well as the three ship hulls. The refinement ratio for each direction is 1.25 and the finest grid is G1. A factor  $\alpha$  is defined by multiplying the refinement ratio at different times. It can be used to indicate the density of the mesh (the smaller the finer). Table 5.5 shows the number of nodes in the x, y and z directions for all cases.

The coefficients of the frictional resistance for each grid are compared in Figure 5.6.

The curves shown in Figure 5.6 can be fitted by the method of Eça and Hoekstra (2014):

$$S_{RE}(\phi_0, \beta, p) = \sqrt{\sum_{i=1}^N (\phi_i - (\phi_0 + \beta \alpha_i^p))^2}, \quad (5.2)$$

where  $\phi_0, \beta, p$  are constants derived from the fitting. The uncertainty is calculated by

$$U(\phi_i) = F_s |\phi_i - \phi_0| + S_{RE} + |\phi_i - (\phi_0 + \beta \alpha_i^p)|, \quad (5.3)$$

where  $F_s = 1.25$  if  $0.5 \leq p < 2.1$ , otherwise,  $F_s = 3$ .

Table 5.5: Number of nodes in  $x, y$  and  $z$  directions for the 2D flat plate, the Wigley hull, the KCS, and the Rhine ship 86 (deep water)

	No.	x	y	z	$\alpha$	Total cells (million)
2D flat plate	G1	881	250	-	1.00	0.22
	G2	701	198	-	1.25	0.14
	G3	557	158	-	1.56	0.09
	G4	449	126	-	1.95	0.06
Wigley hull	G1	558	98	122	1.00	6.45
	G2	403	78	98	1.25	3.30
	G3	350	62	78	1.56	1.69
	G4	274	50	66	1.95	0.87
KCS	G1	523	74	168	1.00	8.22
	G2	415	58	132	1.25	4.28
	G3	327	46	96	1.56	2.27
	G4	267	38	84	1.95	1.19
Rhine ship 86	G1	557	65	110	1.00	7.42
	G2	449	53	90	1.25	3.80
	G3	357	41	70	1.56	1.95
	G4	289	33	50	1.95	1.00

Generally, the accuracy of a calculated frictional resistance increases with the refinement of mesh. However, when it reaches a certain accuracy, continued refinements of the mesh will not significantly contribute to the accuracy but will increase the required computing sources. Therefore, instead of searching for the largest possible number of grid cells, a suitable number with an acceptable error is the purpose of this verification.

After comparing the behavior of the four types of mesh, the grid G1 is selected for the 2D flat plate since it has the highest accuracy among the four grids and with acceptable computation time. G2 is selected for all ships based on a balance of the accuracy and computing effort. The corresponding order of accuracy ( $p$ ) and the uncertainty ( $U(\phi_i)$ ) are given in Table 5.6.

Table 5.6: The observed order of accuracy and uncertainty of  $C_f$  for the 2D flat plate, the Wigley hull, the KCS, and the Rhine ship 86

	$p$	$U(\phi_i)$	$U(\phi_i)/\phi_i$
2D flat plate	2.73	$1.814 \times 10^{-5}$	0.50%
Wigley hull	2.82	$8.385 \times 10^{-7}$	0.02%
KCS	2.93	$5.004 \times 10^{-6}$	0.13%
Rhine Ship 86	3.83	$4.359 \times 10^{-6}$	0.12%

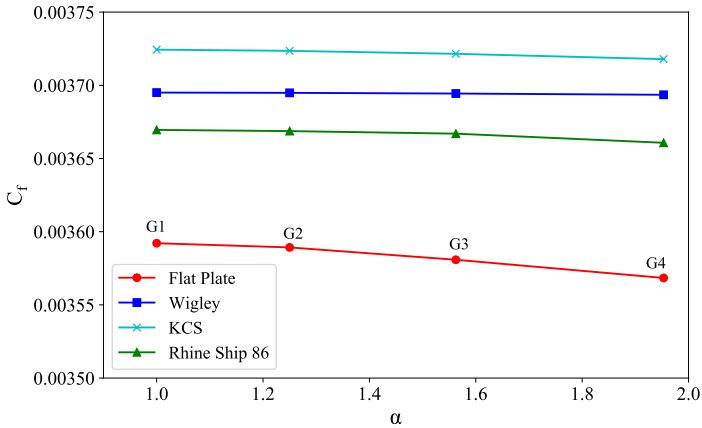


Figure 5.6: Frictional resistance coefficient  $C_f$  with Grid refinement (deep water,  $\lg(Re) = 6.4$ ,  $y^+ = 4$ )

Based on Table 5.6, the uncertainties are at a low level, which means the chosen grids are acceptable and are deemed sufficient for further simulations.

### 5.3.2. Validation

After successfully verifying the simulations, the modeling error should be checked. This error presents the derivation of the numerical results from the experimental data. In this section, calculations are performed with various  $y^+$  and are compared with existing empirical methods. Afterward, the value of the form factor with a conventional definition is validated.

#### Validation of friction

The non-dimensional distance of the first computing point away from the non-slip wall, which is known as  $y^+$ , is defined as follows:

$$y^+ = \frac{u^* y}{\nu}, \quad (5.4)$$

where  $y$  is the dimensional distance of the first computing point to the wall,  $u^*$  the shear velocity and  $\nu$  the kinematic viscosity. A  $y^+$  less than 5 represents the viscous sublayer, and  $30 \leq y^+ \leq 200$  indicates the log-law region (Pope, 2000). It is noteworthy that for Finite Volume Method (FVM), the first computing point is at the center of the first-layer cell.

For numerical simulations,  $y^+$  is usually suggested to be as low as 1 to capture the viscous sublayer. However, the first layer of cells has a very small height if the  $Re$  is high. For example, for the Wigley hull with  $y^+ = 0.5$  and  $Re = 2.512 \times 10^8$ , the height of the first-layer cell is  $3.289 \times 10^{-7}$  m, but the length is normally at the level of  $10^{-2}$  m. The aspect ratio, consequently,

is as high as  $10^5$ , which influences the stability and accuracy of numerical simulations. Even if an aspect ratio of  $10^4$  is guaranteed, the number of cells goes to 9 million which leads to an expensive computation. However, based on a similar refinement, if  $y^+ = 2$ , the number can be reduced to 7 million; if  $y^+ = 30$ , the number can be reduced to 3 million. As the value of  $y^+$  can primarily affect the computing efforts, the  $y^+$  dependency of  $C_f$  is studied to illustrate whether a higher  $y^+$  can be accepted.

In this study, the  $\omega$ -equation is used in the turbulence model. This enables the wall treatment by blending the viscous sublayer formulation and the logarithmic layer formulation based on  $y^+$  (ANSYS, 2017b). The values of  $y^+$  vary at viscous sublayer ( $y^+ < 5$ ) and log-law region ( $30 \leq y^+ \leq 200$ ). Since a slightly larger difference is observed during the transition range ( $5 \leq y^+ < 30$ ), which was depicted in Figure 4.9 of Chapter 4, this range is skipped in this chapter.

In Figure 5.7, the results of  $C_f$  of the 2D plate, the Wigley hull and the KCS calculated in varied  $y^+$  are shown at three Reynolds numbers. The friction line of Katsui et al. (2005) and the ITTC57 model-ship correlation line (ITTC, 1957) are used for comparison.

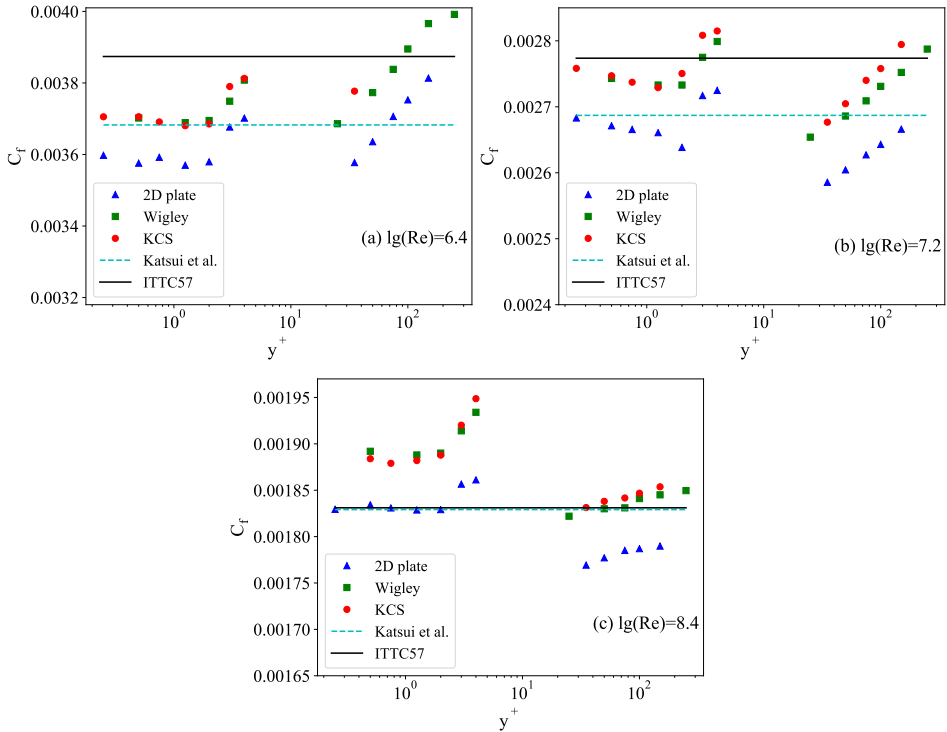


Figure 5.7: The results of  $C_f$  in varied  $y^+$  for (a):  $\lg(Re) = 6.4$ , (b):  $\lg(Re) = 7.2$ , and (c):  $\lg(Re) = 8.4$  (deep-water cases)

Some remarks can be derived from Figure 5.7:

- Minor differences are found for the calculated  $C_f$  between the two chosen ships, despite the distinct ship forms;
- For  $y^+ < 5$ , the results of  $C_f$  of both the flat plate and the ships are stable, especially for  $\lg(Re) = 6.4$  and  $8.4$ , where the differences from the average value less than 1%;
- For  $30 \leq y^+ \leq 200$ , larger differences are observed (up to 4%);
- From the verification perspective,  $y^+ < 1$  should be selected as the benchmark since it directly resolves the boundary layer. Based on this, results generated with the  $y^+ < 5$  are more accurate and stable than  $30 \leq y^+ \leq 200$ ;
- From the validation perspective, the numerical results should be compared with the existing experiments. If the friction line proposed by [Katsui et al. \(2005\)](#) is used as the benchmark for both the 2D flat plate and ships,  $y^+ < 5$  can give better results than  $30 \leq y^+ \leq 200$  at  $\lg(Re) = 6.4$  and  $7.2$ ; If the ITTC57 correlation line is used as the benchmark for ships, calculations with  $y^+ < 5$  behave better only for  $\lg(Re) = 7.2$ .

In summary,  $y^+ < 5$  is preferred due to more stable results and practically acceptable errors. As a relatively higher  $y^+$  can help to reduce the grid cells and consequently save the computing efforts,  $y^+ = 2$  is chosen for all simulations of the flat plate and the ships subsequently.

The water bottom is another non-slip wall, and the mesh close to it has also been refined. Since it moves at the same speed as the incoming water in computations, the Reynolds number defined with the relative velocity (to the water) is low and therefore a small  $y^+ (\approx 1)$  is easily guaranteed in all cases.

### Validation of form factor

The conventional definition of form factor is shown as follows:

$$1 + k = \frac{C_v}{C_f}, \quad (5.5)$$

where  $C_v$  is the coefficient of the viscous resistance, which is the sum of the coefficients of frictional resistance and the viscous pressure resistance. For  $C_f$ , there was a debate on which line should be used to determine  $1 + k$  ([ITTC, 2008](#)), but finally a true turbulent flat plate friction line instead of the ITTC57 correlation line was suggested ([ITTC, 2017j](#)). In this validation, therefore, CFD results of  $1 + k$  are calculated based on  $C_f$  computed on the 2D flat plate.

The values of  $1 + k$  in deep and shallow water for the Wigley hull, the KCS, and the Rhine Ship 86 are validated with the experimental data, as shown

in Figure 5.8. Corrections of shallow water effects proposed by Millward (1989) and Raven (2016) are applied. The form factors of the three ships in deep water, which are derived following the method of Prohaska (1966), are also shown for comparison. In deep water, the form factor is assumed to be constant (ITTC, 2017j).

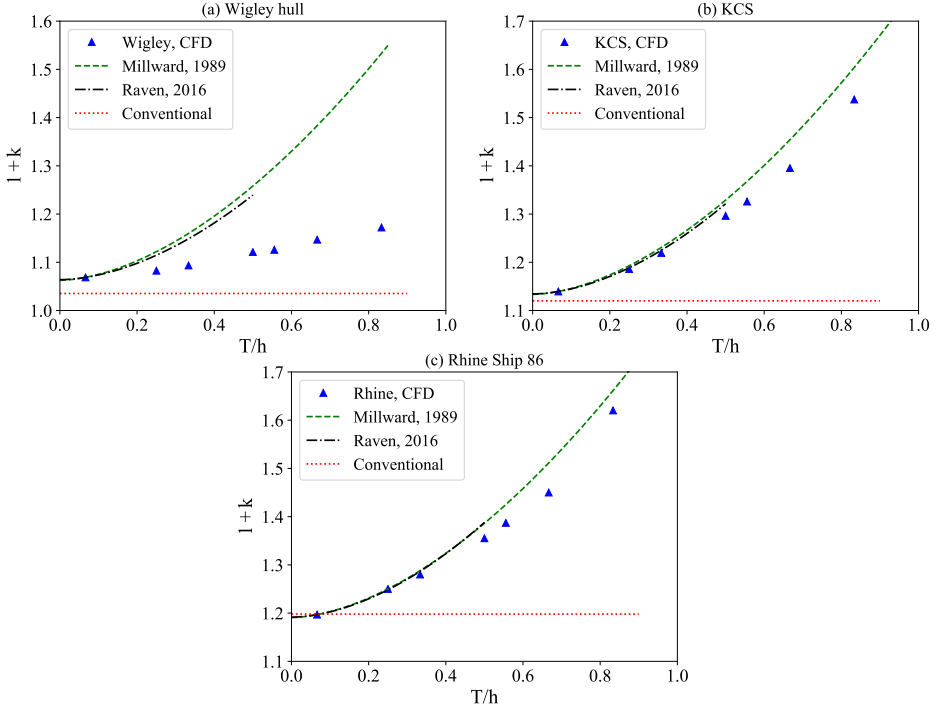


Figure 5.8: Comparisons between CFD results of  $1+k$  (this study) and empirical methods for (a): Wigley hull, (b): KCS, and (c): Rhine Ship 86 ( $\lg(Re)=6.4$ ,  $y^+ = 2$ ); Conventional results are based on deep water model tests: Kajitani et al. (1983) for the Wigley hull, Lee et al. (2018) for the KCS, and test data in Chapter 3 for Rhine Ship 86

Based on ship model tests, Millward (1989) proposed a modification of form factor considering shallow water effects as follows:

$$\Delta k = 0.644(h/T)^{-1.72}. \quad (5.6)$$

More recently, Raven (2016) fitted a new line for form factor correction in shallow water based on double-body computations for different ship types, at both model scale and full scale, as shown in equation (5.7):

$$(1+k)/(1+k)_{deep} = 1 + 0.57(h/T)^{-1.79}, \quad (5.7)$$

where  $h$  is water depth and  $T$  is ship draft. The equation (5.7) is applicable for  $h/T > 2.0$ .

Comparisons are made at  $\lg(Re) = 6.4$ . The value of  $C_f$  on the 2D flat plate is used for calculating  $1 + k$  since it uses the same turbulence model and the same  $y^+$  value as used in the ship simulations.

It can be derived from Figure 5.8 that:

- For the Wigley hull, the CFD result of  $1 + k$  in deep water is slightly larger than the experiment (3.2%). In shallow water, the values of  $1 + k$  are smaller than empirical methods. This discrepancy is due to the much fuller shape of the ships which were used to derive the empirical methods;
- For the KCS and Rhine Ship 86, the calculated  $1 + k$  have a good agreement with both the experimental and empirical data in both deep and shallow water. It means at least for these two ships, the numerical simulations for  $1 + k$  are acceptable;

Therefore, the CFD method used in this study can be trusted and will be used in the systematic calculations. The empirical methods of Millward (1989) and Raven (2016) only considered the effects of water depth. In Section 5.4.2, the effects of water depth and Reynolds number will be considered simultaneously.

## 5.4. Results and Analysis

In this section, numerical results of the frictional resistance of the 2D flat plate and the ships in deep water are first compared to demonstrate the form effects of a 3D ship hull. Afterward, shallow water effects on ship's friction are analyzed and the new correlation line is introduced. Also, the form factors of the three chosen ships in shallow water are discussed separately.

### 5.4.1. The Frictional Resistance

#### Comparison between the flat plate and the ships

For the frictional resistance, the crucial difference between a flat plate and a ship is the curved surface. In Figure 5.9, the results of the frictional resistance coefficient ( $C_f$ ) are shown against the base-10 logarithm of the Reynolds number ( $\lg(Re)$ ) in deep water.

A numerical formula is fitted for the 2D flat plate:

$$C_{f-2Dplate} = \frac{0.07521}{(\lg Re - 1.691)^{1.956}} \quad (5.8)$$

When the ship sails in shallow water, the presence of the water bottom affects the ship's friction further. It plays a similar role to the curved surface and acts as an additional form effect, which will be introduced in detail in the next part.

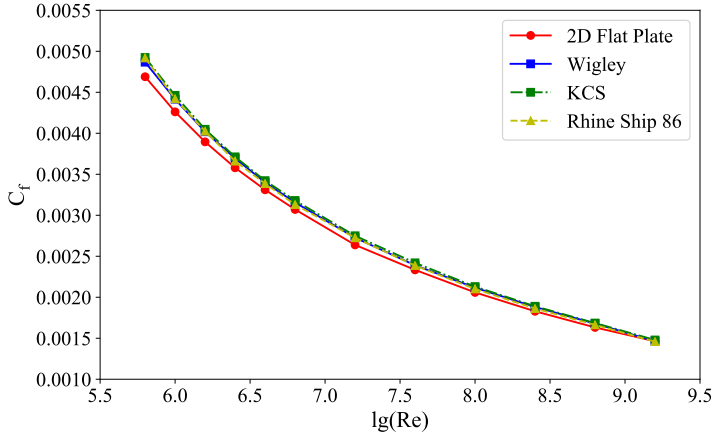


Figure 5.9: The results of the frictional resistance coefficient ( $C_f$ ) against  $\lg(Re)$  for the 2D flat plate, the Wigley hull, the KCS, and the Rhine Ship 86 (deep water)

### Comparison between the Wigley hull, the KCS, and the Rhine Ship 86

The results of  $C_f$  in various water depth for the three ship types are illustrated in Figure 5.10, Figure 5.11, and Figure 5.12.

Despite the similarity of the friction curves in deep water, they show more considerable differences in shallow water. This is caused by the differences in the area of the flat bottom or a different block coefficient ( $C_B$ ). Although the increase of  $C_f$  for the KCS and the Rhine ship 86 are similar, shallow water effects on  $C_f$  of the Wigley hull are minor, which implies a ship form dependency of  $C_f$  in shallow water.

To find an expression to express the frictional resistance for the three ships in varied water depth, a two-step regression is proposed. First, based on the results in deep water, a formula suitable for the three ships is fitted with MATLAB. The format is similar to the ITTC57 line and shown as follows:

$$C_{f-deep} = \frac{0.08468}{(\lg Re - 1.631)^2}. \quad (5.9)$$

Secondly, considering shallow water effects, the correlation line can be given as

$$C_f = \frac{0.08468}{(\lg Re - 1.631)^2} \cdot \left( 1 + \frac{c_1}{\lg Re + c_2} \cdot \left( \frac{h}{T} \right)^{c_3} \right). \quad (5.10)$$

$Re$  — Reynolds number;

$h$  — the water depth;

$T$  — the draft of the ship.

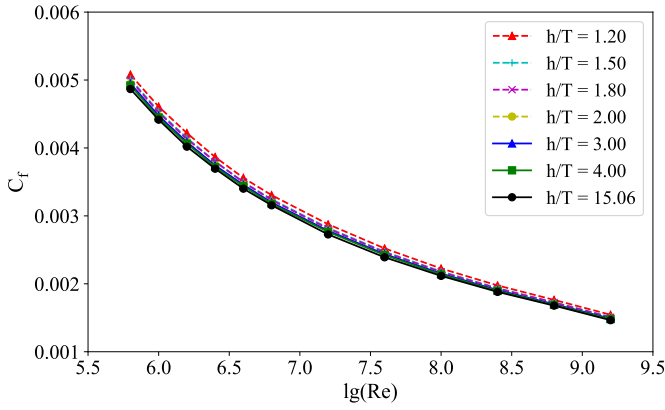


Figure 5.10: The frictional resistance coefficient ( $C_f$ ) against  $\lg(Re)$  in different water depth for the Wigley hull

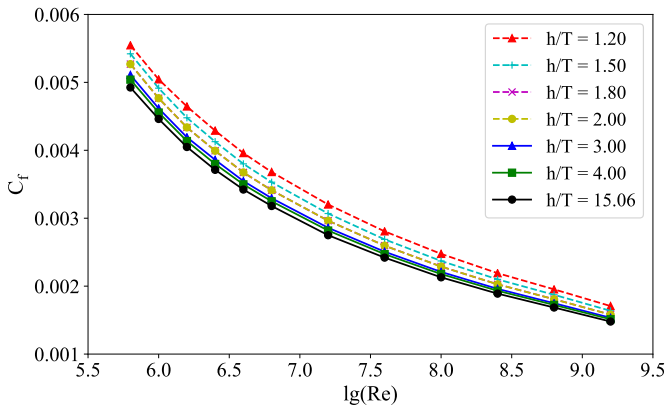


Figure 5.11: The frictional resistance coefficient ( $C_f$ ) against  $\lg(Re)$  in different water depth for the KCS

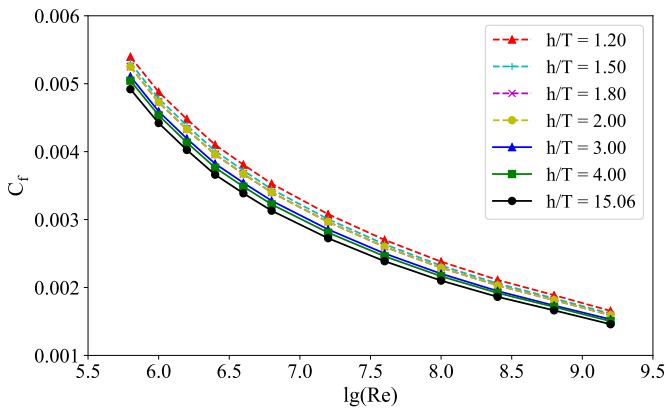


Figure 5.12: The frictional resistance coefficient ( $C_f$ ) against  $\lg(Re)$  in different water depth for the Rhine Ship 86

$c_1$ ,  $c_2$ , and  $c_3$  are constants determined per ship type. Expression 5.10 is suitable for the selected three ship types sailing in shallow water. The constants are fitted with 95% confidence bounds, which are provided in Table 5.7.

Table 5.7:  $c_1$ ,  $c_2$ , and  $c_3$  for the Wigley hull, the KCS, and the Rhine Ship 86

	$c_1$	$c_2$	$c_3$
Wigley hull	0.3466	-0.4909	-1.461
KCS	1.2050	-0.5406	-1.451
Rhine Ship 86	1.1680	-0.5238	-1.472

For the three ships, the value of  $c_2$  varies in a small range (0.49 - 0.55), and a similar conclusion applies to  $c_3$  (1.45 - 1.48). However, the value of  $c_1$  of the Wigley hull differs significantly with the other two ships. This is likely caused by the difference in the characteristics of the ship hull surface.

5

#### A general method to predict the frictional resistance

For ships very different from the selected three ships, equation (5.10) might not apply since no ship parameters are included in this expression. However, the data obtained in this section can be used to build a more general method for  $C_f$  prediction. This method will be established on a concept of “equivalent draft”.

For pure shallow water (with enough lateral space), changes of  $C_f$  are found on the surface facing to the water bottom. Based on this, a virtual ship with a rectangular shape of crosssections is used, as shown in Figure 5.13. Shallow water effects on  $C_f$  are all included on the bottom of the rectangular, and  $C_f$  on the vertical area can be calculated using deep water methods. When  $C_f$  of the virtual ship equals to the target ship, the draft of the virtual ship ( $T_e$ ) is treated as an “equivalent draft”, which has a relation with the draft ( $T$ ) of the target ship as follows:

$$T_e = \gamma \cdot T, \quad (5.11)$$

where  $\gamma$  is the equivalent factor.

Factor  $\gamma$  is assumed to indicate the fullness of the vessel. The total friction coefficient can be represented by the friction coefficient on the vertical area ( $C_{fv}$ ) and the friction coefficient on ship's bottom ( $C_{fb}$ ):

$$C_f = C_{fv} \cdot \frac{S_v}{S} + C_{fb} \cdot \frac{S_b}{S}. \quad (5.12)$$

The vertical area ( $S_v$ ) is calculated by  $2 \cdot L \cdot (\gamma \cdot T)$ . The area of the flat bottom ( $S_b$ ) is calculated by  $L \cdot B$ . Symbol  $S$  is the wetted surface of the target ship.  $C_{fv}$  can be calculated by the ITTC57 correlation line. In this study, a numerical friction line was fitted for the ships in deep water (equation (5.9))

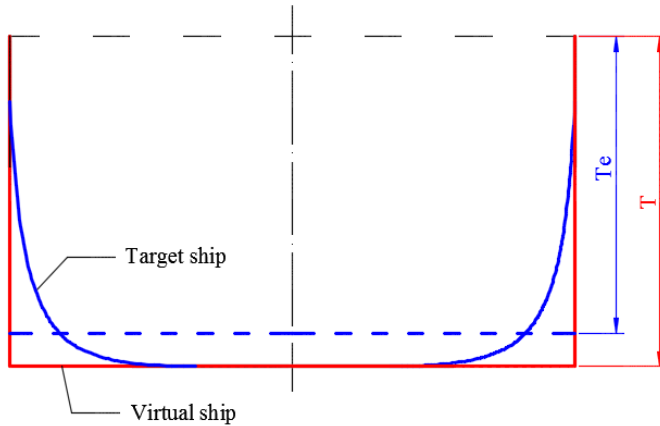


Figure 5.13: The virtual ship and the equivalent draft  $T_e$

and will be applied.  $C_{fb}$  can be calculated by the numerical friction line fitted for a 2D flat plate in shallow water (Chapter 4, equation (4.13)). Errors caused by the velocity of the incoming flow (the incoming flow velocity for the flat plate, here ship's flat bottom, is usually not equal to the initial velocity at the inlet boundary) are also included into the equivalent factor  $\gamma$ .

Based on  $C_f$  that obtained for the Wigley hull, the KCS, and the Rhine Ship 86 in shallow water, factor  $\gamma$  can be given as follows:

$$\gamma = -\frac{c_1}{(\lg Re - 2)^2} + c_2 \cdot e^{-(h/T)^{0.06}} \quad (5.13)$$

where  $c_1 = 5.7472 \cdot C_B - 1.2989$  and  $c_2 = 0.5738 \cdot e^{1.8493 \cdot C_B}$ .

Equivalent factor  $\gamma$  depends on  $Re$ ,  $h/T$ , and  $C_B$ . For the same sailing conditions, the higher the  $C_B$ , the larger the factor  $\gamma$ , as an example shown in Figure 5.14.

Equation (5.12) can be used to calculate the coefficient of the frictional resistance for a ship very different from the selected three ships. Equation (5.13) can be referred to calculate the corresponding equivalent factor  $\gamma$ .

### 5.4.2. The Viscous Pressure Resistance

In Section 5.4.1, the shallow water effects on frictional resistance have been discussed. During double-body computations, the second part of the total resistance, the viscous pressure resistance, can be obtained separately by integrating the pressure on the ship surface in the longitudinal direction. The CFD results of frictional resistance in Section 5.4.1 will be used in the computations of the form factor.

Due to the influence of viscosity, the water loses kinetic energy when it passes from the bow to the stern and forms a pressure difference. The

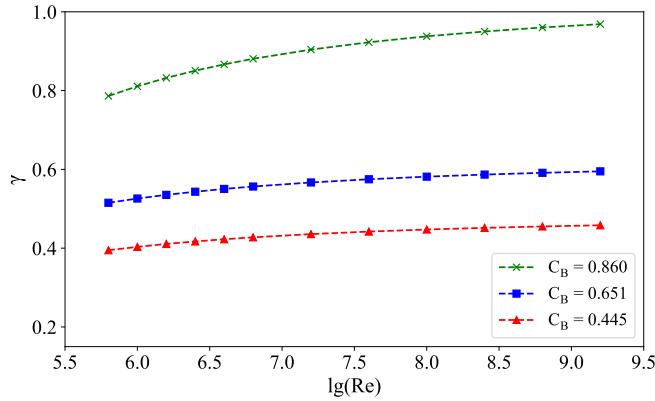


Figure 5.14: Equivalent factor  $\gamma$  for the Wigley hull ( $C_B = 0.445$ ), the KCS ( $C_B = 0.651$ ), and the Rhine Ship 86 ( $C_B = 0.860$ ) against  $\lg(Re)$  at  $h/T = 1.2$

## 5

resistance caused by this kinetic energy loss is called the viscous pressure resistance. In this subsection, a new definition of the form factor is proposed searching for a stronger physical basis. The results of the new-defined form factor of the three chosen ships are analyzed in sequence.

#### A new definition of form factor in shallow water

If one keeps using a flat plate friction line in the definition of form factor, shallow water effects on both the friction and the viscous pressure resistance are included simultaneously in the form factor, which weakens the physical basis of this factor, i.e., a part of shear force is transferred into the form factor. To remedy this, the computed friction ( $C_{fc}$ ) of the ship is recommended to define the form factor in shallow water, by which all shear forces are kept in the friction. To distinguish it from the conventional way, an asterisk is used:

$$1 + k^* = \frac{C_v}{C_{fc}} \quad (5.14)$$

By this definition, the factor  $k^*$  clearly represent the viscous pressure resistance. Meanwhile, the  $1+k^*$  is not expected to be constant with ship scales, since its Reynolds number dependency will be observed to be even more pronounced in shallow water.

In principle, it is required to keep the influence of transom outside the form factor (ITTC, 2017j), but it is hard to put into practice. For a large number of inland ships, the immersed transom is commonly found, as well as the backward-facing tunnel endings, as shown in Figure 5.15. Their effects are already included in the form factor derived from, e.g. double-body computations. There are, at least to the author's knowledge, no reliable methods to separate it precisely from form factor.



Figure 5.15: An inland ship with a transom and backward-facing tunnel endings (Rotteveel, 2019)

Physically, the influence of the transom is also a part of viscous pressure resistance; thus, for practical reasons, it is considered as form effects. Therefore, keeping such influence inside the form factor is also nominally acceptable. Based on this, the  $1+k^*$  can also be seen as an indicator to show transom effects on the viscous pressure resistance of a quite number of inland vessels.

Form factor of the Wigley hull

As shown in Figure 5.16, the CFD results of  $1+k^*$  against the  $\lg(Re)$  for the Wigley hull are demonstrated.

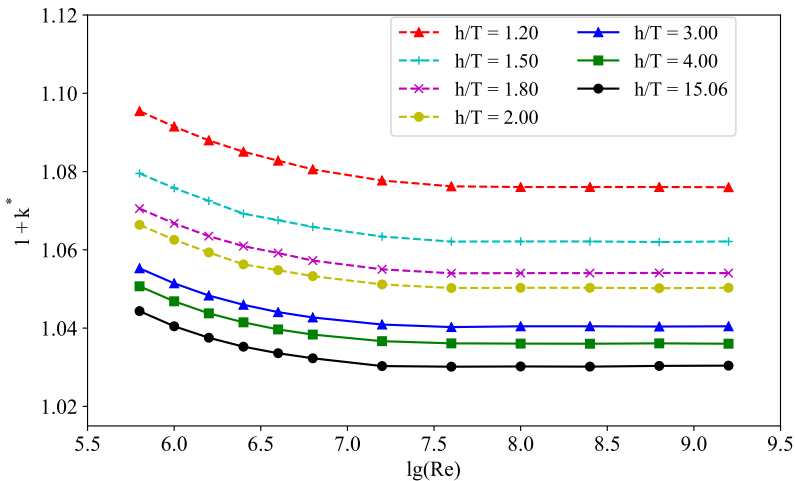


Figure 5.16: The form factor against  $\lg(Re)$  for the Wigley hull with different water depths

Based on Figure 5.16:

- The  $1+k^*$  decreases with  $Re$  when  $\lg(Re) < 7.2$  and becomes stable for higher  $Re$ ;
- A smaller  $h/T$  indicates a higher  $1+k^*$  and the curves of  $1+k^*$  for different water depth are approximately parallel;
- Water depth affects the  $1+k^*$  more than  $Re$ . For  $h/T = 1.2$  and  $\lg(Re) = 5.8$ , the  $1+k^*$  increases by about 5% than  $\lg(Re) = 5.8$  in deep water, but by about 1.8% than  $h/T = 1.2$  and  $\lg(Re) = 9.2$ ;
- For the same  $h/T$ , smaller  $1+k^*$  is usually observed for a relatively higher  $Re$ . It can be explained by a thinner boundary layer at a higher Reynolds number, where a smaller proportion of kinetic energy is dissipated.

## 5

The presence of water bottom provides an additional boundary layer and will interact with the ship's boundary layer when the water is shallow enough. Figure 5.17 shows a comparison of the velocity distribution at the stern section when  $\lg(Re) = 6.4$ . As indicated in the figure, the ship's boundary layer is enlarged in the shallow water case, particularly in the region where the interaction of the two boundary layers occurs. The water, therefore, will be less likely to go back to its initial velocity when it arrives at the stern area.

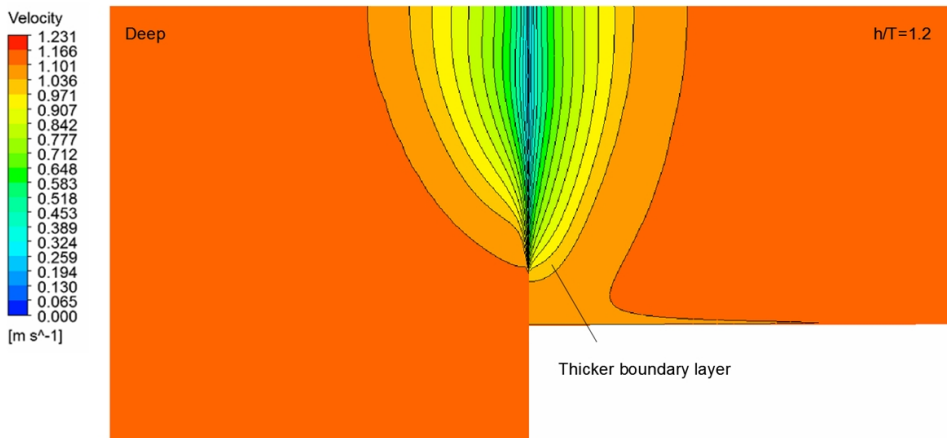


Figure 5.17: The velocity distribution at the stern section ( $x = 0$  m) for  $h/T = 15.06$  (deep) and  $h/T = 1.20$  when  $\lg(Re)=6.4$  for the Wigley hull

A regression of the form factor depending on both the Reynolds number and water depth is proposed for the Wigley hull:

$$(1 + k^*)_{Wigley} = \left( 1.03 + \frac{1.276}{(\lg Re - 3.277)^{4.79}} \right) \cdot \left( 1 + 0.06303 \cdot \left( \frac{h}{T} \right)^{-1.7} \right) \quad (5.15)$$

The first part of equation (5.15) represents the form factor in deep water. The constant 1.03 is the form factor for the Wigley hull at  $\lg(Re) \geq 8.0$  in deep water. The second part represents shallow water effects, which will reduce to one when the water is deep enough. This formula is valid for  $h/T \geq 1.2$ , which is in line with the minimum water depth in the calculations.

### Form factor of the KCS

Numerical results of  $1+k^*$  for the KCS are depicted in Figure 5.18.

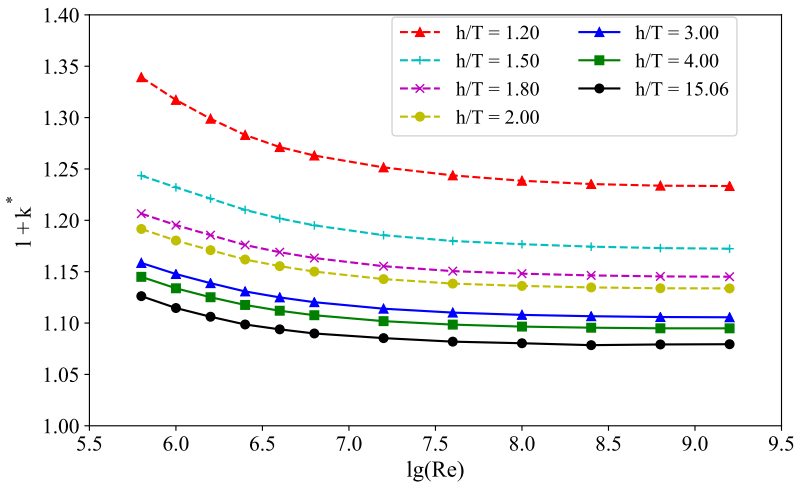


Figure 5.18: The form factor against  $\lg(Re)$  for the KCS with different water depths

Similar to the Wigley hull, the form factor becomes stable for  $\lg(Re) > 7.2$ . However, the response of the KCS is more significant than the Wigley hull:

- For the same water depth, considerable influence of  $Re$  on  $1+k^*$  is observed. For  $h/T = 1.2$ , the maximum change of  $C_f$  caused only by  $Re$  is about 8.6% which is more distinct than that for the Wigley hull (1.8%);
- For the same  $Re$ , water depth can cause about 18% increase of  $1+k^*$  at  $h/T = 1.2$  and  $\lg(Re) = 5.8$  compare to deep water, but the value is about 5% for the Wigley hull.

Therefore, the effects of ship forms are enlarged in shallow water, and corrections of shallow water effects on the form factor should be made per ship. Based on the numerical results, the prediction of  $1+k^*$  for the KCS in shallow water can be fitted as

$$(1+k^*)_{KCS} = \left( 1.075 + \frac{1.086}{(\lg Re - 3.419)^{3.513}} \right) \cdot \left( 1 + 0.2066 \cdot \left( \frac{h}{T} \right)^{-1.887} \right) \quad (5.16)$$

### Form factor of the Rhine Ship 86

For a thin and streamlined surface like Wigley hull, flow separation and vorticity are not observed obviously. However, for ships with a transom like the Rhine Ship 86, vortices are generated behind the stern, and the conclusions about the form factor derived from the previous sections may be subject to change.

The results of  $1+k^*$  against the  $\lg(Re)$  for the Rhine Ship 86 in different water depths are displayed in Figure 5.19.

From Figure 5.19, it can be seen that:

- Different from the two ships discussed previously, the  $1+k^*$  encounter an increase starting at  $\lg(Re) \approx 6.6$  making its  $Re$  dependency more complicated;
- Shallower water will lead to a higher  $1+k^*$ . For  $h/T = 1.20$ , the  $1+k^*$  increases by 19.7% at  $\lg(Re) = 5.8$  and 8.2% at  $\lg(Re) = 9.2$ .

In Figure 5.20, the  $1+k^*$  of the Wigley hull, the KCS, and the Rhine Ship 86 at  $h/T = 15.06$  (deep water) and  $h/T = 1.20$  (shallowest case) are compared.

Based on Figure 5.20:

- As expected, the Wigley hull, of which the block coefficient is the smallest, receives the lowest influence of water depth on its form factor;
- The effects on the form factors of the KCS and the Rhine Ship 86 are at the same level of magnitude;
- Designs with an immersed transom such as the Rhine Ship 86, the mechanism of shallow water effects on the viscous pressure resistance subject to different rules compared to those without a transom when the  $Re$  is sufficiently high.

The different trend of the form factor of the Rhine Ship 86 can be explained by the vortices formed due to the blunt stern and/or the transom. A vertical vortex and a horizontal vortex, as shown in Figure 5.21, are generated and their cores are interconnected and provides a low-pressure region behind the stern.

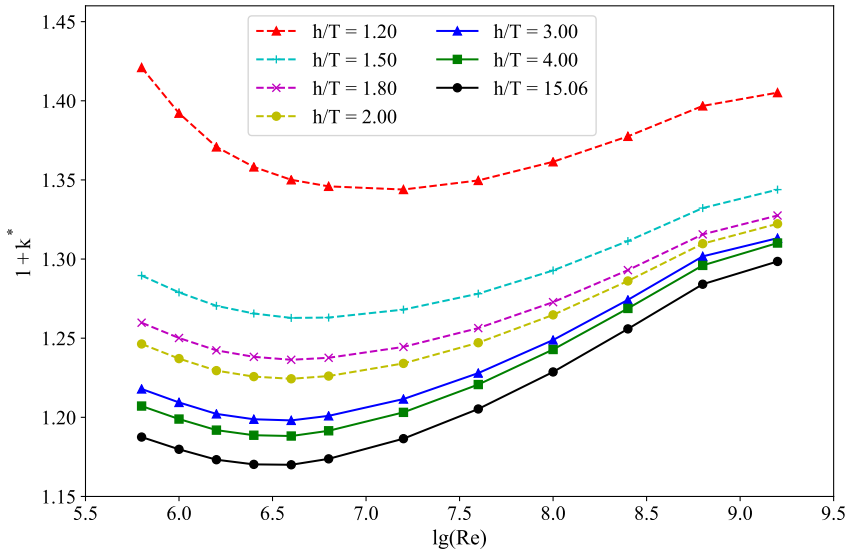


Figure 5.19: The form factor against  $\lg(Re)$  for the Rhine Ship 86 in deep and shallow water

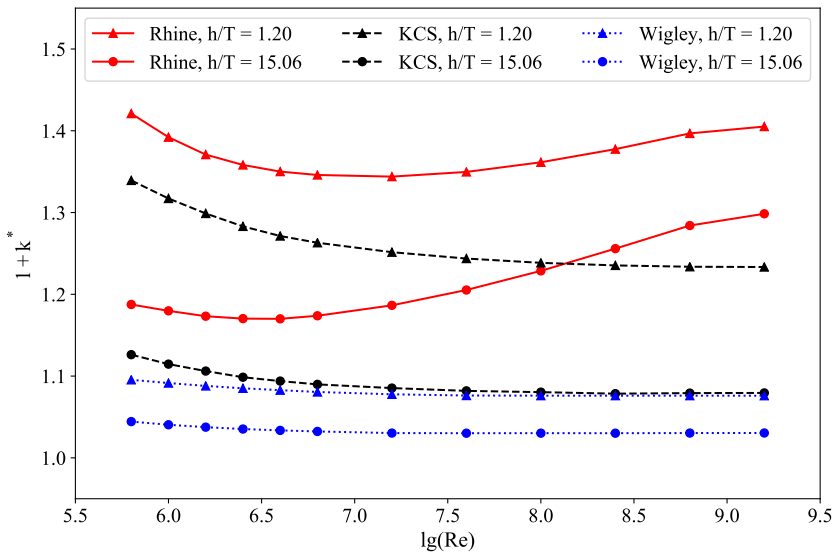


Figure 5.20: Comparisons of the form factors of the Wigley hull, the KCS, and the Rhine Ship 86 in deep water ( $h/T = 15.06$ ) and  $h/T = 1.20$

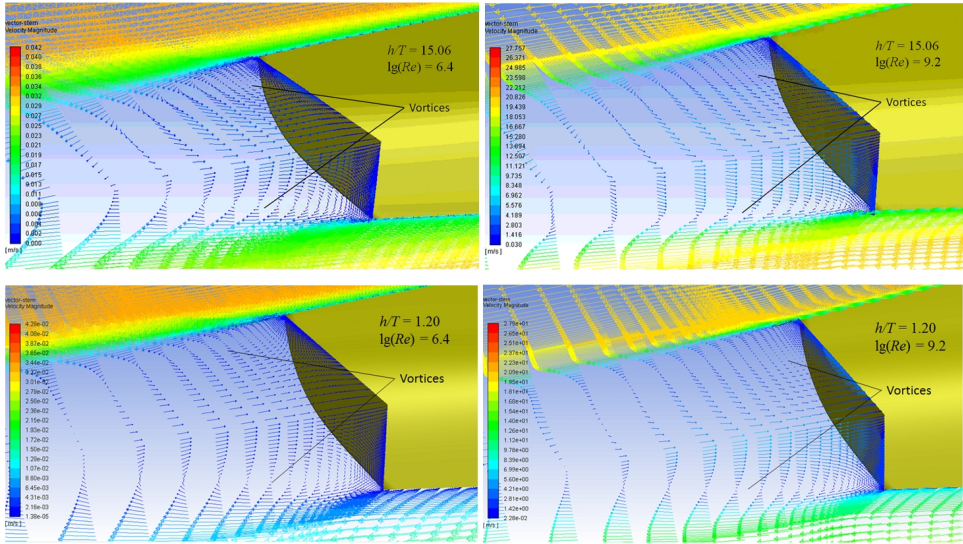


Figure 5.21: The vortices generated after the stern for  $\lg(Re) = 6.4$  and  $\lg(Re) = 9.2$  in deep water (top) and shallow water (bottom)

For a relatively high Reynolds number, the pressure in the vortex core is even lower, both for deep water and shallow water (Figure 5.22). This phenomenon can lead to a larger pressure difference between the bow and the stern, which determines a larger  $1+k^*$ .

Compared with the influence of the 3D boundary layer, which leads to a smaller  $1+k^*$  at higher  $Re$ , the vortex plays the opposite role and is dominant for  $\lg(Re) \geq 7.0$ . Figure 5.23 shows a qualitative demonstration of the contributions of ① ship's boundary layer and ② ship's form effects (e.g., vortex) to the  $1+k^*$  against the Reynolds number.

The ship's form, the water depth, and the transom can all be counted as form effects, therefore the "form factor" is still nominally appropriate to describe the viscous pressure resistance for a ship with a transom. An adjusted formula considering shallow water effects and the transom is suggested for Rhine Ship 86 for  $h/T \geq 1.2$ :

$$(1+k^*)_{RhineShip86} = (1+k^*)_{Wigley} + \left(-0.004165 \cdot (\lg Re)^3 + 0.1085 \cdot (\lg Re)^2 - 0.8726 \cdot \lg Re + 2.367\right) \cdot \left(1 + 1.269 \times 10^4 \cdot (\lg Re)^{-6.155} \cdot (h/T)^{-4.04}\right) \quad (5.17)$$

The first part of equation (5.17) is the form factor of the Wigley hull, which shows the basic effects of the boundary layer caused by a mildly curved ship, corresponding to curve ① in Figure 5.23. The remaining part

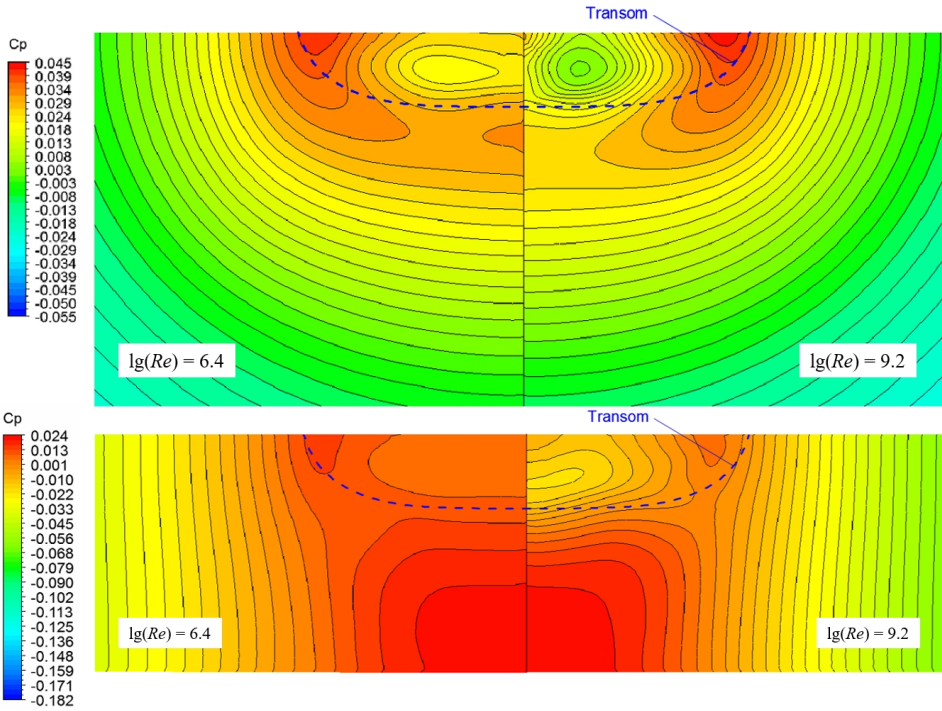


Figure 5.22: The contours of pressure coefficient  $C_p$  (pressure/ $(0.5\rho V^2)$ ) at the section  $x = -2.5\%L$  after the stern for  $\lg(Re) = 6.4$  and  $\lg(Re) = 9.2$  at deep water (top) and  $h/T = 1.2$  (bottom)

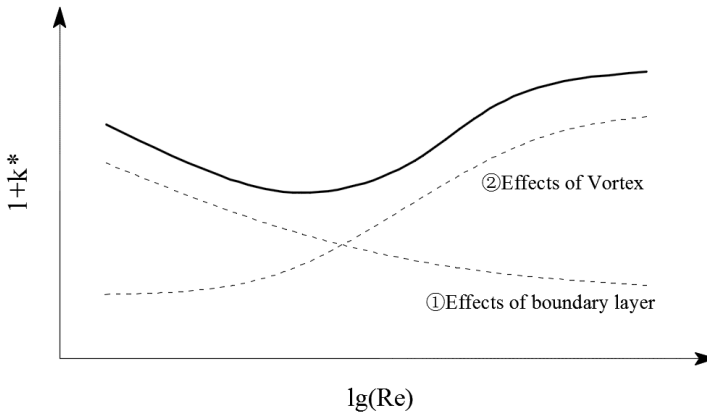


Figure 5.23: A qualitative demonstration of the contributions of the 3D boundary layer and the vortex to the  $1+k^*$  against the Reynolds number for the Rhine Ship 86

of 5.17 represents the effects of ship form, such as an altered boundary layer, ship-generated vortices, etc., corresponding to curve ② in Figure 5.23. It should be noticed that the remaining part of equation (5.17) can be improved by including more parameters of the ship, such as the geometric parameters of the transom, but a study of various hull forms are subject to further investigations.

Additionally, in this dissertation, the sinkage of a ship is considered by regarding the position of the fixed ship as the final position in the stable navigation. However, the results derived in this section might not be applicable for the ships of which the features of the wetted surface change obviously with sinkage. For example, the KCS has a small area of wetted transom at the designed waterline. This area will not cause noticeable influence on the form factor according to CFD results in this section, but it can make a difference if the wetted transom increases with sinkage. A study on these changes is also recommended for future research.

## 5

### 5.4.3. The Significance of Shallow Water Effects on Viscous Resistance

In the previous sections, shallow water effects on the viscous resistance of three ships are studied and empirical expressions are fitted. It will be valuable and also straightforward to show the significance of how the viscous resistance deviates from that in deep water.

According to ITTC guidelines (ITTC, 2017j), the total resistance of a full-scale ship can be extrapolated from model tests through

$$C_{ts} = (1 + k_s)C_{fs} - (1 + k_m)C_{fm} + C_{tm}, \quad (5.18)$$

$C_t$  is the total resistance coefficient, and the subscripts  $s$  and  $m$  represent full scale and model scale, respectively. In the guidelines,  $C_f$  is calculated by the ITTC57 correlation line, and the  $1+k$  is obtained by the method of Prohaska (1966). Based on this chapter, shallow water effects can lead to more significant discrepancies for the frictional resistance. Meanwhile, a different definition of the form factor  $1+k^*$  is proposed to strengthen its physical basis.

To show the discrepancy between the conventional approach and the method proposed in this chapter, an example is given in Table 5.8, where the increase of  $C_f$ ,  $1+k^*$ , and  $(1+k^*)C_f$  compared to the conventional way are shown for the three ships at  $h/T = 1.2$ .

Based on Table 5.8, it is found that:

- Both  $C_f$  and  $1+k^*$  can increase by more than 10% than the conventional way.
- For slender ship like the Wigley hull, the changes of  $(1+k^*)C_f$  is up to 10% for both model-scale and full-scale ships. However, for fuller ships like the KCS and the Rhine Ship 86, the value can even reach

Table 5.8: The difference of  $C_f$ ,  $1+k^*$ , and  $(1+k^*) C_f$  caused by shallow water effects from the conventional approach for the three ships ( $h/T = 1.2$ )

lg(Re)	Wigley hull			KCS			Rhine Ship 86		
	$C_f$	$1+k^*$	$(1+k^*) C_f$	$C_f$	$1+k^*$	$(1+k^*) C_f$	$C_f$	$1+k^*$	$(1+k^*) C_f$
5.8	4.37%	4.89%	9.47%	12.61%	18.92%	33.92%	10.22%	19.66%	31.89%
6.0	4.37%	4.90%	9.48%	13.06%	18.17%	33.61%	12.88%	18.00%	33.20%
6.2	4.97%	4.86%	10.07%	14.73%	17.42%	34.72%	15.13%	16.85%	34.52%
6.4	4.64%	4.81%	9.68%	15.53%	16.79%	34.94%	16.65%	16.06%	35.38%
6.6	4.68%	4.76%	9.66%	15.68%	16.22%	34.45%	17.53%	15.39%	35.62%
6.8	4.73%	4.68%	9.63%	15.81%	15.89%	34.22%	17.99%	14.67%	35.29%
7.2	5.50%	4.60%	10.35%	16.42%	15.31%	34.24%	18.52%	13.27%	34.24%
7.6	5.49%	4.47%	10.21%	16.21%	14.96%	33.59%	18.84%	11.98%	33.08%
8.0	5.15%	4.45%	9.83%	16.29%	14.64%	33.31%	19.01%	10.81%	31.88%
8.4	5.05%	4.45%	9.73%	16.07%	14.54%	32.94%	19.16%	9.69%	30.71%
8.8	5.03%	4.44%	9.69%	15.88%	14.32%	32.47%	19.23%	8.77%	29.70%
9.2	5.45%	4.42%	10.12%	15.43%	14.27%	31.90%	19.29%	8.21%	29.09%

30%, which means the prediction of the viscous resistance will be about 30% less if the conventional approach is used;

- Different from the conventional approach,  $C_f$  is affected by ship forms, and the discrepancy can be as large as 15%.

Therefore, the extrapolation method given by equation (5.18) should be reevaluated in shallow water. Following the format of equation (5.18), a similar method is suggested as follows:

$$C_{ts} = (1 + k_s^*)C_{fs} - (1 + k_m^*)C_{fm} + C_{tm}, \tag{5.19}$$

where  $C_f$  should be given by an improved friction correlation line considering shallow water effects, such as the empirical formulas shown in Section 5.4.1. The term  $1+k^*$  should be calculated with the method proposed in Section 5.4.2, where for vessels similar to the three selected ships, the empirical formulas can be applied directly. For other ships, a more general prediction of the form factor needs to be further established. However, the method proposed in this study provides a physically-correct idea to establish a general prediction of the frictional resistance as well as the form factor.

## 5.5. Case Study of Viscous Resistance in Extremely Shallow Water

In the previous sections, studies have been conducted to improve the prediction of the frictional resistance and the form factor when  $h/T$  is 1.2 or more. The existing studies also not considered the case of extremely shallow water. In the researches of Schlichting (1934) and Lackenby (1963),  $h/T$  is always larger than 1.3. The method of Jiang (2001) applies only for  $h/T \geq 1.5$ . The study of Raven (2012) investigated lower values of  $h/T$ , but

the number is still above 1.2. It is noteworthy that  $h/T < 1.2$ , which can be seen as extremely shallow water, is also commonly found in the existing waterways, especially for tributaries and canals (Eloot and Vantorre, 2011). Ships sailing at  $h/T < 1.2$  may have a risk of grounding but also can carry more cargo or containers. It would be valuable to gain an insight into the physical phenomenon in extremely shallow water and its effects on ship resistance to evaluate the feasibility of extremely-shallow-water navigation.

In this section, a case study of how the viscous part of ship's resistance changes in extremely shallow water are introduced. As the area of ship's flat bottom plays an essential role, another standard ship, KVCLL2 ( $C_B = 0.81$ ), which has a larger proportion of flat bottom than the KCS and excludes the effects of the transom, was selected to more explicitly illustrate the flow mechanism in extremely shallow water. The Wigley hull was also used for comparison.

It will show that for a ship with a high block coefficient, the frictional resistance becomes smaller when the water is shallower due to the strong interactions between the boundary layers formed on the ship bottom and waterway bottom. The form effects are also enlarged, leading to the result that the viscous pressure resistance can be even larger than the frictional resistance in extremely shallow water.

5

### 5.5.1. Case Setup

A 1/58 model of the KVLCC2 is used in the tests of Kim et al. (2001). To enable possible comparisons, a numerical model with the same size was built. The underwater part of the sections of the KVLCC2 is depicted in Figure 5.24 together with the Wigley hull.

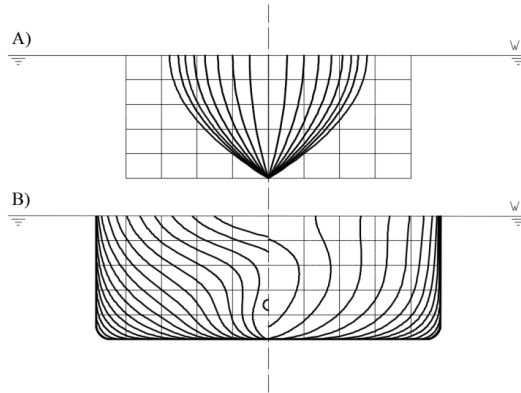


Figure 5.24: The sections of A) the Wigley hull, B) the KVLCC2

Double-body computations are used to calculate the viscous resistance. A commercial CFD code, Ansys Fluent (version 18.1), is again applied and numerical settings are the same as Section 5.2.3. The Reynolds numbers

spread from  $\lg(Re) = 5.8$  to  $\lg(Re) = 9.2$ , as shown in Table 5.9. Four water depths are chosen (Table 5.10), where the cases with  $h/T = 1.1$  and  $h/T = 1.05$  are both extremely shallow water scenarios. The deep water case and the case with  $h/T = 1.2$  are used for comparison.

Table 5.9: The Reynolds number ( $Re$ ) chosen in this study

No.	1	2	3	4	5	6	7	8	9	10	11	12
$\lg(Re)$	5.8	6.0	6.2	6.4	6.6	6.8	7.2	7.6	8.0	8.4	8.8	9.2

Table 5.10: The selected water depths

No.	$h/T$
1	15.0 (deep)
2	1.2
3	1.1
4	1.05

### 5.5.2. Results and Discussion

In Section 5.4.1, it was found that for all three ships, smaller water depth will lead to a higher frictional resistance when  $h/T \geq 1.2$ . However, this argument may not apply in extremely shallow water  $h/T < 1.2$ . The results of the frictional resistance coefficient ( $C_f$ ) of the Wigley hull and the KVLCC2 are shown in Figure 5.25.

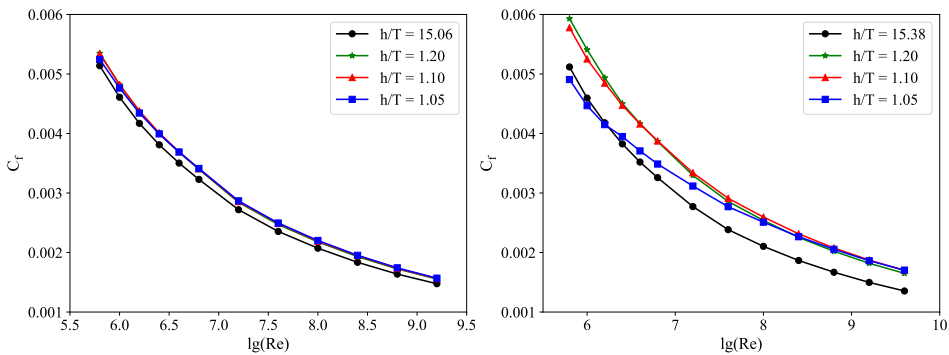


Figure 5.25: The frictional resistance coefficient ( $C_f$ ) of the Wigley hull (left) and the KVLCC2 (right)

Based on Figure 5.25:

- Although  $C_f$  of the KVLCC2 and the Wigley are similar at deep water

case ( $h/T \approx 15$ ), the KVLCC2 has much larger  $C_f$  when  $h/T = 1.2$  and  $1.1$ , which indicates the dependency of  $C_f$  on the fullness of the hull lines;

- For the KVLCC2 when  $\lg(Re) < 6.5$ ,  $C_f$  at  $h/T = 1.1$  is slightly smaller than that at  $h/T = 1.2$ ; for  $\lg(Re) < 8.0$ ,  $C_f$  at  $h/T = 1.05$  is significantly lower than  $h/T = 1.2$ , and even lower than the deep water case for  $\lg(Re) < 6.4$ . This phenomenon is counterintuitive and will be explained later;
- For the Wigley hull,  $C_f$  at  $h/T = 1.1$  is always slightly larger than  $h/T = 1.2$  (this may not be easily observed in the figure but it is true according to the data). For  $\lg(Re) < 6.5$ , a slight drop of  $C_f$  can be observed for  $h/T = 1.05$ .

In contrast to the counterintuitive changes of  $C_f$  in extremely shallow water, the viscous pressure resistance increases, as expected, with a decreasing  $h/T$ . The coefficient of the viscous pressure resistance ( $C_{vp}$ ) is shown in Figure 5.26.

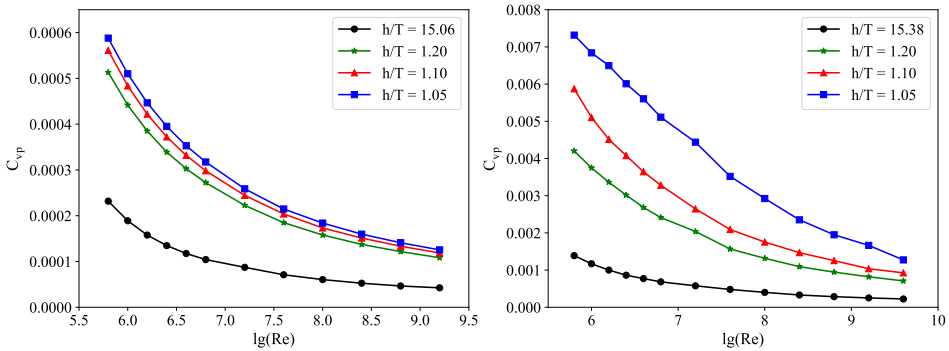


Figure 5.26: The coefficient of the viscous pressure resistance ( $C_{vp}$ ) of the Wigley hull (left) and the KVLCC2 (right)

Based on Figure 5.26, some remarks can be made for  $C_{vp}$ :

- For the Wigley hull at  $h/T = 1.05$ ,  $C_{vp}$  for different Reynolds numbers increases by roughly a factor of three compared to the value in deep water ( $h/T = 15.06$ ). However, the values of  $C_{vp}$  are still about 10% of the values of  $C_f$ ;
- For the KVLCC2, the increase of  $C_{vp}$  is more significant than the Wigley hull. For  $h/T \leq 1.2$ ,  $C_{vp}$  increases by three to seven times compared to deep water. For  $h/T = 1.05$ ,  $C_{vp}$  is at the same level of magnitude as or even higher than  $C_f$ .

In Figure 5.25,  $C_f$  of the KVLCC2 at  $h/T = 1.05$  is even lower than the deep water case for  $\lg(Re) < 6.4$ . This counterintuitive result is caused by

the extremely restricted under-keel space. Different from 2D cases, a large part of the flow will go sideways if the vertical direction is restricted, as shown in Figure 5.27. As a result of this, the flow beside the hull will be accelerated further, and a larger area of overspeed flow can be observed compared to the deep water case, which can be seen in the top view of the velocity field shown in Figure 5.28.

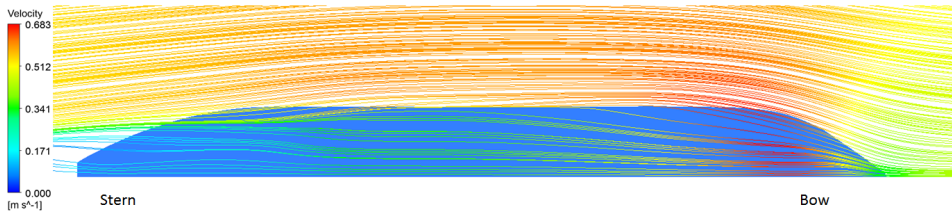


Figure 5.27: Streamlines under the bottom of KVLCC2 (bottom view; streamlines at the plane  $-0.025T$  away from ship bottom plane;  $h/T = 1.05$  and  $\lg(Re) = 6.4$ )

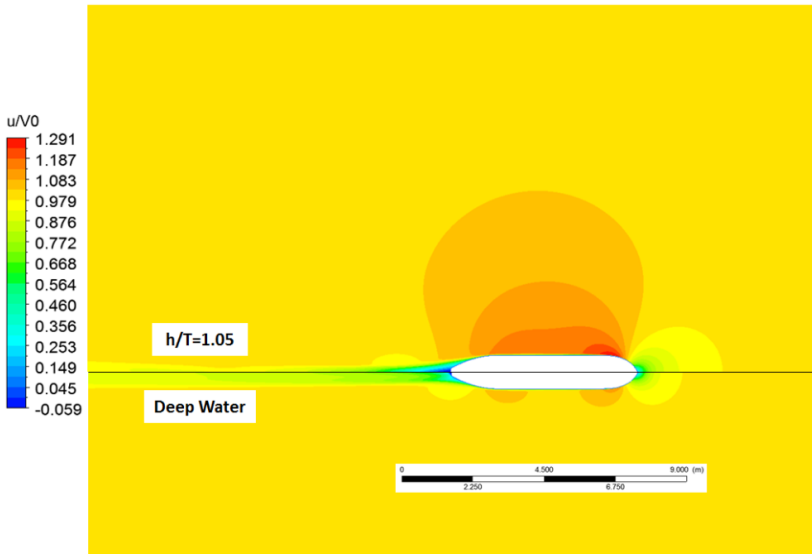


Figure 5.28: Velocity distribution on the plane  $z = T$  around the 1/58 KVLCC2 (top:  $h/T = 1.05$ ; bottom: deep water;  $\lg(Re) = 6.4$ ;  $u$ : flow velocity at  $x$  direction;  $V_0$ : the velocity of the incoming flow)

In the meantime, a different shape of the ship will lead to a different distribution of shear stress on the hull, as shown in Figure 5.29. Compared to the Wigley hull at  $h/T = 1.05$ , a negative gradient of shear stress at  $x$  direction is formed on the flat bottom of the KVLCC2, by which a smaller  $C_f$  was caused. In this case, the water at the stern of the KVLCC2 is less likely to recover to its speed before reaching the bow. According to the Bernoulli equation, a larger discrepancy in the velocity will cause a more significant

difference of the pressure between the bow and stern, leading to a higher viscous pressure resistance. This implies that the KVLCC2 is, therefore, more sensitive to water depth.

When the under-keel space is highly restricted, the boundary layer on the ship's bottom cannot develop freely. As depicted in Figure 5.30, where the velocity distribution on the midsection is shown, the development of the boundary layer on the ship's bottom is highly limited for KVLCC2 compared to the Wigley hull. The boundary layer on the bottom of the KVLCC2 is highly compressed and the flow velocity in the under-keel space decreases significantly leading to a friction loss on the ship's bottom. Owing to a large flat bottom of the KVLCC2, such friction loss can lead to a decrease of the total frictional resistance in extremely shallow water.

An example at  $\lg(Re) = 5.8$  is shown for a clear explanation. In this example, the shear force at  $x$  direction on three places: the flat bottom, the side parallel surface of the hull, and other surfaces of the KVLCC2 are compared in different water depths. The corresponding surface area of each place is shown in Table 5.11.

Table 5.11: The area of the flat bottom, the side parallel surface of the hull, and the total surface of the 1/58 scaled KVLCC2

	Area(m <sup>2</sup> )	Percentage
Bottom	1.796	43.6%
Side	1.010	24.5%
Others	1.310	31.8%
Total	4.116	100.0%

The results of shear force (friction) on each surface with different water depth are shown in Figure 5.31 and its percentage are visualized in Figure 5.32.

Based on Figure 5.31 and 5.32, it can be derived that for  $\lg(Re) = 5.8$ :

- Compared with deep water ( $h/T = 15.38$ ), the percentage of the friction on the flat bottom increases at  $h/T = 1.2$ , but decreased when  $h/T < 1.2$ . At  $h/T = 1.05$ , the number (41.8%) is even less compared to deep water (43.7%);
- The shear force on the flat bottom takes about half of the total friction. For  $h/T < 1.2$ , changes of the shear force on the flat bottom dominate the changes of the total friction;
- The friction on the parallel surface and other surface is much less sensitive to the water depth.

According to one's intuition, larger friction is expected if the water is shallower. However, based on this section, this is only correct for ships at full scale and slender ships, such as the Wigley hull, at model scale.

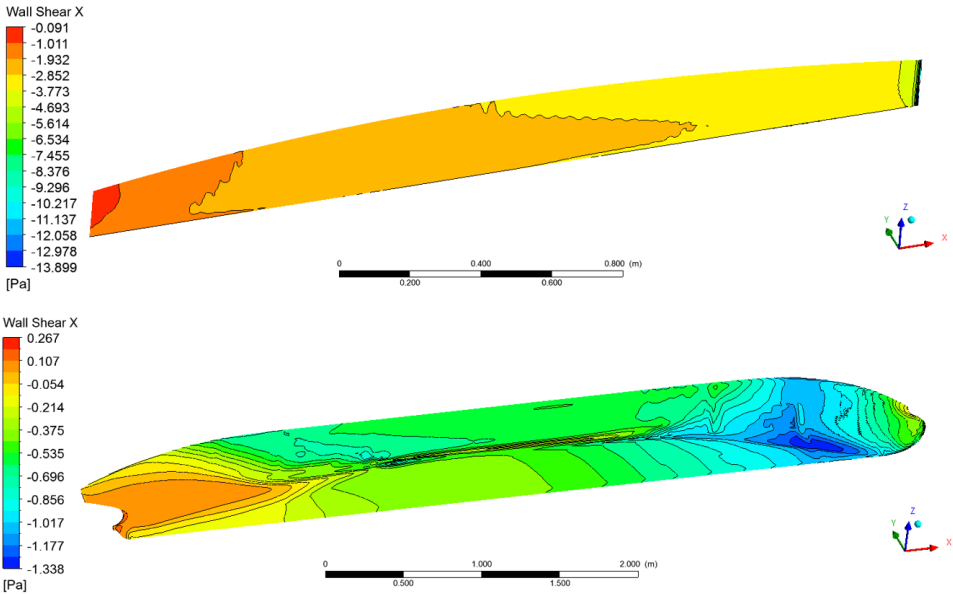


Figure 5.29: Distribution of wall shear at x direction for the Wigley hull (top) and the 1/58 KVLCC2 (bottom) at  $\lg(Re) = 6.4$  and  $h/T = 1.05$

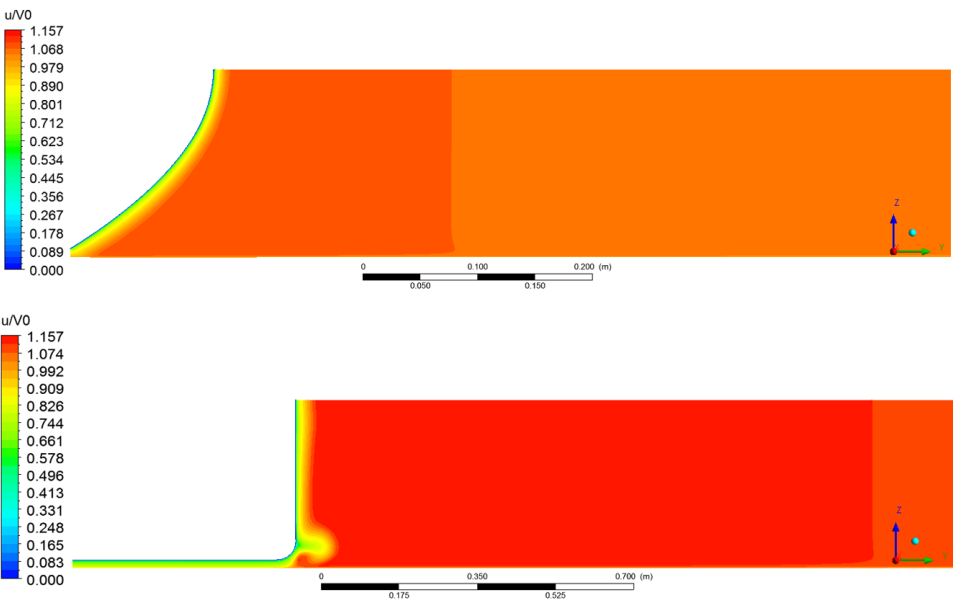


Figure 5.30: The velocity distribution on the midsection of the Wigley hull (top) and the 1/58 KVLCC2 (bottom) at  $\lg(Re) = 6.4$  and  $h/T = 1.05$

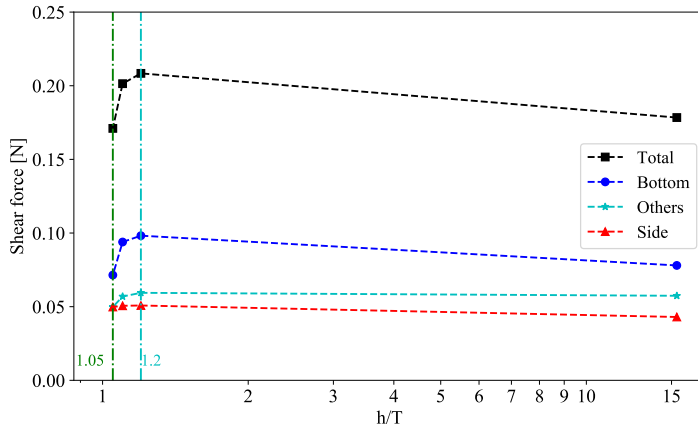


Figure 5.31: The shear force at x direction on the flat bottom, the side parallel surface, and the total surface of the 1/58 scaled KVLCC2 ( $\lg(Re) = 5.8$ )

5

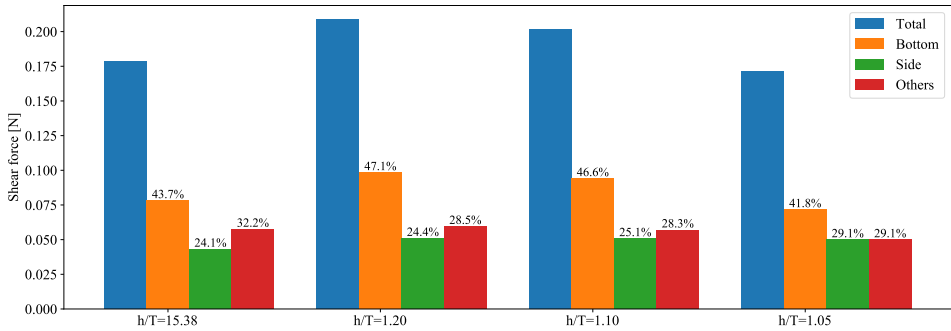


Figure 5.32: The shear force (N) and its percentage with different  $h/T$  on the flat bottom, the side parallel surface of the hull, and the total surface of the 1/58 scaled KVLCC2

Flow separation is found at the stern of the KVLCC2. Vortices caused by the separation can even provide thrust locally, as the positive shear stress at the stern shown in Figure 5.29. This thrust will also cause a decrease of  $C_f$ . However, the influence of the separation occurs at the stern only, which is local and minor compared to the changes on the ship bottom (see Figure 5.31).

The point when the friction starts to decrease with the water depth can be predicted by comparing the ship's boundary layer in deep water with the under-keel clearance ( $UKC$ ) in shallow water cases. As shown in Figure 5.33, the ratio between the boundary layer thickness ( $\delta_{0.99}$ ) and ship's draft is depicted for various Reynolds numbers in deep water.  $UKC$  of  $h/T = 1.10$  and  $h/T = 1.05$  are also shown in this figure.  $\delta_{0.99}$  is measured at  $x = 0.25 L_{pp}$  (the origin is at the aft perpendicular) on the ship bottom.

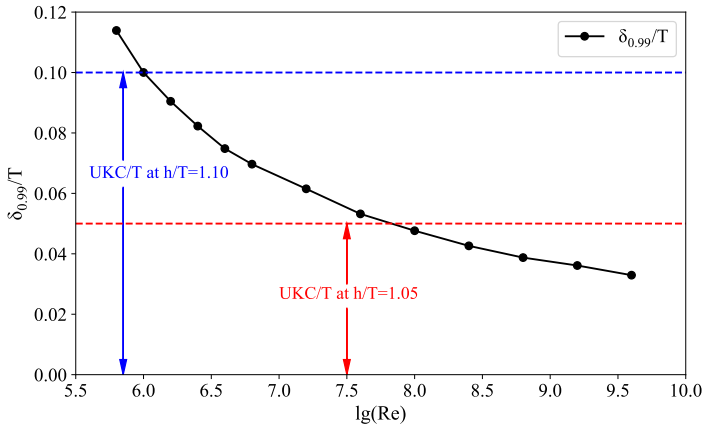


Figure 5.33: The ratio of bottom boundary layer thickness to KVLCC2's draft ( $\delta_{0.99}/T$ ) at  $x = 0.25 L_{pp}$  against Reynolds numbers in deep water and compared to *UKC* in extremely shallow water

It can be derived from Figure 5.33 that

- A thinner boundary layer is observed for a higher Reynolds number ( $Re$ ). When  $\lg(Re) > 8.5$  (full scale),  $C_f$  is hardly affected by water depth due to a thin enough boundary layer, even in extremely shallow water;
- For  $h/T = 1.1$ , the under-keel clearance (*UKC*) is  $0.1 T$ , which is at the same order of magnitude as the boundary layer thickness at  $\lg(Re) = 6.0$ . According to Figure 5.25, shallow water effects can spread up to  $\lg(Re) = 6.5$ ;
- Similarly, for  $h/T = 1.05$ , *UKC* is  $0.05 T$  which is similar to  $\delta_{0.99}$  at  $\lg(Re) = 7.8$ , but according to Figure 5.25, the shallow water effects can be observed until  $\lg(Re) = 8.5$ .

As mentioned before, the changes in ship's frictional resistance depend on whether or not the boundary layer can develop freely (ship boundary layer can develop freely in deep water). The Wigley hull is slender enough and provides enough space for the development of the boundary layer, but it is not the case for the KVLCC2.

### 5.5.3. Supplementary Notes

- The 3D flow around a ship hull in extremely shallow water ( $h/T < 1.2$ ) is so complex that it cannot be simplified into a 2D flow over a flat plate. The basic rule that how the viscous resistance changes with water depth and Reynolds number should be investigated separately from that in deep and intermediate shallow waters.

- If the free surface is considered, the ship-generated wave system can impact the results of  $C_f$ . The trough of the bow wave system, which is a primary wave system, lowers the water level close to the bow. This leads to shallower water and therefore a higher local  $C_f$ . The crest of the bow wave system can raise the water level and plays an opposite role to the trough. However, the influence is limited to a small area at the bow and makes little difference to the total  $C_f$ . The crests and troughs of the secondary wave system along the hull can compensate each other and will also make little contribution to  $C_f$ .
- Inland waterways usually have lateral restrictions. In extremely shallow water, the critical velocity in a confined condition is easier to be reached compared to intermediate shallow waters. In this case, indicating the critical speed in confined conditions instead of the open shallow water will be more applicable to choose an appropriate speed.

## 5

## 5.6. Concluding Remarks

In this chapter, the viscous part of the resistance of a ship sailing in shallow water was studied. Comparisons between a 2D flat plate and three ship forms are made to illustrate the effects of a curved surface on the viscous resistance in deep water. Comparisons of a specific ship in varied vertically-restricted waters are made to show the influence of water depth. Comparisons among the Wigley hull, the KCS, and the Rhine Ship 86 are made to demonstrate how ship forms play a role on the viscous resistance in shallow water.

Based on the results and analyses of  $h/T \geq 1.2$ , several conclusions can be drawn:

- In contradiction with traditional assumptions based on ships sailing in deep water, the frictional resistance depends on both hull form and water depth in shallow water. A general formula to predict ship's friction in shallow water can be built, with some constants in the expression determined per ship form;
- The viscous pressure resistance is affected by both the hull form and the water depth. A definition of the form factor based on the computed frictional resistance instead of the flat plate friction line is proposed to ensure a stronger physical basis. Empirical correlation line for the form factor of three ships are built considering the effects of both ship scale and water depth;
- For both model scale and full scale, the viscous part of resistance predicted by the conventional approach without shallow water corrections has up to 10% error for slender ships like the Wigley hull and up to 30% for fuller ships, such as the KCS and the Rhine Ship 86.

In the case study of the ship's viscous resistance in extremely shallow water ( $h/T < 1.2$ ), the effects on both  $C_f$  and  $C_{vp}$  are demonstrated and compared with the results in deep and intermediate shallow water. Several conclusions can be derived:

- Against to one's intuition, when  $h/T < 1.2$  and at a relatively low Reynolds number, the friction of a highly-curved ship (such as the KVLCC2) is decreasing with decreasing water depth. These changes usually occur on the model scale of ships;
- For slender ships like the Wigley hull, in contrast to the KVLCC2, only slight effects on both the frictional resistance and the viscous pressure resistance can be observed when  $h/T < 1.2$ ;
- For the KVLCC2, the increase of the viscous pressure resistance is more significant than that of the Wigley hull. For  $h/T \leq 1.2$ , the increasing  $C_{vp}$  caused by shallow water effects is at the same level or even larger than  $C_f$ ;
- Evaluating whether the boundary layer can develop freely is the key to estimate the trend of changes of  $C_f$  in shallow water;
- The prediction of ship's viscous resistance in extremely shallow water should be considered specifically and separately. Additional corrections need to be applied once the boundary layer thickness reaches the under-keel clearance at model scale. Both the geometry and the Reynolds number should be considered if a new prediction method is built.

With the analysis of shallow water effects on the viscous part of ship resistance, this chapter adds some information into the understanding of the physics of ship resistance in shallow water which expects to improve the prediction of ship's resistance in shallow water.



# 6

## Shallow Water Effects on Ship-generated Waves

The previous chapters have addressed the shallow water effects on the viscous part of ship resistance. Among the three main components, the wave-making resistance will have the smallest impact on the total resistance since most ships sail at a low speed in shallow water. However, wave-making resistance is not ignorable and understanding shallow water effects on wave-making resistance can make the prediction of ship's total resistance in shallow water complete. Since wave-making resistance strongly relates to ship-generated waves, a study of shallow water effects on the characteristics of ship-generated waves contributes to understand how wave-making resistance changes in shallow water.

The existing methods to determine wave-making resistance, such as the potential theory, are mostly derived from the inviscid flow. They cannot cope with the effects of viscosity, which plays an essential role in wave-making resistance in shallow water. In this chapter, the changes in the height and length of ship-generated waves in shallow water are studied based on CFD computations. Also, the effects of waterbed friction and the scale effects on wave-making resistance are discussed. Although displacement vessels do not navigate in critical or supercritical speed regions, CFD computations in this chapter force the Wigley hull to enter those speed regions to provide a complete demonstration for the properties of ship-generated waves in shallow water.

---

This chapter (except Section 6.5) is based on the paper:

Qingsong Zeng, Cornel Thill, Robert Hekkenberg, 2019. Shallow water effects on ship-generated waves, 5th International Conference on Ship Manoeuvring in Shallow and Confined Water (MASHCON), Ostend, Belgium. ([Zeng et al., 2019c](#)).

## 6.1. Introduction

In the existing theories to determine wave-making resistance, a well-known method is the wave-pattern analysis, which is based on the relation between wave energy and wave pattern (Eggers et al., 1967; Havelock, 1932; Michell, 1898). With the assistance of the velocity potential, the velocity field and pressure field can be solved both analytically and numerically (Raven, 1996). However, wave-pattern analysis does not always provide plausible results, and the wave-making resistance obtained by linearized wave-pattern analysis is usually larger than the values obtained by measurements (Insel and Doctors, 1995; Sharma, 1963). The gap between the analyzed wave-pattern resistance and the obtained wave-making resistance from experiments is even bigger in shallow water (Thill, 1991).

In shallow water, wave-pattern analysis is influenced by the variations of wave properties caused by limited water depth. For small amplitude waves in deep water, the movements of water particles are linear and harmonic, and the trajectory is circular with its amplitude damping exponentially to the water depth (Airy, 1841). However, when the water is sufficiently shallow, the oscillating movements adjacent to the bottom will be affected by the bottom friction. An oscillatory boundary layer (Stokes boundary layer) is formed above the bottom, and a part of wave energy is dissipated in the boundary layer (Schlichting, 1979).

According to the existing studies, shallow water effects were observed for the characteristics of waves, e.g., the height (Putnam and Johson, 1949), the velocity (Lamb, 1932) and the length (McSullea et al., 2018) of the waves. Therefore, the mechanism of wave propagation becomes different in shallow water, and the theory used to describe shallow water waves should, therefore, not be limited to the linear wave theory. According to Chakrabarti (1987), several wave theories are available and can be applied in shallow water.

Additionally, the method of resistance extrapolation in model tests will be influenced if the viscosity, e.g., effects of bottom friction on waves (Jons-son, 1967), is considered. In model tests, a pervasive assumption is that the coefficient of wave resistance coefficient is solely a function of the Froude number and stays the same for full-scale ships and its geometrically similar models (ITTC, 2017j). As the full-scale Reynolds number and the Froude number cannot be achieved simultaneously in model tests, it is conventional to keep the Froude numbers identical during model tests on ship resistance. However, for certain ship forms, the Reynolds number dependency of the wave-making resistance becomes noticeable, which can lead to a reconsideration of the resistance extrapolation.

## 6.2. Method

This section introduces three waves theories, both linear and nonlinear. They will be used for further analysis of wave profiles in Section 6.3 and

bottom friction in Section 6.4. Afterward, the commercial CFD code by which the main results are generated is verified and validated for ship wave computation.

### 6.2.1. Linear and Non-linear Wave Theories

The well-known Airy wave theory (Airy, 1841), a cnoidal wave theory (Benjamin et al., 1972), and the Stokes second-order wave theory (Stokes, 1847) are introduced in sequence. The expressions of the governing equations, wave elevation, and bottom oscillating velocity, which will be used, are presented.

#### Airy wave theory

The Airy wave theory, or the so-called linear wave theory, assumes small-amplitude waves and inviscid fluid. With the concept of the velocity potential ( $\phi$ ), the kinematic and dynamic conditions on the free surface can be derived:

$$\frac{\partial \eta}{\partial t} - w = 0, \quad (6.1)$$

$$\frac{\partial \phi}{\partial t} + g\eta = 0, \quad (6.2)$$

where  $\eta$  is the free surface elevation,  $w$  the velocity at the vertical direction,  $t$  the time and  $g$  the acceleration of gravity. The solution of wave elevation and velocity potential can be given as

$$\eta(x, t) = a \cos(kx - \omega t), \quad (6.3)$$

$$\phi(x, z, t) = \frac{a\omega}{k} \cdot \frac{\cosh[k(z+h)]}{\sinh(kh)} \cdot \sin(kx - \omega t), \quad (6.4)$$

where  $a$  is the wave amplitude,  $k$  the wave number,  $\omega$  the wave frequency, and  $h$  the water depth. Based on the linear wave theory, the velocity of water particles at the bottom ( $V_h$ ) is derived as follows:

$$V_h = \frac{a\omega}{\sinh(kh)} \cos(kx - \omega t). \quad (6.5)$$

For certain large  $a/h$  ratios, where the water is sufficiently shallow, the horizontal velocity (equation (6.5)) will not decay to zero on water floor. As the applied potential approach cannot cope with friction, a correction dealing with the physical boundary condition at the bottom, see Figure 2.4, is not possible. However, equation (6.5) can be applied to estimate the energy dissipation in the oscillating boundary layer on the water bottom.

### BBM wave theory (cnoidal wave)

For some relatively large amplitude waves in shallow water, the terms of the velocity and elevation derivatives on the free surface are no longer negligible. Therefore, the boundary conditions become

$$\frac{\partial \eta}{\partial t} + u \frac{\partial \eta}{\partial x} - w = 0, \quad (6.6)$$

$$\frac{\partial \phi}{\partial t} + \frac{1}{2}(u^2 + w^2) + g\eta = 0. \quad (6.7)$$

Then Boussinesq equations (Boussinesq, 1872) can be derived:

$$\frac{\partial^2 \eta}{\partial t^2} = gh \frac{\partial^2 \eta}{\partial x^2} + gh \frac{\partial^2}{\partial x^2} \left( \frac{3}{2} \frac{\eta^2}{h} + \frac{h^2}{3} \frac{\partial^2 \eta}{\partial x^2} \right), \quad (6.8)$$

where the symbols have the same meaning as in the linear theory. Cnoidal wave theory was built when solving the equations (6.6) to (6.8): with some additional assumptions (more details are omitted), the Korteweg and De Vries (1895) equation (KdV equation) and Benjamin et al. (1972) equation (BBM equation) were derived for unidirectional waves in shallow water.

As the BBM equation, or is also called the regularized long wave (RLW), is assumed to be more appropriate to describe long waves in nonlinear dispersive systems than KdV equation (Benjamin et al., 1972), the BBM wave is selected as a representative of cnoidal waves. Based on the assumption that the wave profile is permanent, i.e., independent of time, Dingemans (1997) provided the periodic solution for the BBM equation:

$$\eta(x, t) = -a_t + H \operatorname{cn}^2 \left( 2K(m) \frac{x - ct}{\lambda} \middle| m \right), \quad (6.9)$$

where

$$\begin{aligned} \lambda &= \sqrt{\frac{16h^3}{3H} m \frac{c}{\sqrt{gh}}} \cdot K(m), \\ a_t &= H - a_c, \quad a_c = \frac{H}{m} \left( 1 - \frac{E}{K} \right), \\ c &= \left[ 1 - \frac{1}{2} \frac{H}{h} + \frac{1}{m} \frac{H}{h} \left( 1 - \frac{3}{2} \frac{E}{K} \right) \right] \sqrt{gh}, \end{aligned}$$

where  $a_c$  and  $a_t$  are absolute values that the crest and the trough deviate the mean water level,  $H$  is the wave height,  $\lambda$  the wavelength, and  $c$  the wave speed.  $m$  is the elliptic parameter,  $K(m)$  is the complete elliptic integral of the first kind, and  $E(m)$  is the complete elliptic integral of the second kind. The velocity on the water bottom is demonstrated as

$$V_h = u + \frac{1}{6} \cdot \frac{d^2 u}{dx^2}, \quad (6.10)$$

where

$$u = \frac{c\eta}{h+\eta}.$$

Again, the velocity is not vanishing on the water bottom, since the BBM wave theory cannot cope with the Stokes boundary layer at the bottom.

### Stokes second-order wave theory

Higher orders of Stokes waves were first introduced by Stokes (1847) using perturbation theory to achieve practical solutions for non-linear waves. By considering a different number of terms in the Stokes expansion, different orders of Stokes waves can be obtained.

The most frequently used wave theories are from the second order to the fifth order, and this section briefly discusses the solution of the second order (2nd), which is more appropriate than other orders to describe ship-generated waves. According to the study of Dingemans (1994), the solution of the second-order Stokes wave on limited and even water depth is given:

$$\eta(x, t) = a \left[ \cos \theta + ka \frac{3 - \sigma^2}{4\sigma^3} \cos 2\theta \right], \quad (6.11)$$

$$\phi(x, z, t) = \frac{aw_0}{k \sinh(kh)} [\cosh [k(z+h)] \sin \theta + \frac{3ka}{8 \sinh 3(kh)} \cosh [2k(z+h)] \sin 2\theta], \quad (6.12)$$

where

$$\begin{aligned} \omega &= \omega_0 \left[ 1 + k^2 a^2 \frac{9 - 10\sigma^2 + 9\sigma^4}{16\sigma^4} \right], \\ \theta &= kx - \omega t, \\ \sigma &= \tanh(kh), \\ \omega_0^2 &= gk \cdot \tanh(kh). \end{aligned}$$

The symbols again have the same meaning as used in linear wave theory. The velocity on the water bottom of Stokes 2nd wave theory can be derived as

$$V_h = \frac{aw_0}{\sinh(kh)} \cdot \left[ \cos(kx) + \frac{3ka}{4\sinh^3(kh)} \cos(2kx) \right]. \quad (6.13)$$

Even for Stokes 2nd wave theory, a horizontal velocity exists at the bottom for certain  $a/h$  ratios, and the Stokes boundary condition at the bottom will be sacrificed. Expressions of the horizontal velocities of all three wave theories will be used for estimating the energy dissipation in the oscillating boundary layer.

The wave theories mentioned above are developed based on ideal flow, where the viscosity is zero. To include the influence of viscosity, Computational Fluid Dynamics (CFD) method is seen as a proper choice, which will be discussed in the following subsection.

### 6.2.2. Code Verification and Validation

In this chapter, the results of free surface elevation and ship resistance will be achieved again through a commercial solver: ANSYS<sup>(TM)</sup> Fluent (version 18.1). The Wigley hull, which has been used in Chapter 5, is applied to verify and validate the code in the computations considering the free surface. In the numerical calculations, the mesh type, the turbulence model, and the scheme of discretization are selected as the same as Chapter 5. The difference is the consideration of free surface, where the VOF (Volume of Fluid) method is applied.

#### Verification

To obtain an accurate and relatively high-resolution wave profile but with acceptable computing time, an appropriate number of grid points should be used within one wave height and one wavelength. In this chapter, the number of grid points per wave height is about 10, and the aspect ratio of the cells near the free surface is at the magnitude of 10. Such setting was proved to be suitable in the vertical direction, and a continued increase of the number of grid points in the wave height makes a minor contribution to the resolution (Javanmardi, 2015). Therefore, this study will focus on the choice of grid points per wavelength.

The linear wave theory is referred to during the selection of the number of grid points per wavelength. In the linear theory, the number of ship-generated waves along the hull ( $n$ ) is a function of Froude number ( $Fr$ ):

$$n = \frac{1}{2\pi Fr^2}. \quad (6.14)$$

Equation (6.14) makes it possible to estimate the wavelength ahead. In shallow water, it will be shown that the wavelength is longer compared to deep water, which means the number of grid points acceptable in deep water will be also enough in shallow water.

In Table 6.1, choices of the number of grid points per wavelength ( $N$ ) are shown. Numerical results of the coefficients of the ship's frictional resistance ( $C_f$ ) and total resistance ( $C_t$ ) are compared to reflect the effects of grid points on the force computation.

Table 6.1: The number of grid points per wavelength and the results of resistance for  $Fr = 0.316$  in deep water

Case	$N$	$C_f (\times 10^3)$	$C_t (\times 10^3)$
1	100	3.566	5.281
2	80	3.574	5.286
3	60	3.590	5.302
4	40	3.617	5.331
5	30	3.592	5.303
6	20	3.572	5.333

From Table 6.1, the differences of both  $C_f$  and  $C_t$  for each case are within 2%, which indicates that the number of grid points per wave has a minor influence on the results of resistance. However, a different conclusion has to be made for the accuracy of free surface elevation. As shown in Figure 6.1, a wave-cut at  $y = 2B$  (lateral direction) is depicted for each case in the range of  $x = -1.5L \sim 0.8L$  (longitudinal direction).

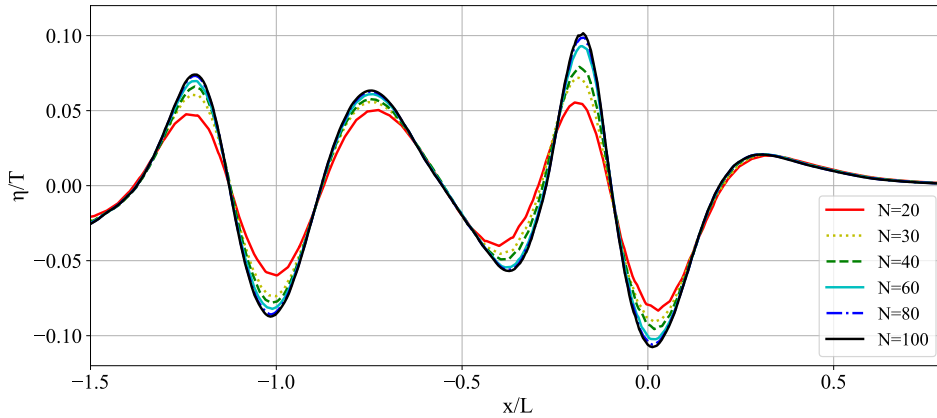


Figure 6.1: The wave cut at  $y = 2B$  for different cases in the range of  $x = -1.5L \sim 0.8L$  ( $Fr = 0.316$ ; the hull locates at  $x = -0.5L \sim 0.5L$  with the bow at  $0.5L$ )

Based on Figure 6.1:

- When  $N = 20$ , the calculation is not able to give a correct wave profile;
- In the range of  $N = 30 \sim 60$ , the accuracy or sharpness of wave profile increases with a refinement of the mesh, but the changes are becoming smaller when  $N$  is larger than 60, as an example shown in Figure 6.2;
- When  $N \geq 60$ , the refinement of the mesh only makes small contributions to the accuracy of wave profiles.

The purpose of this grid refinement study is to find a balance between accuracy and computing time. Therefore, an  $N \geq 30$  is guaranteed for all cases, and an  $N \geq 60$  is guaranteed in the area close to the ship hull.

The value of  $y^+$  is another factor which can play a role in the accuracy of ship resistance computation. In Chapter 5, the effects of  $y^+$  on the results of the frictional resistance have been studied without considering the effects of the free surface. In this chapter, the free surface will be included in the study of  $y^+$  dependency. Also, only the viscous sublayer and the log-law region were studied in Chapter 5 since a strong physical basis is available. In this chapter, the buffer layer and the out layer, where empirical methods are used, will be also studied, as shown in Table 6.2.

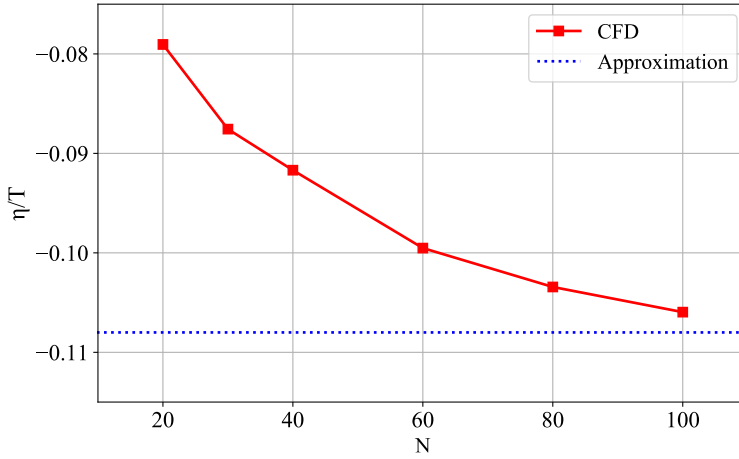


Figure 6.2: The wave height at  $x = 0L$  with the increase of grid points per wavelength (an asymptotic line can be predicted (dashed line) when  $N > 100$ )

6

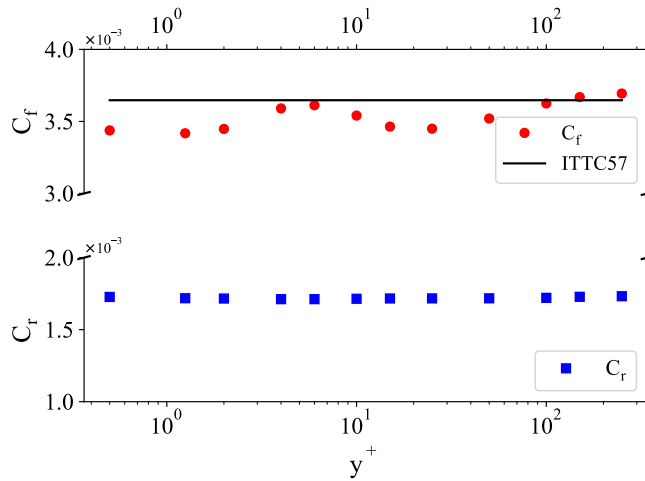


Figure 6.3: The friction coefficient  $C_f$  and the residual resistance coefficient  $C_r$  of a Wigley hull against  $y^+$  (deep water,  $Fr = 0.316$ ,  $\lg(Re) = 6.53$ )

The results of the frictional resistance coefficient ( $C_f$ ) and the residual resistance ( $C_r = C_t - C_f$ ) in deep water are demonstrated in Figure 6.3. The ITTC57 correlation line (ITTC, 1957) for ship friction is also shown for comparison.

From Figure 6.3, it can be seen that

Table 6.2: The selected  $y^+$  and the corresponding region in the boundary layer

No.	Location	$y^+$
1	viscous sublayer	0.5
2	viscous sublayer	1.25
3	viscous sublayer	2
4	viscous sublayer	4
5	buffer layer	6
6	buffer layer	10
7	buffer layer	15
8	buffer layer	25
9	log-law region	50
10	log-law region	100
11	log-law region	150
12	outer layer	250

- The values of  $C_f$  show wiggles with  $y^+$  and the largest deviation from the ITTC57 line is about 6%;
- When  $y^+ \approx 6$  and  $y^+ \approx 100$ , the numerical results of  $C_f$  have a satisfactory agreement with the ITTC57 line;
- The results of  $C_r$  are not sensitive to  $y^+$  (variations are less than 1%).

When comparing the results of  $y^+$  test in Chapter 5 (Figure 5.7), the influence of  $y^+$  on  $C_f$  is similar regardless of whether the free surface is considered. The wiggles of  $C_f$  are caused by different wall treatments based on the value of  $y^+$ , which is set within the selected  $\omega$ -equation applied in the code. A low-Reynolds number model is used in the viscous sublayer. The wall function approach is switched on in the logarithmic layer. In the buffer layer and the outer layer, blending methods are applied to ensure a reasonable result. It would be interesting to point out that the code provider claims “ $y^+$  insensitive”  $C_f$  (ANSYS, 2017a), but perceptible differences can be found based on Figure 6.3.

In practice, a value of  $C_f$  which coincides better with the ITTC57 line is assumed to be more accurate. Accordingly,  $y^+$  around 4 or 100 are preferred, and  $y^+ = 4$  is selected for most cases, and a value of 100 is selected for high  $Re$  cases based on the stability and cost of computations.

### Validation

The CFD results of free surface elevation along the Wigley hull in deep water ( $N = 60$  and  $y^+ = 4$ ) is validated by the experimental results of Kajitani et al. (1983), as shown in Figure 6.4.

In Table 6.3, The computing results of  $C_f$  are compared with the ITTC57 correlation line, and the total resistance coefficient ( $C_t$ ) is compared with the data of Kajitani et al. (1983).

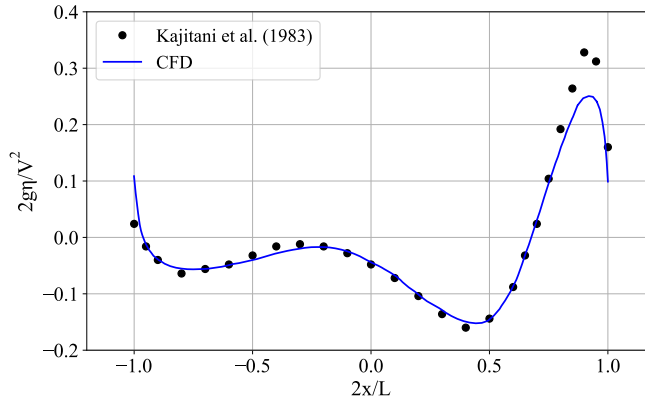


Figure 6.4: The validation of the free surface elevation along the Wigley hull (the bow is at  $2x/L = 1.0$ ;  $Fr = 0.316$ )

Table 6.3: Comparison of total resistance coefficient  $C_t$

$C_f$ -CFD ( $\times 10^{-3}$ )	$C_f$ -ITTC ( $\times 10^{-3}$ )	Error- $C_f$
3.590	3.647	-1.56%
$C_t$ -CFD( $\times 10^{-3}$ )	$C_t$ - Kajitani( $\times 10^{-3}$ )	Error- $C_t$
5.302	5.149	2.97%

Based on Figure 6.4 and Table 6.3, it can be derived that

- The CFD results of free surface elevation have a generally good agreement with experiments. Small differences are observed for the area close to the bow. It might be caused by a higher pressure gradient near the bow, and a finer mesh can help to improve the results close to the bow. However, this error is located in a small area, and its influence on the resistance is not significant;
- The differences of  $C_f$  compared to ITTC 57 line and  $C_t$  compared to the experiment are -1.56% and 2.97%, respectively, which are within a practically acceptable range.

In summary, the chosen code with the settings used in this study is able to generate acceptable results of both wave profile and results of ship resistance, and it will be used for the systematic calculations in the following sections.

### 6.3. Shallow Water Effects on Inviscid Ship Waves

When compared to deep water, ship waves develop less freely in shallow water. The wave properties, such as wave height and wavelength, are affected

by the limited water depth (Lamb, 1932). In this part, shallow water effects on the height and the superposition of ship-generated waves are discussed in inviscid water.

### 6.3.1. Wave Height

In Figure 6.5, the free surface elevations of the stern waves and the bow waves at the zero buttock plane ( $y = 0$ ) are shown for the Wigley hull sailing at the same speed but with various water depths. In Figure 6.5, the relation between  $h/T$  and  $Fr_h$  is shown in Table 6.4.

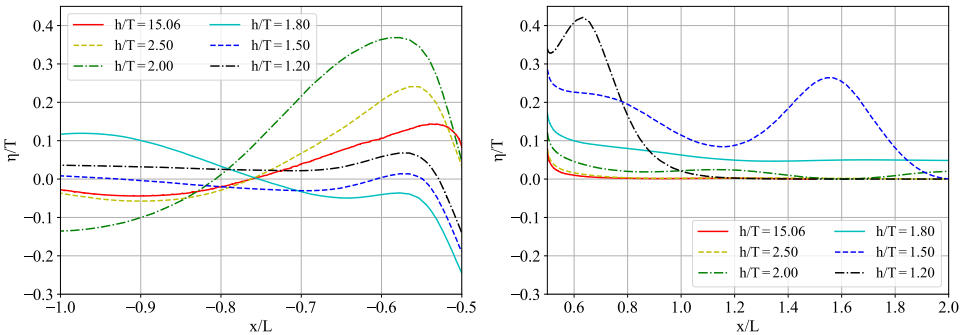


Figure 6.5: Stern waves (left) and bow waves (right) of a Wigley hull at various water depths ( $y = 0$ ;  $Fr = 0.316$ ; water comes from right to left; the bow is at  $x = 0.5L$  and stern is at  $x = -0.5L$ )

Table 6.4: Comparison table for applied  $h/T$  and  $Fr_h$

$h/T$	15.06	2.5	2.0	1.8	1.5	1.2
$Fr_h$	0.326	0.800	0.894	0.943	1.033	1.155

Some remarks can be made based on Figure 6.5:

- The height of the bow wave is larger when the water is shallower. Since a smaller under-keel clearance provides less space for the water to pass, more kinetic energy of the water will be transferred into wave’s potential energy resulting in higher bow waves;
- The changes are different for the stern waves. When  $h/T \geq 2.0$ , the height of the stern wave is increasing with decreasing water depth. However, when  $h/T \leq 1.8$ , the height drops immediately and then continue increasing with a decreasing water depth. The corresponding  $Fr_h$  of this turning point is about 1.0 (see Table 6.4).

The alternation of the wave height will influence the pressure distribution at the bow and the stern. The pressure resistance, both the viscous pressure resistance and the wave resistance, will be influenced accordingly.

### 6.3.2. Wavelength and Wave Superposition

Another property of ship-generated waves affected by water depth is wavelength. The linear wave theory is firstly applied to check its feasibility in shallow water. In linear wave theory, the phase velocity ( $c$ ) can be written analytically as

$$c = \sqrt{\frac{g\lambda}{2\pi} \tanh\left(\frac{2\pi h}{\lambda}\right)}, \quad (6.15)$$

where  $\lambda$  is the wavelength, and  $h$  is the water depth. For well-developed waves generated by a ship, the phase speed of the water is equivalent to the ship's velocity, which means that the phase speed of ship-generated waves stays the same for both deep and shallow water. Based on this, A relation of wavelength in deep and shallow water can be achieved as follows:

$$\frac{\lambda_s}{\lambda_d} = 1/\tanh\left(\frac{2\pi h_s}{\lambda_s}\right), \quad (6.16)$$

where the subscripts  $s$  and  $d$  indicate shallow and deep water, respectively. Linear theory can provide an acceptable description of wavelength in deep water but is not accurate enough when the water is shallow enough. As the comparison shown in Figure 6.6 at  $Fr = 0.316$ .

From Figure 6.6, it can be seen:

- Based on the linear theory, shallow water effects on wavelength are negligible when  $\lambda_s/h_s \leq 3$ , and the increase of wavelength in shallow water is approximately linear to  $\lambda_s/h_s$  when  $\lambda_s/h_s > 3$ ;
- The linear wave theory does not apply when for  $h/T \leq 2.0$ , where the wavelength is clearly underestimated compared to the CFD results.

To explicitly show the changes of wavelength in shallow water, numerical results of the wave profile behind the stern of the Wigley hull are demonstrated in Figure 6.7.

When  $h/T > 2.0$  (Figure 6.7 left), of which  $Fr_h < 1.0$ , the wavelength increases slightly but it becomes severe when  $h/T < 2.0$  (Figure 6.7 right). This change is non-linear and cannot be explained by the linear wave theory. For  $h/T = 1.2$  ( $Fr_h \approx 1.15$ ), the wavelength is over three times as long as the ship length. It can be derived that when the water is shallow enough, the length of the wave will become infinite and can explain the disappearance of the transverse wave system in the critical speed range.

The changes of wavelength will influence the wave superposition behind the stern. For shallow water, the waves generated at the bow will arrive earlier at the stern, but a crest is always generated at the aft. The depth of water then can determine how the bow and stern wave systems interact. Consequently, the optimal destructive wave interference that stands for

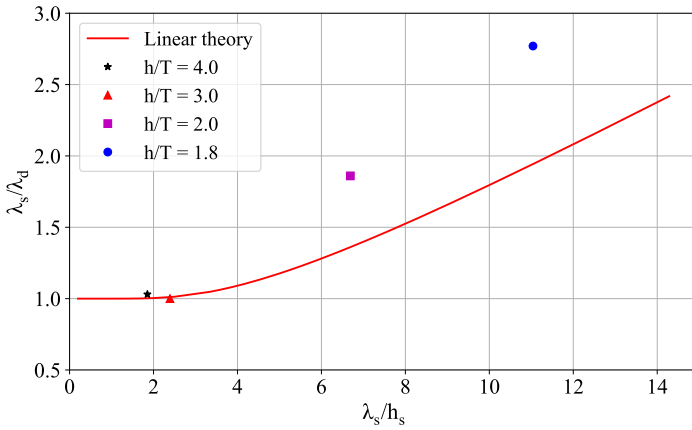


Figure 6.6: The ratio of wavelengths in shallow and deep water ( $\lambda_s/\lambda_d$ ) against the ratio of wavelength and water depth ( $\lambda_s/h_s$ ) based on linear wave theory compared with some CFD results in shallow water

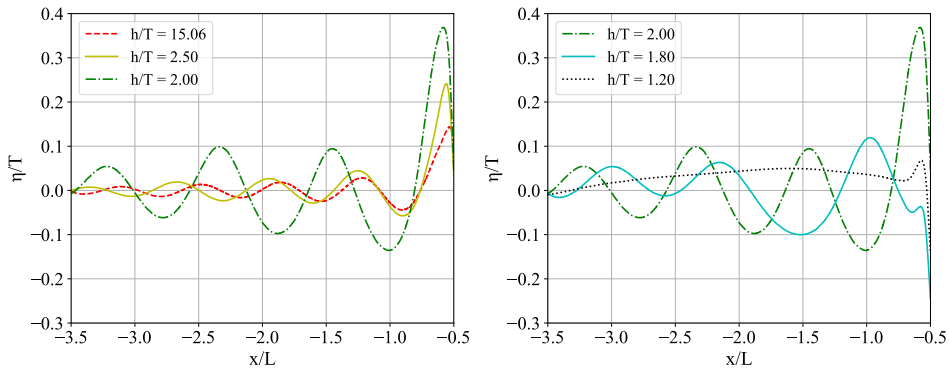


Figure 6.7: The wave profile after the stern of a Wigley hull ( $y = 0$ ;  $Fr = 0.316$ ; waters comes from right to left; the end of the stern is at  $x = -0.5L$ ; left:  $h/T = 15.06, 2.50,$  and  $2.00$ ; right:  $h/T = 2.00, 1.80,$  and  $1.20$ )

a good design in deep water can be inappropriate for other certain water depths.

An example is given in Figure 6.8, in which the same velocity but different water depths are applied. It can be seen that the second crest of the bow wave system moves further aft for shallower water, which will surely superimpose differently with the waves generated by the stern.

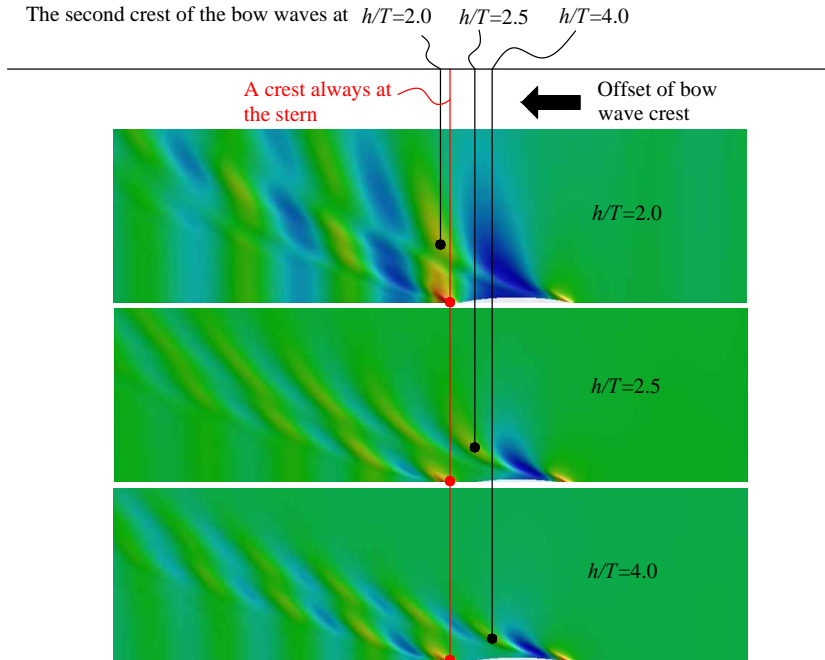


Figure 6.8: The wave pattern of a Wigley hull with various water depths ( $Fr = 0.316$ )

## 6.4. Effects of Viscosity on Ship Waves

In the previous section, the properties of ship waves in inviscid shallow water already show significant differences from deep water. If the viscosity is considered, wave profiles will be affected further, and the bottom friction of the waterway begins to play a role. In this section, the effects of viscosity on ship waves are studied, followed by a discussion of the influence of bottom friction on ship wave resistance.

### 6.4.1. Effects of Viscosity on Wave Height

The viscosity of water acts as damping for ship-generated waves. Part of the energy that the wave contains will be dissipated due to the shear stress between water particles. Such dissipation will be accumulated with the propagation of waves, and the movements of water particles will, therefore, be influenced especially behind the ship. In Figure 6.9, wave profiles of the Wigley hull in inviscid flow and viscous flow are compared. When  $Fr_h = 0.63$ , the wave profiles are highly overlapping for  $x \geq -L$ , which means for this case, the influence of viscosity is not significant close to the ship hull. However, for the range  $x < -L$ , the wave height in viscous flow is lower compared to inviscid flow.

Nevertheless, if the ship sails at a very high speed, where the wave resis-

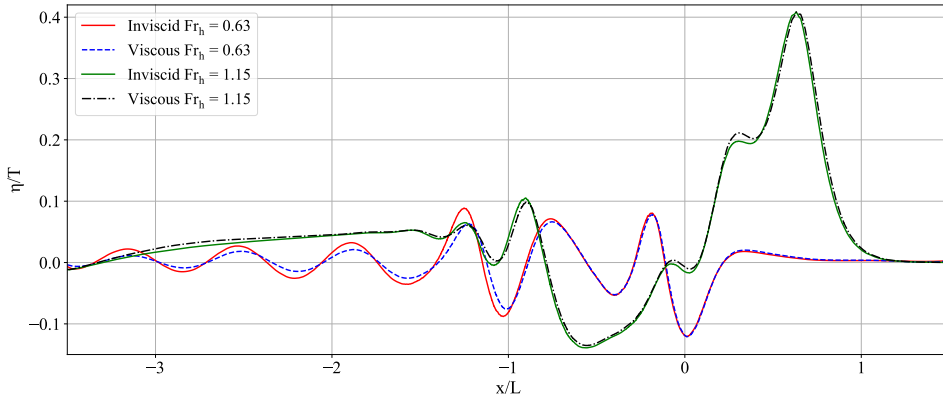


Figure 6.9: Comparison of longitudinal wave cuts of a Wigley hull in inviscid flow and viscous flow (wave cut at  $y = 2B$ ; the stern is at  $x = -0.5L$  and the bow is at  $x = 0.5L$ )

tance dominates the total resistance, the effects of viscosity are too small to be considered, as shown for  $Fr_h = 1.15$  in Figure 6.9.

The wave-cut analysis is one of the well-known methods to estimate wave resistance. This theory is built on the wave-pattern analysis, where the effects of viscosity are assumed to be negligible. For example, the transverse wave cut needs to pick two transverse sections behind the stern to measure the free surface elevation, but according to Figure 6.9, if the two sections are located behind  $x = -L$  for  $Fr_h = 0.63$ , the wave-cut method will underestimate the wave-making resistance. However, if  $Fr_h = 1.15$ , the corresponding error is less significant.

Therefore, the effects of viscosity on wave-making resistance are non-negligible for relatively low- $Fr_h$  vessels and become minor when  $Fr_h$  is high enough. An assessment of the influence of viscosity should be considered before applying wave pattern analysis.

#### 6.4.2. Effects of Bottom Friction

The friction at the bottom of a fairway is another factor affecting wave resistance. As mentioned in Section 6.1, the movements of water particles on the water bottom are retarded by bottom friction, and the corresponding kinetic energy is dissipated. Such energy dissipation ( $E_D$ ) can be estimated by integrating all instantaneous dissipation over one wavelength:

$$E_D = \int_0^\lambda \tau \cdot |V_h| dx, \quad (6.17)$$

where  $\lambda$  is wavelength, and  $V_h$  is the oscillating velocity of water particles at water bottom when the viscosity is not considered, which can be calculated analytically based on wave theories, e.g., the expressions listed in Section 6.2.1.  $\tau$  is the shear stress which can be obtained by

$$\tau = C_{fb} \cdot \frac{1}{2} \rho V_h^2, \quad (6.18)$$

where  $C_{fb}$  is the coefficient of bottom friction. To explore the significance of the energy dissipation on the water bottom, the percentage ( $\varepsilon$ ) it takes in total wave energy ( $E_T$ ) per wavelength is calculated:

$$\varepsilon = \frac{E_D}{E_T}, \quad (6.19)$$

and the total energy can be achieved by

$$E_T = E_k + E_p, \quad (6.20)$$

where  $E_k$  and  $E_p$  are kinetic energy and potential energy per wavelength, respectively, and they are obtained by

$$E_k = \frac{\rho}{2\lambda} \int_0^\lambda \int_{-h}^\eta (u^2 + w^2) dz dx, \quad (6.21)$$

$$E_p = \frac{\rho}{2\lambda} \int_0^\lambda \eta^2 dx, \quad (6.22)$$

where  $\eta$  is the elevation of the free surface,  $h$  the water depth,  $u$  and  $w$  are the velocities at the  $x$  and the  $z$  direction, respectively. When equation (6.19) is used to estimate bottom energy dissipation, the choice of a wave theory can make a difference. Chakrabarti (1987) provided a graph to show the ranges of the suitability of different wave theories. A number of CFD results of stern waves in shallow water obtained in this chapter are presented in the graph, as shown in Figure 6.10.  $h/T$  of the CFD results varies from 4.0 to 1.2.

In Figure 6.10, most CFD results are located in the range of the Stokes second order wave theory. Some results are located in the region of the Airy theory and on the border of the cnoidal wave region. To give a straightforward impression of the energy dissipation on the water bottom with different wave theories, an example is given in which specific values are assigned.

Based on the CFD results in this study, the ratio between wavelength and water depth ( $\lambda/h$ ) is always under 15. Therefore, a typical value of 10 is assigned in the calculation of the bottom energy dissipation. The material on the water bottom is assumed to be evenly distributed, and the coefficient of bottom friction ( $C_{fb}$ ), therefore, can be seen as a constant. According to Hardisty (1990), a typical value of  $C_{fb}$  is 0.1 (consider roughness on the floor). Based on equation (6.19) and the oscillating velocities of three wave theories introduced in Section 6.2.1, the percentage of the energy dissipation ( $\varepsilon$ ) is calculated and shown in Figure 6.11.

Based on Figure 6.11:

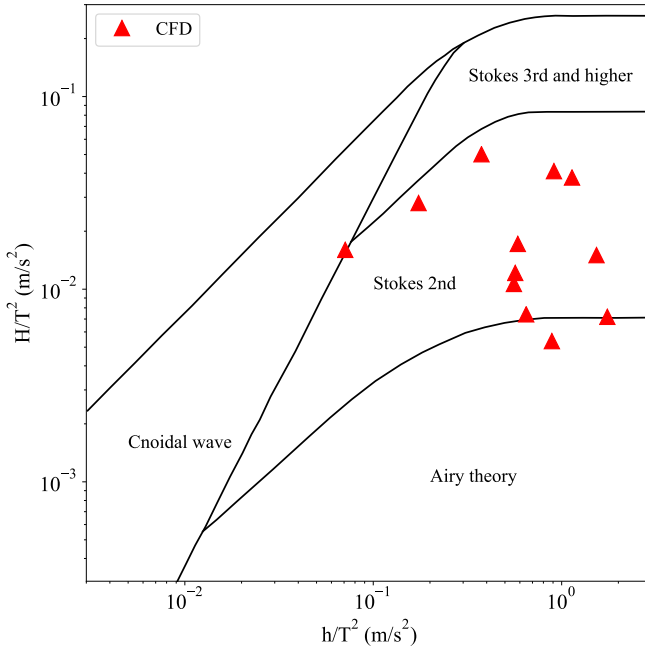


Figure 6.10: Several CFD results computed in shallow water are shown in the regions of wave theories

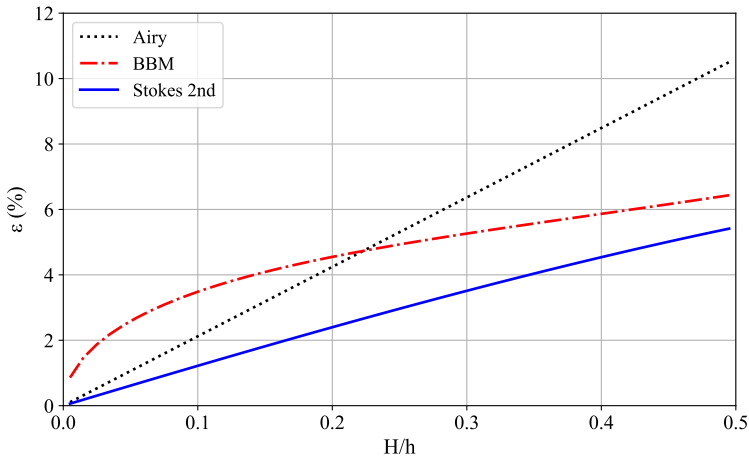


Figure 6.11: Energy dissipation on the bottom over one wavelength ( $\epsilon$ ) against wave height-water depth ratio ( $H/h$ ) for three wave theories ( $C_{fb} = 0.1, \lambda/h = 10$ )

- The percentage of energy dissipation is less than 11% for all three wave theories when  $H/h \leq 0.5$ ;
- For  $H/h \leq 0.22$ , the BBM theory gives the highest estimation of energy dissipation;
- The Airy wave theory gives a higher estimation when  $0.25 \leq H/h \leq 0.5$ ;
- For ship-generated waves, where  $H/h$  is usually less than 0.1, the energy dissipation  $\varepsilon < 4\%$  for all three methods.

Therefore, the choice of wave theory has an impact on the estimation of energy dissipation on the bottom of the fairway. Since a perceptible influence of viscosity is observed, the wave-making resistance no longer depends on Froude number only, but also depends on Reynolds number in shallow water. To explicitly show the effects of bottom friction on ship's wave-making resistance, a case study is made for the Wigley hull at  $h/T = 1.2$ , with both non-slip and slip boundary conditions, are applied to the fairway bottom, which is shown in Figure 6.12.

A curve of the coefficient of viscous resistance ( $C_v = C_t - C_w$ ) proposed in Chapter 5 is shown for comparison. The value of  $C_w$  is obtained by subtracting  $C_v$  from  $C_t$ .

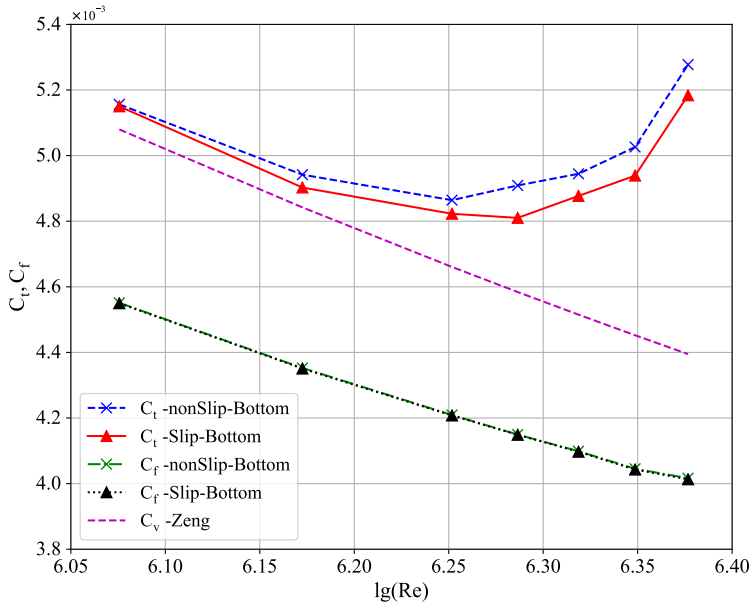


Figure 6.12: The results of  $C_t$  and  $C_f$  of the Wigley hull with non-slip and slip water bottom at  $h/T = 1.2$  (A curve  $C_v$  derived form Chapter 5 is shown for comparison)

Based on Figure 6.12, at least for  $\lg(Re) = 6.05 \sim 6.4$ :

- $C_t$  considering bottom friction is larger compared to the one ignoring the bottom friction;
- When compared with the results of  $C_f$ , where much smaller differences are observed,  $C_w$  is more sensitive to the friction of the fairway bottom;
- Whether or not the bottom friction is considered makes about 3% difference for the total resistance of the Wigley hull at  $h/T = 1.2$ .

Therefore, a physical understanding has been obtained for how and to which extent the viscosity affects the wave-making resistance of the Wigley hull at model scale. Since the influence is about 3% and will be even less at full scale, the deviation of  $C_t$  caused by bottom friction is practically negligible for this ship, but it should be considered for the sake of a physical sound model.

## 6.5. Scale Effects on Wave-making Resistance

In the previous section, the Wigley hull was used and the  $\lg(Re)$  varies from 6.05 to 6.4. In this  $Re$  range, the  $Re$  dependency of the wave-making resistance was proved, and the influence of the bottom friction on the wave-making resistance was found to be about 3%. However, higher discrepancies are expected if much fuller ship forms are considered, such as the KCS and the Rhine Ship 86 used in Chapter 5.

In this section, the scale effects, expressed by the extended range of the  $\lg(Re)$  ( $= 6.0 \sim 9.2$ ), are studied using the Wigley hull, the KCS, and the Rhine Ship 86. The Reynolds dependency of wave-making resistance for different hull forms in shallow water will be discussed.

### 6.5.1. Case Design

The main dimensions of the three ships can be found in Section 5.2.2. During the case design, the Froude number ( $Fr$ ) and depth Froude number ( $Fr_h$ ) are the controlled variables. As shown in Table 6.5,  $Fr$  is independent of water depth for each ship.  $Fr_h$  stays the same at the same water depth for all hull forms except in deep water, where the shallow water effect is minor.

Six numerical ship models are tested to investigate how the scale of a ship model affects the wave-making resistance. One numerical ship for each ship form is built at full scale for comparison, as shown in Table 6.6. The length of the models for each ship varies from 1.5 m to 15.1 m which covers the general range of the size applied for a ship model. The velocities of the Wigley hull, the KCS, and the Rhine Ship 86 at full scale are 18.70 km/h, 28.41 km/h, and 16.18 km/h, which are within the scope of velocity used by ships in inland and coastal waters.

Table 6.5: The Froude number ( $Fr$ ) and depth Froude number ( $Fr_h$ ) with different ships and water depths

$h/T$	Wigley		KCS		Rhine Ship 86	
	$Fr$	$Fr_h$	$Fr$	$Fr_h$	$Fr$	$Fr_h$
Deep*		0.1976		0.1980		0.1516
2.0		0.5422		0.5422		0.5422
1.5	0.1915	0.6261	0.1662	0.6261	0.1551	0.6261
1.3		0.6725		0.6725		0.6725
1.2		0.7000		0.7000		0.7000

\*  $h/T$  for Wigley, KCS, and Rhine Ship 86 in deep water are 15.1, 15.0, and 25.6.

Table 6.6: The Reynolds number ( $Re$ ), ship length ( $L_{pp}$ ), and velocity ( $V$ ) for each case

	$lgRe$	Wigley			KCS			Rhine Ship 86		
		$L_{pp}$ (m)	$V$ (m/s)	$V$ (km/h)	$L_{pp}$ (m)	$V$ (m/s)	$V$ (km/h)	$L_{pp}$ (m)	$V$ (m/s)	$V$ (km/h)
Model scale	6.0	1.53	0.74	2.67	1.68	0.68	2.43	1.76	0.65	2.32
	6.3	2.50	0.95	3.41	2.73	0.86	3.09	2.85	0.82	2.95
	6.5	3.30	1.09	3.93	3.63	0.99	3.57	3.80	0.95	3.41
	6.8	5.24	1.37	4.94	5.75	1.25	4.49	6.02	1.19	4.29
	7.0	7.12	1.60	5.76	7.28	1.40	5.05	8.18	1.39	5.00
	7.4	13.13	2.17	7.83	14.38	1.97	7.10	15.06	1.89	6.79
Full scale	8.5	75.00	5.20	18.70	-	-	-	85.52	4.49	16.18
	9.2	-	-	-	230.00	7.89	28.41	-	-	-

### 6.5.2. Results and Analysis

The wave-making resistance is obtained by comparing the outcomes of two types of computations: with free surface and without free surface (double-body computation). It provides insight into the scale effects on wave-making resistance qualitatively. The introduced error of this approach can be estimated by the difference of the frictional resistance coefficients ( $\Delta C_f$ ) between these two types of computation, which are shown in Table 6.7 for deep water and Table 6.8 for  $h/T = 1.2$ .

Based on Tables 6.7 and 6.8:

- In deep water, values of  $C_f$  in the computations with and without free surface are assumed identical. The results of  $\Delta C_f/C_w$  are mostly in the range of -10% ~ 10%, which can be deemed that the uncertainty of  $\Delta C_f$  is about 10% of  $C_w$ ;
- In shallow water, values of  $\Delta C_f/C_w$  are all positive and generally higher than those in deep water (valid for all ships used), which reflects the shallow water effects on  $C_f$ ;

Table 6.7: The difference of the frictional resistance affected by free surface ( $\Delta C_f$ ) and the comparison with the value of wave resistance ( $C_w$ ) in deep water

	lg(Re)	Wigley		KCS		Rhine Ship 86	
		$\Delta C_f$	$\Delta C_f/C_w$	$\Delta C_f$	$\Delta C_f/C_w$	$\Delta C_f$	$\Delta C_f/C_w$
Model scale	6.0	$-1.927 \times 10^{-5}$	-6.4%	$-8.318 \times 10^{-6}$	-7.1%	$5.500 \times 10^{-5}$	15.7%
	6.3	$-1.744 \times 10^{-5}$	-5.6%	$-1.016 \times 10^{-5}$	-7.8%	$4.406 \times 10^{-5}$	12.6%
	6.5	$-1.502 \times 10^{-5}$	-4.7%	$-1.109 \times 10^{-5}$	-8.7%	$2.568 \times 10^{-5}$	7.7%
	6.8	$-2.920 \times 10^{-6}$	-0.9%	$7.676 \times 10^{-6}$	5.9%	$3.087 \times 10^{-5}$	9.4%
	7.0	$-2.748 \times 10^{-6}$	-0.8%	$3.590 \times 10^{-6}$	2.6%	$1.612 \times 10^{-5}$	5.0%
	7.4	$-4.474 \times 10^{-6}$	-1.2%	$1.399 \times 10^{-5}$	8.3%	$1.607 \times 10^{-5}$	5.2%
Full scale	8.5	$3.615 \times 10^{-6}$	0.9%	-	-	$1.021 \times 10^{-5}$	3.1%
	9.2	-	-	$1.033 \times 10^{-5}$	5.2%	-	-

Table 6.8: The difference of the frictional resistance affected by free surface ( $\Delta C_f$ ) and the comparison with the value of wave resistance ( $C_w$ ) at  $h/T = 1.2$ 

	lg(Re)	Wigley		KCS		Rhine Ship 86	
		$\Delta C_f$	$\Delta C_f/C_w$	$\Delta C_f$	$\Delta C_f/C_w$	$\Delta C_f$	$\Delta C_f/C_w$
Model scale	6.0	$8.396 \times 10^{-5}$	13.1%	$1.662 \times 10^{-4}$	9.1%	$1.617 \times 10^{-4}$	10.3%
	6.3	$7.826 \times 10^{-5}$	13.1%	$1.615 \times 10^{-4}$	10.8%	$1.827 \times 10^{-4}$	13.3%
	6.5	$8.244 \times 10^{-5}$	14.1%	$1.730 \times 10^{-4}$	12.5%	$1.863 \times 10^{-4}$	14.4%
	6.8	$7.626 \times 10^{-5}$	13.5%	$1.652 \times 10^{-4}$	14.9%	$1.846 \times 10^{-4}$	15.6%
	7.0	$6.712 \times 10^{-5}$	12.1%	$1.559 \times 10^{-4}$	15.3%	$1.758 \times 10^{-4}$	16.6%
	7.4	$6.007 \times 10^{-5}$	11.1%	$1.411 \times 10^{-4}$	16.1%	$1.664 \times 10^{-4}$	16.2%
Full scale	8.5	$4.387 \times 10^{-5}$	8.6%	-	-	$1.322 \times 10^{-4}$	14.7%
	9.2	-	-	$1.038 \times 10^{-4}$	18.0%	-	-

- the results of  $\Delta C_f$  are always less than 18% of  $C_w$ , i.e.,  $\Delta C_f$  is roughly one magnitude less than  $C_w$ , which means the method using two types of computations to obtain  $C_w$  is acceptable.

For a computation with a free surface, the area of the wetted surface on the hull is different from that in a double-body computation. In this study, the actual area is calculated and applied when analyzing the results. The grid distribution under the water stays the same for both computations with and without free surface. For  $\lg(Re) \leq 6.5$ , the value of  $y^+$  is less than 5, and for other Reynolds numbers, wall functions are applied ( $30 \leq y^+ \leq 200$ ). The same value of  $y^+$  is guaranteed for the same speed in the calculations with and without free surface. Results of  $C_w$  of all cases are shown in Figure 6.13.

Based on Figure 6.13:

- When  $Fr_h \leq 0.5422$ , the wave resistance coefficient ( $C_w$ ) can still be seen as independent of Reynolds number for all three ships used;

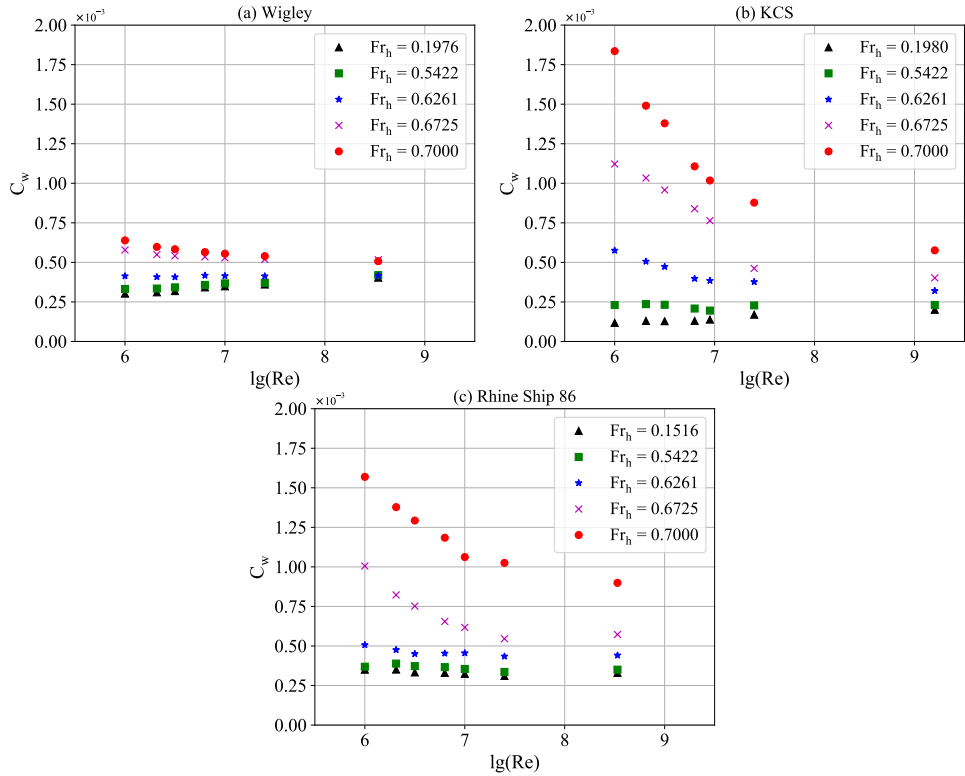


Figure 6.13: The wave-making resistance ( $C_w$ ) against base10 logarithm of Reynolds number ( $\lg(Re)$ ) with different depth Froude number ( $Fr_h$ ) for (a) the Wigley hull, (b) the KCS, and (c) the Rhine Ship 86

- When  $Fr_h = 0.6261$ , ship form begins to play a role in the scale dependency of  $C_w$ : the values of  $C_w$  of the KCS at model scale show larger values than full scale. For instance, the value of  $C_w$  of the KCS increases by 44% at  $\lg(Re) = 6.0$  than that at  $\lg(Re) = 9.2$ ;
- When  $Fr_h = 0.7000$ , the scale dependency of  $C_w$  is observed for all three ships. For the Wigley hull at model scale, the increase of  $C_w$  is 26% (maximum) compared to full scale, but for the other two ships, of which the block coefficient ( $C_B$ ) is much higher, the value is 219% for the KCS and a value of 75% for the Rhine Ship 86;
- Scale effects on the wave-making resistance coefficient are decreasing with an increasing Reynolds number. This is in line with the common sense that the effect of viscosity is smaller when the Reynolds number is larger.

Therefore, the assumption that  $C_w$  is independent of ship scales is still valid for  $Fr_h \leq 0.5422$ . It should be reevaluated when  $Fr_h > 0.5422$ . If  $Fr_h$  is

reaching to 0.700, the scale effects on wave-making resistance are significant, and the assumption that  $C_w$  is independent of  $Re$  in the conventional extrapolation is challenged and needs to be revised.

Based on the results shown in Figure 6.13, a modification can be given for the three selected ships. A factor  $\beta$  is defined to represent the difference of  $C_w$  between full and model scale.

$$C_{ws} = \beta \cdot C_{wm}, \quad (6.23)$$

where the subscripts  $s$  and  $m$  denote full scale and model scale, respectively.

For the KCS at  $Fr_h > 0.5422$ , and  $6.0 \leq \lg(Re) \leq 7.4$ :

$$\beta = 1 + 0.2324 \lg(Re) - 1.117 \exp(1.27 \cdot Fr_h^2). \quad (6.24)$$

For the Rhine Ship 86 at  $Fr_h > 0.6261$ , and  $6.0 \leq \lg(Re) \leq 7.4$ :

$$\beta = 1 + 0.3035 \lg(Re) - 1.548 \exp(0.7976 \cdot Fr_h^2). \quad (6.25)$$

For other cases of the KCS and the Rhine Ship 86 and also the Wigley hull:

$$\beta = 1.0. \quad (6.26)$$

The above equations contain no ship parameters and cannot be used to determine the value of  $\beta$  for ships whose dimensions are very different from the three selected ships. An expression of  $\beta$  as a function of ship parameters is subject to future research.

## 6.6. Concluding Remarks

In this chapter, shallow water effects on ship-generated waves are studied in both inviscid flow and viscous flow. The CFD method was verified and validated for the calculations of ship wave properties. The effects of bottom friction and ship scales on wave-making resistance were explicitly studied. Based on the results, some concluded remarks can be made.

In inviscid flow:

- The bow wave is higher when the water is shallower, which indicates a higher wave-making resistance;
- For stern waves, when  $Fr_h < 1.0$ , the height of the first crest of stern waves is increasing with decreasing water depth. When  $Fr_h > 1.0$ , the height drops immediately and then continue increasing with a decreasing water depth;
- Ship-generated waves become longer in shallow water for the same navigating speed. When  $Fr_h > 1.0$ , the wavelength increases dramatically and approximate infinity, which leads to the disappearance of the transverse wave system;

- The waves generated by the bow will arrive earlier to the stern in shallower water, which changes the wave superposition behind the stern.

In viscous flow:

- The viscosity of the water will lower the wave height behind the stern by which errors will be caused for wave-cut analysis;
- It was proved that the Reynolds number dependency of the wave-making resistance. The influence of the bottom friction on the wave-making resistance of the Wigley hull was found to be about 3%;
- When  $Fr_h > 0.5422$ , wave-making resistance starts to be affected by ship scales, which applies to both slender and fuller ships. The assumption that  $C_w$  is independent of  $Re$  in the conventional extrapolation is challenged and needs to be revised. Recommendations to remedy the comparison law are given for the three selected ships.

# 7

## A Method to Improve Resistance prediction in Shallow Water

Shallow water effects on the three main components of ship resistance, i.e., the frictional resistance, the viscous pressure resistance, and the wave-making resistance, have been addressed in the previous chapters. Empirical formulas have been developed to improve the prediction of each component considering ship scales and water depth for three ship types, (the Wigley hull, the KCS, and the Rhine Ship 86). In this chapter, a method including those considerations is proposed for ship resistance extrapolation in shallow water. This method also consolidates the physical basis of the extrapolating approach. Finally, the robustness of the proposed method is evaluated and compared with the conventional approach.

### 7.1. Motivation

Ship model tests are conducted to predict the resistance of full-scale ships through the method of resistance extrapolation. In the traditional method recommended by the International Towing Tank Conference (ITTC, 2017j), the ITTC57 correlation line is used to predict the frictional resistance, a constant form factor is recommended for viscous pressure resistance, and Reynolds number independence applies for the wave-making resistance. In shallow water, ship resistance is affected by the limited water depth, leading to significant errors in the resistance prediction. There are some methods available to correct the shallow water effects (García-Gómez, 2000; Millward, 1989; Raven, 2016), but they focused on modifying the form factor without explicitly addressing shallow water effects on the frictional resis-

tance and the wave-making resistance.

In the previous chapters, the ITTC57 correlation line (Chapter 4), the assumption of a constant form factor (Chapters 5), and the Reynolds number ( $Re$ ) independence of wave-making resistance (Chapter 6) have been challenged in shallow water. The three resistance components are related to different physical aspects, i.e., the shear stress along the hull, the pressure difference caused by viscosity in the course direction, and the wave system. Each component suffers from shallow water effects individually. Corrections that only concerns the form factor, therefore, have a weak physical basis.

To search for a sounder physical basis for the model-ship resistance extrapolation, individual modifications for each resistance component considering shallow water effects are expected, which is the main concern of this chapter. The extrapolation method will be modified based on the results obtained in Chapters 4 through 6.

## 7.2. The Proposed Method

The new expression of the total resistance coefficient of a bare hull is shown in equation (7.1), expressed by the three main components of ship resistance. To distinguish each component from the conventional method, an asterisk (\*) is added to each resistance symbols:

$$C_t = (1 + k^*)C_f^* + C_w^*, \quad (7.1)$$

where  $C_t$  is the total resistance coefficient for both models and ships.  $C_f^*$  is the friction resistance coefficient for which model-ship correlation line considering shallow water effects should be applied.  $1+k^*$  is the form factor defined based on  $C_f^*$  and includes effects of shallow water.  $C_w^*$  is the wave-making resistance coefficient that varies with water depth and Reynolds number. In principle, all variables shown in equation (7.1) depend on both Reynolds number and depth Froude number.

### 7.2.1. Wave-making Resistance Coefficient $C_w^*$

For  $h/T \geq 1.5$ , it was found that the  $Re$  independence of wave-making resistance is still applicable (Chapter 6), which means the treatment of  $C_w^*$  remains the same as in the conventional approach. Thus the extrapolation method can be written as

$$C_{ts} = (1 + k_s^*)C_{fs}^* - (1 + k_m^*)C_{fm}^* + C_{tm}^*, \quad (7.2)$$

where the subscripts  $s$  and  $m$  denote full scale and model scale, respectively.

For  $h/T < 1.5$ , shallow water effects on  $C_w^*$  become significant (26% ~ 219% based on Chapter 6) and should be modified. As an example shown in equation (7.3), a correction factor  $\beta$  is used for  $C_w^*$ . Thus, the new extrapolation method can be derived and shown in equation (7.4):

$$C_{ws}^* = \beta \cdot C_{wm}^* \quad (7.3)$$

$$C_{ts} = (1 + k_s^*)C_{fs}^* - \beta \cdot (1 + k_m^*)C_{fm}^* + \beta \cdot C_{tm}. \quad (7.4)$$

The factor  $\beta$  is a function of the hull form and the water depth. A general prediction of  $\beta$  should be determined based on an extensive database in which a large number of ships with different hull forms are included. However, the results of  $C_w^*$  derived from the three ships that are assessed in Chapter 6 can provide initial empirical values of  $\beta$ .

The applied three ships are regarded as representatives of three ship categories with different main dimensions and can be used to estimate the  $\beta$  of a different vessel. Errors may be introduced into  $C_w^*$  if the parameters (e.g.,  $C_B$ ) of a vessel deviates significantly from the three ships. Since the proportion of  $C_w^*$  is at the level of 10% of  $C_t$ , an error of about 20% in  $C_w^*$  can only lead to about 2% difference in  $C_t$ . However, for cases when  $h/T \approx 1.2$ ,  $C_w^*$  strongly depends on the hull form and more significant errors in  $C_t$  will be caused (> 5%). In this case, the extrapolation of  $C_w^*$  of a different vessel should be treated specifically.

### 7.2.2. Frictional Resistance Coefficient $C_f^*$

For  $h/T \geq 1.2$ , a general prediction for the frictional resistance in shallow water can be built. As proposed in Chapter 5 (equation (5.9)), the expression of  $C_f^*$  is repeated here:

$$C_f^* = \frac{0.08468}{(\lg Re - 1.631)^2} \cdot \left( 1 + \frac{c_1}{\lg Re + c_2} \cdot \left( \frac{h}{T} \right)^{c_3} \right)$$

where  $Re$  is Reynolds number,  $h$  the water depth,  $T$  the draft of the ship.  $c_1$ ,  $c_2$ , and  $c_3$  are functions of hull forms. The first part of the equation can be seen as a numerical correlation line for ship's frictional resistance in deep water. The second part of the equation expresses the influence of both shallow water effects and ship form effects. This formula is considered to be suitable for ships similar to the Wigley hull, the KCS, and the Rhine Ship 86 sailing in shallow water. ITTC 57 correlation line is essentially a particular case of this approach at the condition of deep water. Based on the study of Chapter 5,  $c_1$ ,  $c_2$ , and  $c_3$  for the three selected ships is already given in Table 5.7 and is shown again in Table 7.1 for further demonstration in this chapter.

In Chapter 5, a more general method was also explored using a virtual ship to predict the  $C_f^*$  of different ship types. The block coefficient was selected as a presentative of ship parameters.

For  $h/T < 1.2$ , which can be seen as extremely shallow water, ship's friction will decrease with a decreasing water depth, especially for a ship with a flat bottom at model-scale Reynolds numbers (Section 5.5). In this case, the movement of the flow around the ship hull is different from the cases when

Table 7.1:  $c_1$ ,  $c_2$ , and  $c_3$  for the Wigley hull, the KCS, and the Rhine Ship 86 (Table 5.7)

	$c_1$	$c_2$	$c_3$
Wigley hull	0.3466	-0.4909	-1.461
KCS	1.2050	-0.5406	-1.451
Rhine Ship 86	1.1680	-0.5238	-1.472

$h/T \geq 1.2$  and also varies with different hull forms. Although the drop of the friction can be predicted based on the thickness of ship's boundary layer, a more sophisticated prediction needs to be subject to further investigations.

### 7.2.3. The Form Factor $1+k^*$

The prediction of the form factor  $1+k^*$ , which is defined in Chapter 5 (Section 5.4.2), should be determined based on whether a ship has a transom:

For a bare ship hull without a transom, the expression  $1+k^*$  of follows the form of equation (7.5).

$$1+k^* = \left( a_1 + \frac{a_2}{(\lg Re + a_3)^{a_4}} \right) \cdot \left( 1 + a_5 \cdot \left( \frac{h}{T} \right)^{a_6} \right) \quad (7.5)$$

In equation (7.5),  $a_1$  can be seen as the form factor for the full-scale ship in deep water. The parameters  $a_2$ ,  $a_3$ , and  $a_4$  indicate the influence of Reynolds number on the form factor, and the factors  $a_5$  and  $a_6$  express the shallow water effects. For the Wigley hull and the KCS at  $h/T \geq 1.2$ , parameters in equation (7.5) can be provided based on the results obtained in Chapter 5 and shown in Table 7.2.

Table 7.2: The  $a_1 \sim a_6$  for the Wigley hull and the KCS

	$a_1$	$a_2$	$a_3$	$a_4$	$a_5$	$a_6$
Wigley	1.03	1.276	-3.277	4.790	0.06303	-1.700
KCS	1.075	1.086	-3.419	3.513	0.2066	-1.887

Although the Wigley hull has a different size compared to the KCS, they have similar values for  $a_1$ ,  $a_3$ , and  $a_6$ . Other parameters are considered to be relevant to the hull form.

For ships with a transom, this stern form provides an additional (non-linear) influence apart from the hull form and the water depth on the form factor. In this case,  $1+k^*$  can be described by a polynomial fitting for the Rhine Ship 86, which is obtained in Chapter 5 (equation (5.17)) and also shown here for illustration:

$$(1 + k^*)_{RhineShip86} = (1 + k^*)_{Wigley} + \left( -0.004165 \cdot (\lg Re)^3 + 0.1085 \cdot (\lg Re)^2 - 0.8726 \cdot \lg Re + 2.367 \right) \cdot \left( 1 + 1.269 \times 10^4 \cdot (\lg Re)^{-6.155} \cdot (h/T)^{-4.04} \right)$$

Similarly, the above equation is valid for  $h/T \geq 1.2$ . In extremely shallow water ( $h/T < 1.2$ ), the value of  $1+k^*$  highly depends on the frictional resistance and has been explored together with the ship's friction in extremely shallow water (Section 5.5).

### 7.3. Robustness Evaluation

In Section 7.2, the process of extrapolating the resistance from model tests to full-scale ships in shallow water was proposed. The robustness of the proposed method will be evaluated in this section. Several new cases (Table 7.3) with the same ships but different velocities, which are not used to determine the expressions in Chapter 5, are selected in this evaluation. Four water depths are considered:  $h/T = 2.0, 1.5, 1.3,$  and  $1.2$ . The robustness of this method can be confirmed if it can give acceptable outcomes for these new cases.

Table 7.3: New cases selected in the performance evaluation

	Wigley		KCS		Rhine Ship 86	
	1/30 model	full scale	1/40 model	full scale	1/30 model	full scale
$L$ (m)	2.50	75.00	5.75	230.00	2.85	85.52
$V$ (m/s)	0.95	5.20	1.25	7.89	0.82	4.49
$Fr$	0.192	0.192	0.166	0.166	0.155	0.155
$\lg(Re)$	6.32	8.53	6.80	9.20	6.31	8.53

Due to the absence of full-scale resistance tests of bare hulls, numerical calculations are implemented instead. The results of the total resistance at full scale are used as a benchmark to evaluate both the proposed method and the conventional approaches. Computations are performed both with a free surface and without a free surface. Thus, all three resistance components can be derived separately. Among the benchmark,  $C_{fs}$  and  $C_{ts}$  (the subscript  $s$  denotes full-scale ships) are calculated with a free surface, and  $k_s$  and  $k_s^*$  are obtained by the computations without a free surface.

Numerical calculations instead of physical model tests are also applied for model-scale ships to ensure that the results of resistance at both model scale and full scale have the same numerical uncertainties resulting from, e.g., mesh type, the selection of a turbulence model, etc. The results of the total resistance at model scale will be implemented in the process of extrapolation.

In this evaluation, three methods, as shown in Table 7.4, are compared with their abilities to obtain the three resistance components and the total resistance.

Table 7.4: The compared three methods

Symbol	Method	$C_f$	$k$ & $k^*$	$C_w$
MA	Method A: Traditional way	ITTC 57	Method of <a href="#">Prohaska (1966)</a> ; Constant $k$	$Re$ independence
MB	Method B: with $1+k$ correction	Numerical friction line on flat plate	Method of <a href="#">Prohaska (1966)</a> in deep water; Corrected $k$ for shallow water with <a href="#">Millward (1989)</a>	$Re$ independence
Pro	Proposed method	Proposed formulas of $C_f^*$	Proposed formulas of $1+k^*$	Modified $C_w^*$

The factor  $k$  is the form factor using the traditional definition and  $k^*$  follows the new definition introduced in Chapter 5 (Section 5.4.2).  $C_f$  in the method “MB” is calculated with a turbulent flat plate friction line derived in Chapter 5 (Section 5.4.1). The modified  $C_w^*$  in the method of “Pro” is based on the results in Chapter 6 (Figure 6.13). For the Wigley hull at all water depths, the values of  $\beta$  are equal to one. For the KCS and the Rhine Ship 86,  $\beta$  is equal to one at  $h/T \geq 1.5$ , and at  $h/T = 1.3$  and 1.2, the derived  $\beta$  are shown in Table 7.5.

Table 7.5: The values of  $\beta$  for the KCS and the Rhine Ship 86 at  $h/T = 1.3$  and 1.2

	$\beta$	
	$h/T = 1.3$	$h/T = 1.2$
KCS	0.479	0.558
Rhine Ship 86	0.696	0.653

In Figure 7.1 and Figure 7.2, the results of  $C_{ts}$ ,  $C_{fs}$ ,  $k_s$  &  $k_s^*$  and  $C_{ws}$  (at full scale) derived from the method “MA”, “MB”, and “Pro” are shown for comparison. In the methods MA and MB, the conventionally-defined  $k_s$  is used, and in the method Pro, the newly-defined  $k_s^*$  is used. Discrepancies of all resistance components and the total resistance compared with the benchmark are shown in Table 7.6, Table 7.7, and Table 7.8 for the Wigley hull, the KCS, and the Rhine Ship 86.

Based on Figure 7.1, Figure 7.2 and tables 7.6 through 7.8, the following observations and illustrations are made:

- In general, for the extrapolated total resistance at full scale, results generated by the proposed method are within the range of  $\pm 5\%$  error of the benchmark, which confirms the robustness of the proposed

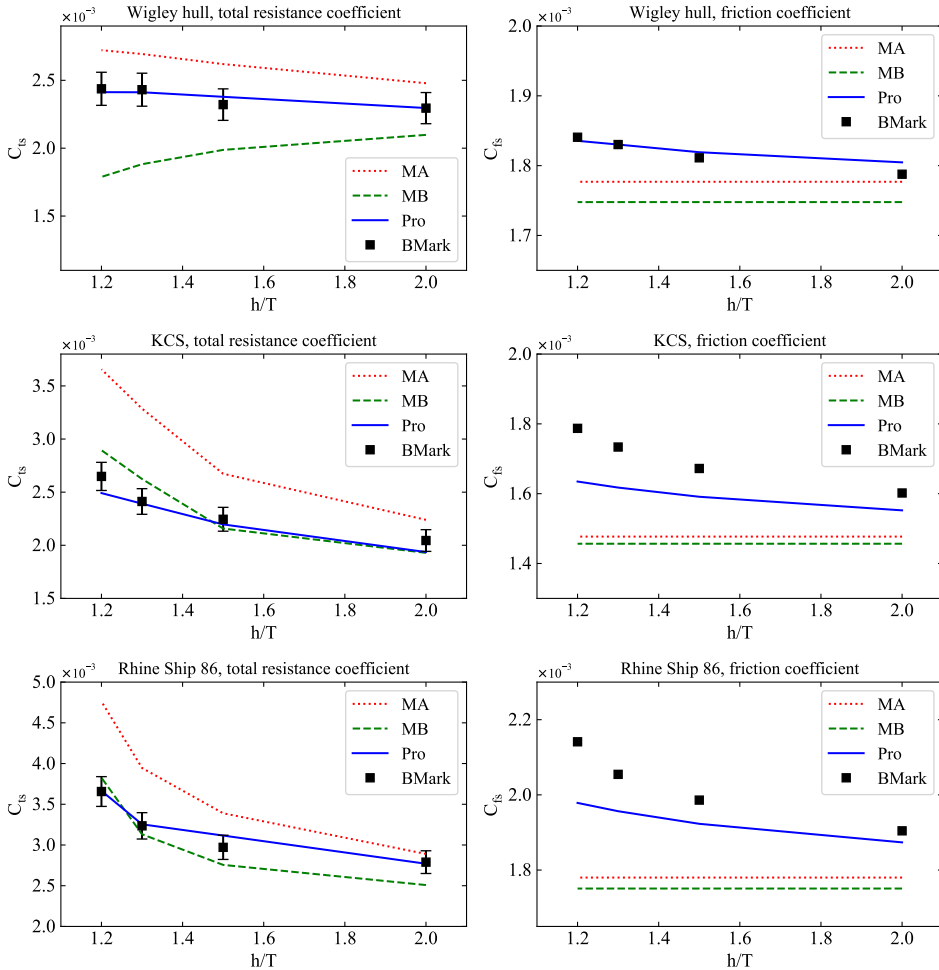


Figure 7.1: Total resistance coefficient ( $C_{ts}$ ) with  $\pm 5\%$  error bar and frictional resistance coefficient ( $C_{fs}$ ) at full scale calculated by the methods “MA”, “MB”, and “Pro” for the Wigley hull, the KCS, and the Rhine Ship 86 and compared with the benchmark (“Bmark”)

method. Also, for the three resistance components, the proposed method shows better agreements with the benchmark when compared with the methods MA and MB. Small discrepancies for  $C_{fs}$  and  $k_s^*$  (at  $h/T \leq 1.5$ ) can be explained by the absence of free surface when the empirical  $C_f$  and  $k^*$  are developed (Chapter 5);

- For all three ships, the method MA underestimates both  $C_{fs}$  (-18% ~ -1%) and  $k_s$  (-75% ~ -50%) since shallow water effects are excluded in this method. Therefore, the  $C_{ws}$  obtained based on the assumption of  $Re$  independence is overestimated (60% ~ 340%) leading to 3.6% ~

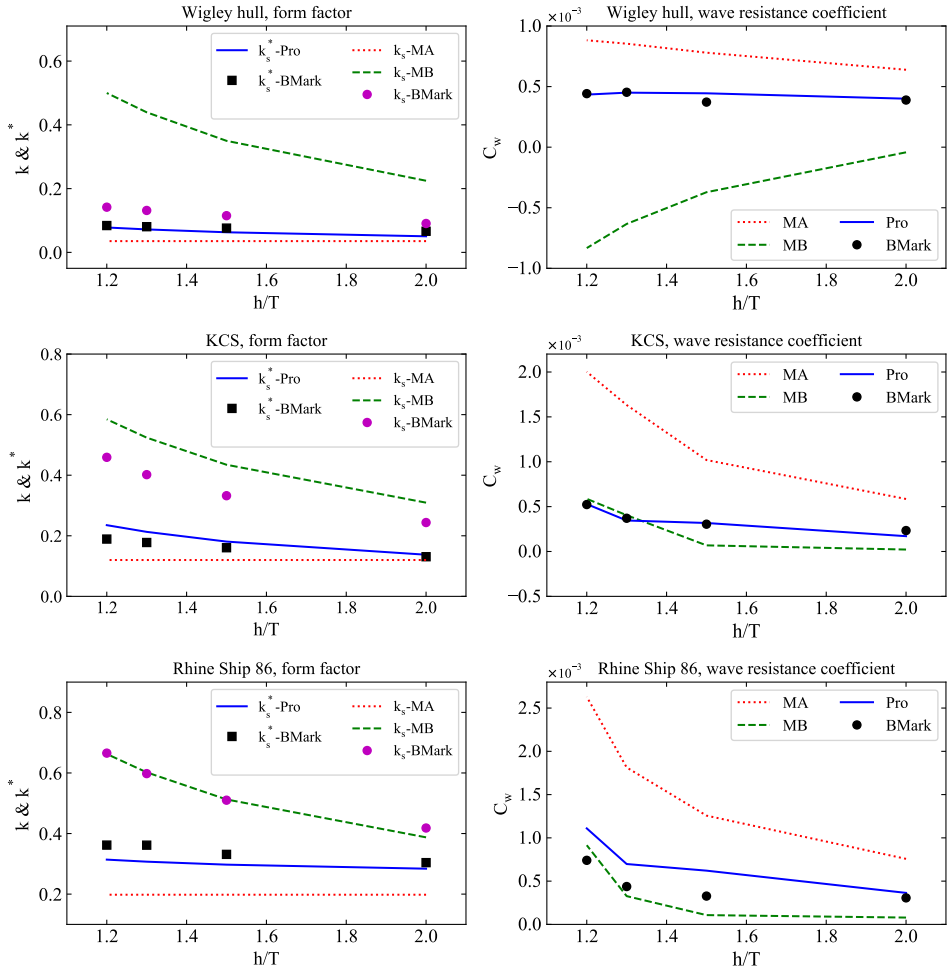


Figure 7.2: Form factor ( $k_s$  &  $k_s^*$ ) and wave-making resistance coefficient ( $C_{ws}$ ) at full scale calculated by the methods “MA”, “MB”, and “Pro” for the Wigley hull, the KCS, and the Rhine Ship 86 and compared with the benchmark (“BMark”)

38% overestimation of  $C_{ts}$ , with a trend of becoming worse in shallower water;

- For the Wigley hull, the method MB corrects  $k_s$  considering shallow water effects, but the corrected  $k$  show much higher values (140% ~ 250%) than the benchmark resulting in negative values of  $C_{ws}$  (-290% ~ -110%). The method MB shows large discrepancies for the Wigley hull since such a slender ship is not applied when MB was developed;
- For the KCS, the method MB provides satisfactory results for  $C_{ts}$  at  $h/T \geq 1.5$  but slightly larger errors ( $\approx 9\%$ ) at  $h/T < 1.5$ . More significant

Table 7.6: Discrepancies (%) of all resistance components and the total resistance compared with the benchmark (for the Wigley hull)

$h/T$	$C_{fs}$			$k_s$ & $k_s^*$			$C_{ws}$			$C_{ts}$		
	MA	MB	Pro	$k_s$ - MA	$k_s$ - MB	$k_s^*$ - Pro	MA	MB	Pro	MA	MB	Pro
2.00	-0.61	-2.23	0.95	-61.04	147.99	-23.87	64.29	-110.92	2.88	8.00	-8.59	0.03
1.50	-1.89	-3.50	0.44	-69.34	203.92	-17.13	109.64	-199.95	19.52	12.86	-14.37	2.48
1.30	-2.91	-4.50	0.00	-73.16	234.09	-10.58	88.46	-239.80	-0.72	10.81	-22.58	-0.78
1.20	-3.47	-5.05	-0.28	-75.10	252.59	-7.19	99.68	-288.49	-1.80	11.67	-26.62	-1.01

Table 7.7: Discrepancies (%) of all resistance components and the total resistance compared with the benchmark (for the KCS)

$h/T$	$C_{fs}$			$k_s$ & $k_s^*$			$C_{ws}$			$C_{ts}$		
	MA	MB	Pro	$k_s$ - MA	$k_s$ - MB	$k_s^*$ - Pro	MA	MB	Pro	MA	MB	Pro
2.00	-7.80	-9.07	-3.11	-50.77	26.92	5.02	150.88	-90.72	-26.83	9.51	-5.67	-5.31
1.50	-11.67	-12.89	-4.84	-63.89	30.75	12.62	235.05	-77.59	4.40	19.09	-3.88	-2.16
1.30	-14.80	-15.98	-6.70	-70.14	30.40	19.75	340.75	9.15	-6.75	36.24	8.78	-4.35
1.20	-17.35	-18.50	-8.53	-73.86	27.33	24.25	282.84	12.20	0.96	38.07	9.31	-3.82

Table 7.8: Discrepancies (%) of all resistance components and the total resistance compared with the benchmark (for the Rhine Ship 86)

$h/T$	$C_{fs}$			$k_s$ & $k_s^*$			$C_{ws}$			$C_{ts}$		
	MA	MB	Pro	$k_s$ - MA	$k_s$ - MB	$k_s^*$ - Pro	MA	MB	Pro	MA	MB	Pro
2.00	-6.53	-8.06	-1.61	-52.66	-7.37	-6.58	147.18	-74.23	18.83	3.60	-10.09	-0.71
1.50	-10.38	-11.85	-3.18	-61.18	0.48	-10.25	284.12	-67.21	89.80	14.08	-7.26	4.87
1.30	-13.36	-14.78	-4.77	-66.88	0.70	-15.08	314.47	-25.35	59.44	21.97	-3.20	0.61
1.20	-16.87	-18.23	-7.59	-70.25	-0.44	-13.26	255.16	23.58	49.85	30.24	4.63	1.44

errors can be seen for the three resistance components. The method MB underestimates the  $C_{fs}$  by -18% ~ -9%.  $k_s$  is overestimated by about 30% since the effects of ship scales (or Reynolds number) is not considered. Coincidentally, the underestimation of  $C_{fs}$  and the overestimation of  $k_s$  generate roughly correct  $C_{ws}$  (especially at  $h/T \leq 1.5$ ) and thus approximately correct  $C_{ts}$ ;

- For the Rhine Ship 86, the method MB generates satisfactory results for  $C_{ts}$  at  $h/T < 1.5$  but larger errors ( $\approx 10\%$ ) at  $h/T \geq 1.5$ . Similar to the KCS, the absolute value of the slope of the curve  $C_{ts}$  is larger when  $h/T < 1.5$ . A good agreement is found for  $k_s$  due to the coincidence that  $k_s$  of the Rhine Ship 86 at the two selected Reynolds numbers are comparable.

In summary, the order of the performance of the three methods is Pro > MB > MA. Large errors (up to 38%) can be caused by MA which reinforces the requirement of shallow water correction. MB can generate relatively satisfactory extrapolations for the KCS and the Rhine Ship 86, but it does not apply for the Wigley hull. In method MB, shallow water effects on both the frictional resistance and the viscous pressure resistance are included in

the form factor. This treatment builds a weak physical basis and makes MB unreliable when used to analyze a different ship form, such as the Wigley hull.

The proposed method deals with the total resistance by considering shallow water effects and Reynolds number on each resistance component individually, which consolidates the physical basis and can generate robust results. It should be noted that the benchmark is based on CFD computations. A proof for the proposed method that has a better performance requires full-scale ship resistance tests, which is, unfortunately, known to be a tough task. However, the proposed method shows the way of obtaining a robust and physically-correct extrapolation of ship resistance in shallow water.

# 8

## Conclusions and Recommendations

This dissertation describes an approach to improve the extrapolation of ship resistance. This approach is to be applied to model scale resistance results carried out in shallow water. The effects of limited water depths on the three components of ship resistance (i.e., the frictional resistance, the viscous pressure resistance, and the wave-making resistance) have been studied individually. Empirical formulas have been developed for three ship types in various water depths. In this chapter, the conclusions are drawn based on the respective concluding remarks addressed in Chapters 4 through 7. The main findings obtained in the process of reaching the final goal and the sub-goals listed in Chapter 1 are presented and discussed. Finally, recommendations from difference aspects are provided as guidelines to further consolidate the findings and the proposed method in this research.

### 8.1. Conclusions

Based on the results achieved in the previous chapters, the mechanism of how limited water depth affects each resistance component were explored and discussed. Understandings of the mechanisms enlighten a different way to improve the prediction of ship resistance considering shallow water effects. In this section, the conclusions are presented in sequence for the proposed approach and shallow water effects on the three resistance components.

#### 8.1.1. Final Goal

The final research goal, as described in Section 1.1 and addressed in Chapter 7, is shown as follows:

*To understand the mechanisms of shallow water effects on ship resistance and based on this to improve the extrapolation of ship resistance in shallow water.*

Since different resistance components are the results of different physical phenomena and thus are affected by shallow water differently, shallow water effects on each component have been studied individually (Chapters 4 ~ 6).

Physically, limited water depth affects both the velocity field and the pressure field around a ship hull. The integral of the force on the hull surface is therefore influenced accordingly. In shallow water, the boundary layer of a ship cannot develop freely, which influences the shear stress and leads to a water depth-dependent frictional resistance.

In addition, the limited under-keel space and viscosity prevent the flow at the stern from recovering to its initial velocity, which enlarges the pressure difference between the bow and the stern leading to a strongly speed-dependent viscous pressure resistance. Also, an oscillating boundary layer is generated on the water bottom in which a part of wave energy is dissipated, leading to a viscosity-dependent wave-making resistance. Therefore, an explicit and physically-correct basis would be realized by modifying shallow water effects individually for each component.

Based on this concern, modifications are proposed, and none of the three parts of resistance are expected to stay the same for model-scale and full-scale ships. To distinguish them from the conventional way, an asterisk (\*) is applied and shown in equation (8.1):

$$C_t = C_f^* + C_{vp}^* + C_w^*. \quad (8.1)$$

In Chapter 7, a new extrapolation method was proposed to calculate the total resistance at full scale, which is summarized from equations (8.2) to (8.4):

$$C_{vp}^* = k^* \cdot C_f^*, \quad (8.2)$$

$$C_{ws}^* = \beta \cdot C_{wm}^*; \quad (8.3)$$

$$C_{ts} = (1 + k_s^*)C_{fs}^* - \beta \cdot (1 + k_m^*)C_{fm}^* + \beta \cdot C_{tm}. \quad (8.4)$$

The subscripts  $m$  and  $s$  indicate model scale and full scale, respectively. The scale effects on wave-making resistance should be first corrected. Based on the result in Chapter 7, the value of  $\beta$  is equal to one for  $h/T$  (water depth/ship draft)  $\geq 1.5$ , and for smaller values of  $h/T$ , its value should be determined based on ship dimensions. Correlations for both the frictional resistance and the form factor follows the approach illustrated in Chapter 5.

Based on the evaluation in Chapter 7, the extrapolation of the total resistance using the conventional method without shallow water corrections has 3.6% ~ 38% deviations from the results of full-scale ship simulations; the conventional method with shallow water corrections (only for the form factor) had -5% ~ 10% deviations for relatively fuller ships but had up to -26% for a slender ship. The method proposed in this research, which is closer to the actual physics, showed a robust performance and reduced the deviation to -5.3% ~ 4.9% for all selected ships.

### 8.1.2. Frictional Resistance

The first sub-goal, as described in Section 1.1 and addressed in Chapter 4 and a part of Chapter 5, is shown as follows:

*To understand the mechanism of how frictional resistance is altered in shallow water.*

To reach this sub-goal, the distribution of the velocity and the pressure of the flow in limited water condition were first studied with a two-dimensional (2D) wall-bounded flow. In shallow water, the flat ship bottom, which exists on nearly all inland cargo vessels, can be simplified to a 2D still flat plate bounded by another moving plate parallel to it (ship-based coordinate system, introduced in Chapter 4). Due to the limited space and the boundary layers on both plates, the flow is accelerated more than in the unlimited situation. Therefore, a thinner boundary layer is formed, and the pressure gradient along the plate can no longer be treated as zero. This challenges the usual assumption of zero pressure gradient in deep water, based on which many traditional friction lines for both laminar flow and turbulent flow were developed.

Besides, an increased velocity gradient perpendicular to the plate is observed in the thinner boundary layer. By definition, the shear stress on the still plate increases accordingly, which leads to higher frictional resistance. Such increase can reach up to 50% at  $\lg(Re) = 5.6$  and around 10% at  $\lg(Re) = 9.2$ . A numerical friction line considering shallow water effects was proposed as a modification for the current ITTC57 correlation line. In this method, the Reynolds number is no longer the only factor influencing the frictional resistance, but the clearance between the plates plays a role too. By using this method to correct shallow water effects on ship's flat bottom and applying the ITTC57 line for the rest of the wetted surface, the prediction of ship's frictional resistance of the whole wetted surface has a better agreement with the CFD results of an actual 3D vessel if compared with the traditional approach.

In Chapter 5, the study of shallow water effects on frictional resistance was extended to three-dimensional (3D) flow. Generally, for  $h/T \geq 1.2$ , how the frictional resistance is affected by a limited flow space follows the similar conclusions drawn in 2D cases (i.e., the friction increases in shallow water).

For instance, when  $h/T = 1.2$ , the increase of the frictional resistance is around 5% for a slender ship and 10% ~ 20% for fuller vessels. A general expression was explored to predict the frictional resistance at the Reynolds number covering both the model-scale and the full-scale vessels.

For  $h/T < 1.2$  (extremely shallow), however, the flow under the ship's bottom is decelerated due to the extremely restricted under-keel clearance. Therefore, the bottom is exposed to a velocity-reduced flow, and a decrease in the frictional resistance will be observed for the ships with a large flat bottom. Since this observation challenges the findings obtained from the cases at  $h/T \geq 1.2$ , the prediction of frictional resistance on a vessel with a large flat bottom in extremely shallow water should be given individually.

### 8.1.3. Viscous Pressure Resistance

The second sub-goal, as described in Section 1.1 and addressed in Chapter 5, is shown as follows:

*To understand the mechanism of how viscous pressure resistance is altered in shallow water.*

To reach this sub-goal, a new explanation of the form factor was proposed. Different from the conventional definition, where a turbulent flat plate friction line is used as the denominator, the new form factor was defined based on the computed frictional resistance. By this definition, the newly-defined form factor explicitly represents the viscous pressure resistance. This definition corrects the weak physical basis of the conventional definition in which the form factor includes the effects of shallow water on both the frictional resistance and the viscous pressure resistance. Also, the effects of a transom are allowed to be considered into the newly-defined form factor to make it applicable for a large number of inland vessels. When  $h/T \leq 2.0$ , it was found that the limited water depth can cause 5% ~ 20% increase in the form factor independence of whether a transom exists.

The value of the newly-defined form factor is inversely proportional to  $h/T$ , i.e., the net pressure difference along the ship hull caused by viscosity is increasing with a decreasing  $h/T$ , even in extremely shallow water. For ships without a transom, the value of the newly-defined form factor at model scale is larger than that at full scale (up to 10%). However, with the increase of the Reynolds number, the form factor at the same  $h/T$  turns constant, especially for  $\lg(Re) \geq 7.6$ . For ships with a transom, since the influence of the low-pressure area behind the stern is enlarged from a certain high Reynolds number ( $\lg(Re) \approx 6.8$ ), the newly-defined form factor first decreases ( $\lg(Re) < 6.8$ ) and then increases. This property makes the form factor for a full-scale ship similar to or even larger than the form factor at model scale.

Empirical formulas of the newly-defined form factor are fitted based on the numerical results of the three ships applied in this research. Effects of both the Reynolds number and the water depth are considered. Combined

with the method proposed for the frictional resistance, a prediction that is closer to the actual physics is achieved for the viscous part of ship resistance, which can cover the majority of the resistance of low-speed vessels.

#### 8.1.4. Wave-making Resistance

The third sub-goal, as described in Section 1.1 and addressed in Chapter 6, is shown as follows:

*To understand the mechanism of how wave-making resistance is altered in shallow water.*

To reach this sub-goal, the effects of the water depth and the viscosity on the characteristics of ship-generated waves were studied (Chapter 6).

Ship-generated waves become longer when the water is shallower. When  $Fr_h$  (depth Froude number)  $\geq 1.0$ , the wavelength increases dramatically and approximate infinity, which leads to the disappearance of the transverse wave system. The wave superposition behind the stern is, therefore, changed since the waves generated by the bow will arrive at the stern faster with a smaller  $h/T$ .

The wave pattern analysis, which based on the wave energy analysis in inviscid flow, will slightly underestimate the wave-making resistance in shallow water due to the influence of viscosity. Another boundary layer will be formed on the bottom of the waterway yielding about a 3% increase for the total ship resistance.

In shallow water, the wave-making resistance does not merely depend on the Froude number, but the Reynolds number begins to play a role. Based on the results of Chapter 6, the Reynolds number dependence of wave-making resistance is obvious for relatively full vessels (e.g., most inland vessels) at  $Fr_h > 0.5422$ . When  $Fr_h$  approaches 0.700, the coefficient of wave-making resistance at model scale can be two times larger compared to full-scale ships.

## 8.2. Recommendations

In this section, recommendations are provided based on the limitations and challenges faced in this research. The first set presents the additional work of model tests and full-scale ship trials. The second describes how the numerical method can be improved to consolidate findings in this research. The last set two discusses the application range and the consideration of propulsion system.

### 8.2.1. Experimental Aspect

- **Choose several standard inland ships for research purposes.** The existing standard ships, such as the KCS, the KVLCC2, etc., are sea-going ships and cannot be the representatives for inland vessels. Some

crucial characteristics, such as the wetted transom which is commonly found on inland vessels, are generally absent on the sea-going ships. Based on the existing classification of the fairway (e.g., the Classification of European Inland Waterways), it is possible to select a standard inland vessel for each class of waterway. These standard ships would enable more straightforward validations for the CFD calculations specifically conducted for inland vessels.

- **Make resistance data of model tests in shallow water publicly available** The resistance data of ship model tests in shallow water are mostly not accessible. If more data of model tests are publicly available, significant benefits can be expected for the validation of CFD simulations.
- **Seek for a method to do full-scale ship resistance tests.** In this dissertation, the improvement of the proposed method cannot be fully validated since full-scale ship resistance is rare and also almost impossible to measure. Therefore, seeking for a new method to obtain the drag force of a full-scale ship is very challenging but is recommended for future research.

### 8.2.2. Computational Aspect

- **Increase the resolution of CFD simulations.** In the CFD calculations performed in this dissertation, the  $k-\omega$  turbulence model is used. Also, due to the limitations of computing resource, the  $y^+$  is about two at the model scale, and the value is more than 50 at the full scale where wall functions are applied. Although the calculated resistance is practically acceptable, more accurate results and more physical details would be obtained if the large eddy simulations (LES) or even the direct numerical simulations (DNS) are conducted. However, the high-resolution computations will also be more expensive than the CFD calculations conducted in this dissertation.

### 8.2.3. Application Range

- **Enlarge the database of ship resistance in shallow water.** This dissertation provides empirical formulas to predict the resistance for the Wigley hull, the KCS, and the Rhine Ship 86 in shallow water. The proposed method is applicable for a ship with similar dimensions as the three selected ships with small trim and sinkage, but not for all vessels. A more general prediction should consider ship's geometry, trim, sinkage, etc., and this demands an extended size of database which contains each resistance component of at least 20 distinct hull forms in a range of water depths.

#### 8.2.4. Coupled with the propulsion system

- **Include the influence of the propulsion system.** In this dissertation, bare ships without propeller(s) are applied, but resistance and propulsion are coupled performances for realistic ships. In shallow water, the inflow conditions and the operation point are different from deep water scenarios. The performance of propeller(s) will, therefore, be affected and the resistance will be influenced accordingly. Considering the effects of the propulsion system is undoubtedly useful to further improve the prediction of ship resistance in shallow water.



# References

- Airy, G. B. (1841). Tides and waves. *Encyclopaedia Metropolitana (1817–1845), Mixed Sciences*, vol. 3.
- Anderson, J. D. and Wendt, J. (1995). *Computational fluid dynamics*, volume 206. Springer.
- ANSYS (2015). 16.2 help manual, icem cfd. *Ansys Inc.*
- ANSYS (2017a). Ansys® academic research, release 18.1, help system, fluent theory guide.
- ANSYS (2017b). Ansys® academic research, release 18.1, help system, fluent user's guide.
- Apukhtin, P. (1947). Influence of shallow water on resistance of passenger vessels (in russian). *Sudostroeniye, No. 4*.
- Apukhtin, P. and Voytkunskii, Y. (1953). Water resistance to ship motion (in russian). *MASHGIZ*.
- Artjushkov, L. (1968). Wall effect correction for shallow water model tests. *NE Coast Institution of Engineers and Shipbuilders*.
- Baba, E. (1969). A new component of viscous resistance of ships. *Journal of the Society of Naval Architects of Japan*, 1969(125):23–34.
- Bai, K. J. (1978). A note on blockage correction. Report, DAVID W TAYLOR NAVAL SHIP RESEARCH AND DEVELOPMENT CENTER BETHESDA MD.
- Benjamin, T. B., Bona, J. L., and Mahony, J. J. (1972). Model equations for long waves in nonlinear dispersive systems. *Phil. Trans. R. Soc. Lond. A*, 272(1220):47–78.
- Blasius, H. (1908). Grenzsichten in flüssigkeiten mit kleiner reibung. *Zeitschrift für Mathematik und Physik*, 56:1–37.
- Boussinesq, J. (1872). Theorie des ondes et des remous qui se propagent le long d'un canal rectangulaire horizontal, en communiquant an liquide contenu dans ce canal de vitesses sensiblement pareilles de la surface anfond, liouville. *J. Math.*, 17:55–108.

- Briggs, M. J., Vantorre, M., Uliczka, K., and Debaillon, P. (2010). Prediction of squat for underkeel clearance. In *Handbook of coastal and ocean engineering*, pages 723–774. World Scientific.
- Buckingham, E. (1914). On physically similar systems; illustrations of the use of dimensional equations. *Physical Review*, 4(4):345–376.
- Chakrabarti, S. K. (1987). *Hydrodynamics of offshore structures*. WIT press.
- Dand, I. and Ferguson, A. (1973). The squat of full ships in shallow water. Report, NATIONAL PHYSICAL LAB TEDDINGTON (ENGLAND) SHIP DIV.
- Dingemans, M. W. (1994). *Water Wave Propagation Over Uneven Bottoms*. Thesis, Delft University of Technology.
- Dingemans, M. W. (1997). *Water Wave Propagation Over Uneven Bottoms: Part 1*. World Scientific.
- Eça, L. and Hoekstra, M. (2008). The numerical friction line. *Journal of marine science and technology*, 13(4):328–345.
- Eça, L. and Hoekstra, M. (2009). Evaluation of numerical error estimation based on grid refinement studies with the method of the manufactured solutions. *Computers and Fluids*, 38(8):1580–1591.
- Eça, L. and Hoekstra, M. (2014). A procedure for the estimation of the numerical uncertainty of cfd calculations based on grid refinement studies. *Journal of Computational Physics*, 262:104–130.
- Eggers, K., Sharma, S., and Ward, L. (1967). An assessment of some experimental methods for determining the wave-making characteristics of a ship form. *Trans. of SNAME*, 75:112–157.
- Eloot, K. and Vantorre, M. (2011). Ship behaviour in shallow and confined water: an overview of hydrodynamic effects through efd. *Specialists' Meeting on Assessment of Stability and Control Prediction Methods for Air and Sea Vehicles*.
- Fine, R. A. and Millero, F. J. (1973). Compressibility of water as a function of temperature and pressure. *The Journal of Chemical Physics*, 59(10):5529–5536.
- Froude, W. (1868). Observations and suggestions on the subject of determining by experiment the resistance of ships. *The Papers of William Froude, 1810-1879: With a Memoir by Sir Westcott Abell and an Evaluation of William Froude's Work by RWL Gawn: Collected Into One Volume, 1955*.
- Froude, W. (1871). *Experiments for the determination of the resistance of a full-sized ship at various speeds by trials*.

- Garcia-Gómez, A. (2000). On the form factor scale effect. *Ocean Engineering*, 27(1):97–109.
- Gourlay, T. (2008). Dynamic draught of container ships in shallow water. *International Journal of Maritime Engineering*, 150(4):43–56.
- Grigson, C. (1999). A planar friction algorithm and its use in analysing hull resistance. *Trans. RINA*, 142:76–115.
- Hardisty, J. (1990). *Beaches: form and process*. Springer Science and Business Media.
- Havelock, T. H. (1908). The propagation of groups of waves in dispersive media, with application to waves on water produced by a travelling disturbance. *Proceedings of the Royal Society of London. Series A, Containing Papers of a Mathematical and Physical Character*, 81(549):398–430.
- Havelock, T. H. (1928). Wave resistance. *Proceedings of the Royal Society of London. Series A, Containing Papers of a Mathematical and Physical Character*, 118(779):24–33.
- Havelock, T. H. (1932). The theory of wave resistance. *Proc. R. Soc. Lond. A*, 138:339–348.
- Hollenbach, U. (2009). Pro's and con's of the form-factor using prohaska's method when extrapolating the model resistance. *STG Annual Meeting*, page 18–20.
- Holtrop, J. and Mennen, G. (1982). An approximate power prediction method. *International Shipbuilding Progress*, 29:166–170.
- Hughes, G. (1954). Friction and form resistance in turbulent flow and a proposed formulation for use in model and ship correlation. *Trans. Inst. Naval Archit*, 96.
- Hughes, G. and Allan, J. (1951). Turbulence stimulation on ship models. *SNAME Transactions*, 59:281–314.
- Insel, M. and Doctors, L. J. (1995). Wave-pattern prediction of monohulls and catamarans in a shallow water canal by linearised theory. *Proceedings of 12th AFMC, University of Sidney, Sidney*, pages 10–15.
- ITTC (1957). In *8th International Towing Tank Conference*.
- ITTC (2008). Specialist committee on powering performance prediction - final report and recommendations. In *25th International Towing Tank Conference*.
- ITTC (2017a). Practical guidelines for ship cfd applications-recommended procedures and guidelines 7.5-03-02-03. In *Proceedings of the 28th International Towing Tank Conference*.

- ITTC (2017b). Preparation, conduct and analysis of speed/power trials-recommended procedures and guidelines 7.5-04-01-01.1. In *Proceedings of the 28th International Towing Tank Conference*.
- ITTC (2017c). Recommended procedures and guidelines-captive model test. *Proceedings of the 28th International Towing Tank Conference*, pages 7.5-02-06-02.
- ITTC (2017d). Recommended procedures and guidelines-determination of a type a uncertainty estimate of a mean value from a single time series measurement. *Proceedings of the 28th International Towing Tank Conference*, pages 7.5-02-01-06.
- ITTC (2017e). Recommended procedures-example for uncertainty analysis of resistance tests in towing tank. *Proceedings of the 28th International Towing Tank Conference*, pages 7.5-02-02-02.1.
- ITTC (2017f). Recommended procedures-fresh water and seawater properties. *Proceedings of the 28th International Towing Tank Conference*, pages 7.5-02-01-03.
- ITTC (2017g). Recommended procedures-general guideline for uncertainty analysis in resistance tests. *Proceedings of the 28th International Towing Tank Conference*, pages 7.5-02-02-02.
- ITTC (2017h). Recommended procedures-guide to the expression of uncertainty in experimental hydrodynamics. *Proceedings of the 28th International Towing Tank Conference*, pages 7.5-02-01-01.
- ITTC (2017i). Recommended procedures-uncertainty analysis instrument calibration. *Proceedings of the 28th International Towing Tank Conference*, pages 7.5-01-03-01.
- ITTC (2017j). Resistance test-recommended procedures and guidelines 7.5-02-02-01. In *Proceedings of the 28th International Towing Tank Conference*.
- Javanmardi, M. (2015). *The investigation of high quality surfing waves generated by a moving pressure source*. Thesis, University of Tasmania.
- Jiang, T. (2001). A new method for resistance and propulsion prediction of ship performance in shallow water. In *Proceedings of the 8th International Symposium on Practical Design of Ships and Other Floating Structures*, volume 1.
- Jonsson, I. G. (1967). *Wave boundary layers and friction factors*, pages 127-148.

- Kader, B. (1981). Temperature and concentration profiles in fully turbulent boundary layers. *International journal of heat and mass transfer*, 24(9):1541–1544.
- Kajitani, H., Miyata, H., Ikehata, M., Tanaka, H., Adachi, H., Namimatsu, M., and Ogiwara, S. (1983). The summary of the cooperative experiment on wigley parabolic model in japan. Report, TOKYO UNIV (JAPAN).
- Karpov, A. (1946). Calculation of ship resistance in restricted waters (in russian). *TRUDY GII. T. IV*, 2.
- Katsui, T., Asai, H., Himeno, Y., and Tahara, Y. (2005). The proposal of a new friction line. In *Fifth Osaka colloquium on advanced CFD applications to ship flow and hull form design*.
- Kim, W., Van, S., and Kim, D. (2001). Measurement of flows around modern commercial ship models. *Experiments in fluids*, 31(5):567–578.
- Korteweg, D. J. and De Vries, G. (1895). Xli. on the change of form of long waves advancing in a rectangular canal, and on a new type of long stationary waves. *The London, Edinburgh, and Dublin Philosophical Magazine and Journal of Science*, 39(240):422–443.
- Kostas, K., Ginnis, A., Politis, C., and Kaklis, P. (2015). Ship-hull shape optimization with a t-spline based bem–isogeometric solver. *Computer Methods in Applied Mechanics and Engineering*, 284:611–622.
- Kozioł, A. (2013). Three-dimensional turbulence intensity in a compound channel. *Journal of Hydraulic Engineering*, 139(8):852–864.
- Lackenby, H. (1963). The effect of shallow water on ship speed. *Shipbuilder and Marine Engineer*, 70:446–450.
- Lamb, H. (1932). *Hydrodynamics*. Cambridge university press.
- Landweber, L. (1939). *Tests of a Model in Restricted Channels*. U.S. Experimental Model Basin.
- Latorre, R., Luthra, G., and Tang, K. (1982). Improvement of inland waterway vessel and barge tow performance: Translations of selected chinese, german and russian technical articles. Report, University of Michigan.
- Lee, Y.-G., Ha, Y.-J., Lee, S.-H., and Kim, S. H. (2018). A study on the estimation method of the form factor for a full-scale ship. *Brodogradnja: Teorija i praksa brodogradnje i pomorske tehnike*, 69(1):71–87.
- McSullea, G., Rodrigues, J., and Soares, C. G. (2018). Wake of a catamaran navigating in restricted waters. In *Progress in Maritime Technology and Engineering: Proceedings of the 4th International Conference on Maritime Technology and Engineering (MARTECH 2018), May 7-9, 2018, Lisbon, Portugal*, page 175. CRC Press.

- Michell, J. H. (1898). Xi. the wave-resistance of a ship. *The London, Edinburgh, and Dublin Philosophical Magazine and Journal of Science*, 45(272):106–123.
- Millward, A. (1989). The effect of water depth on hull form factor. *International shipbuilding progress*, 36(407):283–302.
- Moctar, O. e., Shigunov, V., and Zorn, T. (2012). Duisburg test case: Post-panamax container ship for benchmarking. *Ship Technology Research*, 59(3):50–64.
- Mucha, P., el Moctar, O., Dettmann, T., and Tenzer, M. (2017). Inland waterway ship test case for resistance and propulsion prediction in shallow water. *Ship technology research*, 64(2):106–113.
- Mucha, P., el Moctar, O., Dettmann, T., and Tenzer, M. (2018). An experimental study on the effect of confined water on resistance and propulsion of an inland waterway ship. *Ocean Engineering*, 167:11–22.
- NACA (1950). English translation of blasius' original paper. *NACA Technical Memorandum 1256*.
- Nagib, H. M., Chauhan, K. A., and Monkewitz, P. A. (2007). Approach to an asymptotic state for zero pressure gradient turbulent boundary layers. *Philosophical Transactions of the Royal Society A: Mathematical, Physical and Engineering Sciences*, 365(1852):755–770.
- Nagib, H. M., Christophorou, C., and Monkewitz, P. A. (2006). High reynolds number turbulent boundary layers subjected to various pressure-gradient conditions. In *IUTAM symposium on one hundred Years of boundary layer research*, pages 383–394. Springer.
- Nezu, I. and Rodi, W. (1986). Open-channel flow measurements with a laser doppler anemometer. *Journal of Hydraulic Engineering*, 112(5):335–355.
- Pascolo, S., Petti, M., and Bosa, S. (2018). Wave–current interaction: A 2dh model for turbulent jet and bottom-friction dissipation. *Water*, 10(4):392.
- Pompée, P.-J. (2015). About modelling inland vessels resistance and propulsion and interaction vessel-waterway key parameters driving restricted/shallow water effects. *Proceeding of Smart Rivers 2015*.
- Pope, S. B. (2000). *Turbulent Flows*. Cambridge University Press. p.271-275.
- Prohaska, C. (1966). A simple method for the evaluation of the form factor and low speed wave resistance. *Proceedings 11th ITTC*.
- Putnam, J. and Johson, J. (1949). The dissipation of wave energy by bottom friction. *Eos, Transactions American Geophysical Union*, 30(1):67–74.

- Raven, H. (1996). *A Solution Method for the Nonlinear Ship Wave Resistance Problem, Doctor's Thesis*. Thesis, Delft University of Technology.
- Raven, H. (2012). A computational study of shallow-water effects on ship viscous resistance. In *29th symposium on naval hydrodynamics, Gothenburg*.
- Raven, H. (2016). A new correction procedure for shallow-water effects in ship speed trials.
- Raven, H. C. and Prins, H. J. (1998). Wave pattern analysis applied to nonlinear ship wave calculations. In *Workshop Water Waves and Floating Bodies, March 29th–April 1st, Alphen a/d Rijn*.
- Raven, H. C., Van der Ploeg, A., Starke, A., and Eça, L. (2008). Towards a cfd-based prediction of ship performance—progress in predicting full-scale resistance and scale effects. *Proceedings of RINA-CFD-2008, London, UK*.
- Rayleigh, L. (1892). Viii. on the question of the stability of the flow of fluids. *The London, Edinburgh, and Dublin philosophical magazine and journal of science*, 34(206):59–70.
- Rayleigh, L. (1915). The principle of similitude. *Nature*, 95:66.
- Roache, P. J. (1998). *Verification and validation in computational science and engineering*. Hermosa, Albuquerque, New Mexico.
- Roemer, M. C. (1940). Translation: Ship resistance in water of limited depth—resistance of sea-going vessels in shallow water.
- Rotteveel, E. (2019). *Influence of inland vessel stern shape aspects on propulsive performance: Derivation of insights and guidelines based on a computational study*. Thesis, Delft University of Technology.
- Rotteveel, E., Hekkenberg, R., and van der Ploeg, A. (2017). Inland ship stern optimization in shallow water. *Ocean Engineering*, 141:555–569.
- Russell, J. S. (1837). *Experimental researches into the laws of certain hydrodynamical phenomena that accompany the motion of floating bodies and have not previously been reduced into conformity with the known laws of the resistance of fluids*. Royal Society of Edinburgh.
- Saha, G. K., Suzuki, K., and Kai, H. (2004). Hydrodynamic optimization of ship hull forms in shallow water. *Journal of Marine Science and Technology*, 9(2):51–62.
- Schijf, J. (1949). Protection of embankments and bed in inland and maritime waters, and in overflows or weirs. In *PIANC 17th congress 1949, Lisbon, section SI C2*. PIANC.

- Schijf, J. and Schönfeld, J. (1953). Theoretical considerations on the motion of salt and fresh water. In *IAHR*.
- Schlichting (1934). Ship resistance in water of limited depth-resistance of sea-going vessels in shallow water (translated by roemer, m.c, 1940). *Jahrbuch der STG*, 35:127–148.
- Schlichting, H. (1941). *Lecture series: Boundary layer theory (translated by NACA technical memorandum No. 1218)*. Luftfahrtforschungsanstalt Hermann Gooring, Braunschweig.
- Schlichting, H. (1979). *Boundary Layer Theory*. McGRAW HILL BOOK COMPANY, New York, 7th edition.
- Schoenherr, K. E. (1932). *On the resistance of flat surfaces moving through a fluid*. Trans. SNAME 40: 279.
- Sharma, S. D. (1963). A comparison of the calculated and measured free-wave spectrum of an inuid in steady motion. *International Seminar on Theoretical Wave-Resistance*, I.
- Österlund, J. M. (1999). *Experimental studies of zero pressure-gradient turbulent boundary layer flow*. Thesis, Ph. D. thesis, Stockholm Royal Institute of Technology, Stockholm.
- Stokes, G. (1847). On the theory of oscillatory waves. *Transactions of the Cambridge Philosophical Society VIII*, pages 197–229.
- Sun, S., Wang, C., Chang, X., and Zhi, Y. (2017). Analysis of ship resistance and flow field characteristics in shallow water. *Harbin Gongcheng Daxue Xuebao/ Journal of Harbin Engineering University*, 38(4):499–505.
- Thill, C. (1991). *Längsschnittmethoden Für die Analyse des Schiffswellensystems unter Berücksichtigung endlicher Wassertiefe (In German)*. Thesis, Masterthesis Gerhard Mercator Universität Duisburg, supervision S.D. Sharma, 35-36.
- Todd, F. (1951). Skin friction resistance and the effects of surface roughness. *SNAME Transactions*, 59:315–374.
- Todd, F. (1966). The model-ship correlation problem. *Marine Technology*, pages 152–157.
- Toxopeus, S. L. (2011). Viscous-flow calculations for kvlcc2 in deep and shallow water. In *MARINE 2011, IV International Conference on Computational Methods in Marine Engineering*.
- Tsang, J. M. F., Dalziel, S. B., and Vriend, N. M. (2018). Interaction between the blasius boundary layer and a free surface. *Journal of Fluid Mechanics*, 839.

- Van der Ploeg, A., Raven, H., Windt, J., Leroyer, A., Queutey, P., Deng, G., and Visonneau, M. (2008). Computations of free-surface viscous flows at model and full scale—a comparison of two different approaches. In *Proceedings of the 27th symposium on naval hydrodynamics, Seoul*.
- Van He, N. and Ikeda, Y. (2013). Optimization of bow shape for a non ballast water ship. *Journal of Marine Science and Application*, 12(3):251–260.
- Walters, D. K. and Cokljat, D. (2008). A three-equation eddy-viscosity model for reynolds-averaged navier–stokes simulations of transitional flow. *Journal of fluids engineering*, 130(12):121401.
- Wei, T. and Willmarth, W. (1989). Reynolds-number effects on the structure of a turbulent channel flow. *Journal of Fluid Mechanics*, 204:57–95.
- Will, J. and Kömpe, A. (2015). Improvements in the prediction of the wave making resistance from potential flow by using transverse wave cut methods. In *ASME 2015 34th International Conference on Ocean, Offshore and Arctic Engineering*, pages V002T08A044–V002T08A044. American Society of Mechanical Engineers.
- Zeng, Q., Hekkenberg, R., and Thill, C. (2019a). On the viscous resistance of ships sailing in shallow water. *Ocean Engineering*, 190:106434.
- Zeng, Q., Hekkenberg, R., and Thill, C. (2019b). A study of ship’s frictional resistance in extremely shallow water. In *38th International Conference on Ocean, Offshore and Arctic Engineering (OMAE 2019), Glasgow, UK*.
- Zeng, Q., Thill, C., and Hekkenberg, R. (2018). A benchmark test of ship resistance in extremely shallow water. In *Progress in Maritime Technology and Engineering: Proceedings of the 4th International Conference on Maritime Technology and Engineering (MARTECH 2018), Lisbon, Portugal*, page 221. CRC Press.
- Zeng, Q., Thill, C., and Hekkenberg, R. (2019c). Shallow water effects on ship-generated waves. In *5th International Conference on Ship Manoeuvring in Shallow and Confined Water (MASHCON 2019), Ostend, Belgium*.
- Zeng, Q., Thill, C., Hekkenberg, R., and Rotteveel, E. (2019d). A modification of the ittc57 correlation line for shallow water. *Journal of Marine Science and Technology*, 24(2):642–657.



# Acknowledgements

Foremost, I would like to express my sincere thanks to my copromoters Robert Hekkenberg and Cornel Thill for the continuous guidance and support of my Ph.D. study and research. Robert, thank you for bringing me into this project. Your insight into my plan and trust are the source of power for me to keep everything on track. The extensive discussions with you taught me a great deal about both scientific research and life in general. Cornel, your very scrupulous manner about both thinking and writing is surely a guarantee of my research quality since even an error of punctuation cannot escape from your eyes. Your knowledge about ship hydrodynamics is quite inspiring and your encouragement is essential for me to overcome research obstacles. I could not have imagined having better guidance for my Ph.D. study.

My sincere thanks also go to my promotor prof. Hans Hopman, for offering me the opportunity to do research in your group and also for your strong support about attending conferences and joining Ph.D. courses.

A special thank-you will be given to Dr. Erik Rotteveel. You are among my supervising team in the first two years of my Ph.D. study, even you are doing your own Ph.D. at that time. Your comments and suggestions are very valuable for improving my research skills.

I would like to thank Prof. Wei Cai and Dr. Xiaoli Jiang, who broadened my horizons as well as minds to a global scale. I am also grateful for your greetings during my Ph.D. study. With a special mention to Dr. Jens Kober. As my mentor, even within limited meetings, you taught me how academic life looks like and also the strategies about finishing Ph.D. work.

This work would not have been possible without the funding of the China Scholarship Council (CSC). Financial support partly offered by the department Maritime and Transport Technology is also highly appreciated. Many thanks to the contribution of the Dutch national supercomputer: Cartesius, and the cluster, Reynolds, in 3mE, which help to realize most numerical computations in this thesis.

I would like to thank my colleague Erik Uijn for your wonderful help with my experiments in the flume tank. I appreciate Peter Poot, Hans van der Hek, Jasper den Ouden and Wick Hillege for your invaluable work during my tests in the towing tank. Also, my sincere thanks go to Dr. Mathieu Pourquie for teaching me how to use an HPC, creating an account on the Reynolds cluster, and helping me solve problems during numerical calculations. I thank Dr. Ido Akkerman and Nico van der Kolk for your help and discussions during my application of a pilot project from Cartesius.

I am especially grateful to the friendship with Martin van Dijk and your wife Hennie. The time spent on your nice boat is extremely impressive. My sincere thanks also go to Hotze Boonstra and Arie Aalbers for inviting me to have dinner with your family. Warm chats with you make me feel at home in the Netherlands. Thanks will also be expressed to Agnieta Habben Jansen, Arthur Vrijdag, Austin Kana, and Dick Mensch for the nice talks with you about both research and life, especially at the beginning of my Ph.D. study.

I would particularly thank my officemates Linying Chen, Zhe Du, and my former officemates Ali Haseltalab, Xiaobo Zhang. It was a great time sharing the office with all of you. I am grateful to my colleagues Wenjing Guo, Faisal Wani, Congbiao Sui, Yamin Huang, Qinqin Zeng, Breno Alves Beirigo, Hamid Gilvari, Johan Los, Zhikang Deng, Zongchen Li, Xiao Li, Sebastian Schreier, Xing Chang, Yanxin Qin, and my former colleagues Xiao Lin, Daijie He, Jialun Liu, Shijie Li, Wenbin Ma, Fan Feng, Xiaojie Luan, Peijuan Xu, Lindert Biert, Jie Cai, Huarong Zheng, Xiangwei Liu, Kai Wang, Guangming Chen, Qu Hu, Chengguang Liu, Tao Zou, for your companion and also for the fun we have had in the last four years. I also want to thank my new friends Qingrui Zhang, Mingxin Li, Yimeng Zhang, for nice talks about the life of Ph.D.

Huge thanks will be given to our secretaries Dineke, Anouk, Patty, Monique, Pauline, and Ria. With your help and arrangement, I can focus on my studies without more worries. It was also fantastic to have the opportunity to do research at TU Delft. What a beautiful and exciting place to work!

Nobody has been more important to me in the pursuit of a Ph.D. than the members of my family. I would like to thank my parents, whose love is with me whenever I need. Most importantly, I wish to thank my beloved wife, Yuying Du. Your unending support brings peace in my heart. I also thank my newborn daughter, Yueran, who brings new joys in my Ph.D. study.

Qingsong Zeng

November 2019, in Delft

# Curriculum Vitæ

## Qingsong ZENG

04-Aug-1991    Born in Guangshui, Hubei, China.

### Education

2008–2012    Undergraduate in Naval Architect and Ocean Engineering  
Wuhan University of Technology, China

2012–2015    Master of Science in Engineering in Design and Construction of Naval Architecture & Ocean Structures  
Wuhan University of Technology, China  
*Thesis:*    Development and Implementation of a Comprehensive Optimization Model for Yacht Geometric Modeling and Hull Principal Dimensions

2015–2019    Ph.D. student  
Delft University of Technology, the Netherlands  
*Thesis:*    A Method to Improve the Prediction of Ship Resistance in Shallow Water  
This research is dedicated to understanding the mechanism of ship resistance in shallow water and to improve the extrapolation of resistance from model scale to full scale using both numerical and experimental methods.

### Research Interests

Ship resistance reduction; hydrodynamics in shallow and confined water; ocean energy conversion.



# List of Publications

- Qingsong Zeng, Robert Hekkenberg, Cornel Thill, Hans Hopman, 2019. Scale effects on the wave-making resistance of ships sailing in shallow water. *Submitted to a journal*.
- Qingsong Zeng, Robert Hekkenberg, Cornel Thill, 2019. On the viscous resistance of ships sailing in shallow water, *Ocean Engineering*, 190, 106434.
- Qingsong Zeng, Robert Hekkenberg, Cornel Thill, 2019. A study of ship's frictional resistance in extremely shallow water, *38th International Conference on Ocean, Offshore & Arctic Engineering (OMAE 2019)*, Glasgow, UK.
- Qingsong Zeng, Cornel Thill, Robert Hekkenberg, 2019. Shallow water effects on ship-generated waves, *5th International Conference on Ship Manoeuvring in Shallow and Confined Water (MASHCON 2019)*, Ostend, Belgium.
- Qingsong Zeng, Cornel Thill, Robert Hekkenberg, Erik Rotteveel, 2019. A modification of the ITTC57 correlation line for shallow water. *Journal of Marine Science and Technology*, 24(2), 642-657.
- Qingsong Zeng, Cornel Thill, Robert Hekkenberg, 2018. A benchmark test of ship resistance in extremely shallow water, *Progress in Maritime Technology and Engineering: 4th International Conference on Maritime Technology and Engineering (MARTECH 2018)*, Lisbon, Portugal, p. 221.
- Qingsong Zeng, Robert Hekkenberg, Cornel Thill, Erik Rotteveel, 2017. Numerical and experimental study of resistance, trim and sinkage of an inland ship model in extremely shallow water. *International Conference on Computer Applications in Shipbuilding (ICCAS 2017)*. Singapore, RINA. 2: 19-25.